University of South Carolina
Scholar Commons

Theses and Dissertations

Spring 2023

Characterization of the Spatial and Temporal Dynamics of Floodplain Surface-Water Circulation

Shailesh Cyriel van der Steeg

Follow this and additional works at: https://scholarcommons.sc.edu/etd

Part of the Geological Engineering Commons

Recommended Citation

van der Steeg, S. C.(2023). *Characterization of the Spatial and Temporal Dynamics of Floodplain Surface-Water Circulation.* (Doctoral dissertation). Retrieved from https://scholarcommons.sc.edu/etd/7330

This Open Access Dissertation is brought to you by Scholar Commons. It has been accepted for inclusion in Theses and Dissertations by an authorized administrator of Scholar Commons. For more information, please contact digres@mailbox.sc.edu.

CHARACTERIZATION OF THE SPATIAL AND TEMPORAL DYNAMICS OF FLOODPLAIN SURFACE-WATER CIRCULATION

by

Shailesh Cyriel van der Steeg

Bachelor of Science
Delft University of Technology, 2014

Master of Science
Delft University of Technology, 2016

Master of Applied Statistics
University of South Carolina, 2021

Submitted in Partial Fulfillment of the Requirements

For the Degree of Doctor of Philosophy in

Geological Sciences

College of Arts and Sciences

University of South Carolina

2023

Accepted by:

Raymond Torres, Major Professor

Enrica Viparelli, Committee Member

Edwin Elias, Committee Member

Jessica Sullivan, Committee Member

Alexander Yankovsky, Committee Member

Venkataraman Lakshmi, Committee Member

Cheryl L. Addy, Interim Vice Provost and Dean of the Graduate School

© Copyright by Shailesh Cyriel van der Steeg, 2023
All Rights Reserved.

ABSTRACT

Floodplains are spatially complex landscapes with a variety of surface features and landforms. These low-relief, low-gradient landscapes may contain extensive networks of well-defined channels and topographically connected depressions, and in some cases, the channels originate as cuts across levees or banks of the main river, referred to as through-bank channels. Corresponding complex patterns of inundation and flow have been detected through remote sensing and in field observations. The complex floodplain flows in response to the passing of flood waves is, however, poorly quantified. This work aims to increase fundamental understanding of floodplain flows and to highlight controls on floodplain wetting, circulation and draining.

Surface water flows dynamics over a topographically complex floodplain are quantified using a novel and robust observation approach, the *Triangular Facet* method. The approach requires a minimum of three stage measurements and can be applied to any inundated surface, across a range of temporal and spatial scales. Water level and flow directions are synchronously measured. The *Triangular Facet* revealed complex and highly variable flow patterns, including abrupt flow reversal. Flows during sub-bankfull inundation (via through-bank channels, river stage is below bankfull stage) are particularly variable, including multiple abrupt flow reversals, while overbank inundation produces a more subdued response with slow rotations. The “triangular facet” approach provides a new type of mesoscale insight of flow processes over inundated landscapes, highlighting flow complexity. Moreover, the approach provides information on floods that represent a compromise between in-situ point velocimeter measurements and satellite remote sensing.

Systemwide understanding of floodplain flow dynamics is obtained by process-based numerical modeling under realistic and unsteady forcing conditions. Calibration and validation of the hydrodynamic model was conducted using in-situ field observations obtained with *Triangular Facet* approach. Simulations highlight floodplain inundation dynamics for two conditions, the passage of sub-bankfull and overbank flood waves. Sub-bankfull inundation commences with the passage of the flood wave crest beyond the lower elevation levee breaches, and floodplain wetting is guided by the channel network. Hence, the upstream sub-bankfull inundation area expands while much of the downstream floodplain remains dry. The onset of overbank flow is spatially variable but becomes continuous, and the through-bank channels persist as preferential pathways that produce higher velocity flows several kilometers inland. Meanwhile, near-stagnant zones develop between through-bank channel mouths, where water is temporarily stored and routed to the channel network. Also, the majority of the inundation water enters the study area from the upstream floodplain (intra-floodplain flow).

To glean deeper insight into processes governing floodplain circulation, reduced complexity simulations were conducted using synthetic hydrographs, constrained by observations. Findings indicate that shallow rising gradients produce enhanced floodplain inundation and result in lower river water levels. Steeper rising gradients deter inundation processes and cause higher water levels in the river. On the contrary, shallow falling stages enhance overall floodplain drainage processes. Steep falling stages, however, result in greater floodplain water retention. The substantial variation in inundation and drainage

processes result from highly variable and complex flow patterns resulting from various rates of change of stage that appear to be dependent on flow thresholds associated with submergence and emergence of topography.

Collectively, these findings highlight complex flows in response to floodplain wetting and draining processes, mutually depending on stage, rate of change of stage, inundation process (sub-bankfull or overbank), intra-floodplain flows, initial floodplain wetting conditions, submergence and emergence of topography. Floodplain wetting and draining processes significantly influence flow direction, and characteristics of the flood wave over the floodplain surface such that a single stage in the main channel does not uniquely define floodplain flow hydraulics. Given these findings we propose that assessments of floodplain hydraulic connectivity account for the effects of heterogeneous levee structure, intra-floodplain exchanges, as well as the typical flow thresholds associated with submergence and emergence of topography. Understanding floodplain flows has important implications as increasingly susceptible to flooding, and this view is especially relevant given the role of modern climate change in compound flooding. Detailed insight on water circulation can aid in, for example, flood hazard and mitigation analyses and in maintaining floodplain ecosystems and water quality, and for dam management.

TABLE OF CONTENTS

CHAPTER 1

INTRODUCTION

Floodplains typically are low relief but topographically complex landscapes (e.g., *Xu et al., 2020; Park, 2020; Lewin and Ashworth, 2014*) with a structure reflecting the range of drivers operating at different temporal and spatial scales (e.g., *Dunne and Aalto, 2013; Trigg et al., 2012; Mertes et al., 1997*). Floodplain features are readily identifiable in satellite imagery for large rivers (e.g., *Mertes et al., 1997; Rowland et al., 2009; Lewin & Ashworth, 2014*), and in data from airborne lidar for much smaller systems (e.g., *Xu et al., 2020; Lindroth et al., 2020; David et al., 2017;*). These data reveal that floodplains contain extensive networks of well-defined channels and topographically connected depressions (e.g., *Xu et al*., 2020; *David et al*., 2017; *Fagan & Nanson*, 2004), and in some cases the channels originate as cuts across levees or banks of the main river, referred to as through-bank channel (*Xu et al*., 2021; *Day et al., 2008*; *Lewin and Hughes*, 1978).

Floodplain topography exerts a considerable influence on surface inundation and flows (e.g., *Xu et al., 2021; van der Steeg et al., 2021; Lindroth et al., 2020*). Remote sensing of inundated floodplains reveals extensive temporal and spatial variability in water surface elevation and current direction (*Alsdorf et al., 2007a,b; Mertes, 1997*). The flow complexity is largely associated with spatially variable inundation that arises from a disequilibrium with the water surface of the main channel and the floodplain (*Alsdorf et al., 2007b*). For instance, field observations (*Filgueira-Rivera et al., 2007*) show that elevations of the free surface between the main river and floodplain differ by up to 0.12 m, giving rise to complex flow patterns. Another study shows that water surface elevation gradient across a river-floodplain system varied by a factor of ~9 (*Girard et al., 2009*). In addition, numerical simulations of floodplain inundation suggest that the timing and pattern of flows are strongly influenced by the local, albeit low relief geomorphic features (e.g., *Pinel et al., 2020; Czuba et al., 2019*).

Analyses of floodplain topography (*Lindroth et al., 2020; David et al., 2017;*), and hydrodynamic modeling (*Czuba et al., 2019; Byrne et al., 2019; Tull et al., 2022*) reveal that floodplain inundation occurs in the absence of overbank flow. These studies contrast with the typical view of inundation by overbank flows. In particular, sub-bankfull flows give rise to frequent, low-magnitude inundation (*Czuba et al., 2019; Park* & *Latrubesse, 2017; Kaase & Kupfer, 2016*). Inundation under these conditions occurs via the through bank channels and their networks (*Park and Latrubesse, 2017; Rowland et al., 2009; Czuba et al., 2019*). At high but sub-bankfull flow conditions through-bank channels are the hydraulic openings to expansive albeit low-relief surface flow networks that give rise to low-level floodplain inundation. Furthermore, discrete river-floodplain segments may experience the simultaneous occurrence of sub-bankfull and overbank flooding, or no flooding at all depending on heterogeneity in the along-channel and vertical structure of riverbanks and levees, giving rise to an inundation continuum (*Xu et al., 2021*); i.e., the non-uniform transition from a completely dry to the fully inundated floodplain. The net result is highly a variable and complex floodplain flow (*Xu et al., 2021*), that can present abrupt current reversals (*van der Steeg et al., 2021*). Hence, complex flow dynamics develop in response to along-channel variability in inundation associated with heterogeneous levee development, resulting in the simultaneous occurrence of through-bank (i.e., sub-bankfull) and overbank inundation (*Xu et al., 2021; Lewin and Huges, 1978; van der Steeg et al., 2022*). Furthermore, the submergence-emergence of vegetation (e.g., *Baptiste et al., 2004; Box et al., 2021; Mertes et al., 1995*), and spatial and temporal variability in short-lived tributary inflows (e.g., *Alsdorf et al., 2000; Mertes, 1997, van der Steeg et al., 2022*) enhance flow complexity.

Collectively, floodplain channels facilitate the lateral hydraulic connectivity of the river-floodplain system. Connectivity refers to the various surface flow pathways and dynamics of inundation, and hydraulically mediated exchange between the main river and the floodplain (*Amoros and Bornette*, 2002; *Wohl et al.*, 2019; *Passalacqua*, 2017). Hydraulic connectivity can be expected to vary considerably with variations in stage (e.g., *Amoros & Bornette*, 2002*; Xu et al., 2021; Czuba et al., 2019*). The straight-line distance between a floodplain waterbody and the main channel usually does not well explain the inundation pattern of the floodplain (e.g., *Park and Latrubesse*, 2017). Instead, connectivity is controlled by the inundation frequency and the intricate floodplain topography including the spatial distribution of the channel network (e.g., *Xu et al., 2021; Czuba et al., 2019; Pinel et al., 2020*). Assessments of floodplain channel networks and how they facilitate hydraulic connectivity remains a topic of active research (e.g., *Day et al.*, 2008; *Trigg et al.*, 2012; *Xu et al., 2021*).

Understanding floodplain flow dynamics starts with observing and quantifying the in-situ movement of water over a topographically complex floodplain. Despite that the aforementioned studies provide details on inundation pathways and dynamics, there remains a dearth of information on in situ flow paths at a scale suitable for the characterization of inundation and drainage processes. Therefore, advancements in understanding floodplain flow dynamics ultimately require detailed insight on floodplain inundation processes and pathways, and the hydraulic framework that drives them. Currently, gaining in situ knowledge on flow patterns and pathways requires the deployment of multiple velocimeters across the floodplain with the hope of measuring the dynamics of an anticipated flood event. However, despite the availability of fully autonomous current measuring devices, such as acoustic current profilers, the literature is completely devoid of such observations over floodplains. Part of the problem is likely related to the high cost of these devices (~20 times the cost of sensors used here) and the researcher's limited ability to predict floodplain inundation events. Also, in deploying an autonomous device, the researcher must do an informal cost-benefit analysis that includes vandalism when the device is subaerial. This notwithstanding, acoustic devices have been used to show highly complex flow patterns for tidal inundations over salt marshes (e.g., Torres & Styles, 2007) and they reveal the important role of topography to inundation and drainage flow processes of an intertidal “floodplain.”

In the absence of appropriate field data, researchers often resort to process-based hydrodynamic models for detailed analyses of flows over a floodplain (e.g., *Pinel et al., 2020; Byrne et al., 2019; Czuba et al., 2019*). One major advantage of numerical flow modeling is the capability to increase the spatial and temporal resolution of point-oriented field observations. If constrained with suitable field data, model results can provide near-realistic predictions of flows with high spatial and temporal resolution, which allow for hydrodynamic assessments across the model domain. Recent floodplain modeling efforts provide insight into floodplain flows, but the model constructs lack sufficient calibration to account for realistic, time-varying flow conditions (e.g., *Tull et al., 2022; Pinel et al.,* *2020; Czuba et al., 2019*). For example, *Czuba et al.* (*2019*) highlight how floodplain channels affect hydraulic connectivity under steady boundary conditions. This approach precludes the assessment of inundation dynamics of floods with highly variable stages. Similarly, *Tull et al.* (*2022*) used quasi-steady boundary conditions to demonstrate that during sub-bankfull river stages complex floodplain flows can result due to prior flooding. This approach improves on the work by *Czuba et al. (2019)* but it provides limited insight on flow processes because the boundary conditions fail to represent actual drivers of system dynamics, hence advances in floodplain science through numerical modeling require the application of unsteady forcing conditions. In addition to representative boundary conditions, models require careful incorporation of floodplain structure (i.e., topo-bathymetry) as part of the computational grid (e.g., *Yamazaki et al., 2012; Neal et al., 2012; Verwey et al., 2001*). This approach requires a priori knowledge of often overlooked floodplain channel networks (e.g., *Xu et al., 2020; Wohl et al., 2011*) and a priori knowledge of flow processes.

This work combines field observations, topographic analysis, and hydrodynamic modelling to glean deeper insight into processes governing the wetting, circulation, and draining of floodplains. The results from this work can help provide a more physically based, and system wide understanding of flow complexity over inundated floodplains, and it can enhance efforts to quantify hydraulic connectivity. Detailed insight on water circulation over inundated areas and the processes that facilitate inundation and drainage can aid in, for example, flood hazard and mitigation analyses and in maintaining floodplain ecosystems and water quality (e.g., *Fischer et al., 2019; Funk et al., 2020; Osterkamp & Hupp, 2009)*. Furthermore, understanding the dynamics of floodplain flows aids flood hazard and prediction and mitigation analyses through, for example, floodplain wave attenuation.

RESEARCH OBJECTIVES

The objective of this dissertation is to increase the fundamental understanding of river and floodplain interactions, specifically focusing on surface-water floodplain circulation, inundation and drainage processes over a complex, but low-relief and low-gradient floodplain. The Congaree River floodplain within the Congaree National Park (CNP) located in the southeastern North American coastal plain in South Carolina is used as a study object because the park has been held in conservation since the mid-1970s and there has been no significant shift in species community due to human activities *(Kinzer, 2017)* and local systems with perennial and intermittent channels have been reported by several authors (e.g., *Xu et al., 2020; Kaase and Kupfer, 2016; Shelley, 2007*). Furthermore, the Congaree River discharges hydrological conditions varies substantially (discharge 190-4200 m3/s between 1940-2022), and the riverbank and levee height are highly variable, thereby facilitating irregular sub-bankfull and overbank inundation patterns (*Xu et al., 2021*) over a wide range of forcing conditions.

This works aims to answer the following questions: - what are reliable methods to observe in-situ flow dynamics under variable forcing conditions over a low-gradient and low relief floodplain, - what are the spatial and temporal variability of flow dynamics across the floodplain; - what are the topographic controls on the spatial and temporal variability of flow, and, - what are the effects of the characteristics of the river hydrograph on floodplain flow dynamics? These questions are expressed in three basic research objectives:

- Determine in-situ spatial and temporal variability of flow in the floodplain under variable hydrologic forcings conditions.

- Determine the topographic controls on flow dynamics under dynamic hydrologic conditions.

- Determine the factors of river hydrographs that control and influence floodplain flow dynamics and storage processes.

RESEARCH APPROACH AND OUTLINE

The research questions formulated in the previous section cover a wide range of temporal and spatial scales that require detailed analysis of field measurements, interpretation of topographic analysis to understand flow process and numerical process-based modeling to obtain fundamental understanding floodplain flow processes. Three scientific papers that have been submitter or published in peer-reviewed journals form the core of this work, and the dissertation is written in such a manner that all chapters can be read individually.

To understand floodplain flow dynamics, in-situ inundation and drainage processes needs to be observed and analyzed. Chapter 2 presents a robust and novel method ("Triangular Facet") that allows researchers to observe in-situ flow water levels and flow directions over inundated floodplains and creates new and robust opportunities for field observation and for validation of numerical simulations and remote sensing analyses. The application of the method in the study site revealed complex spatially and temporal varying flow dynamics, including abrupt current reversals, during sub-bankfull and overbank inundation in response to passing flood wave.

In Chapter 3, results from the Triangular facet approach are used to calibrate and validate a Delft3D Flexible Mesh model for the Congaree River and floodplain against water level and flow directions under realistic, time-varying flow conditions. Quantitative analyses of model performance indicate that simulation results are representative of actual field conditions. The results of realistic model applications have been used to generate near-realistic predictions of flows with high spatial and temporal resolution, which allow for hydrodynamic assessments across the model domain during the passage of sub-bankfull and overbank floodwaves. Model results reveal that floodplain flows can be predictably simple or complex, largely controlled by inundation process. Sub-bankfull inundation commences with the passage of the flood wave crest beyond the lower elevation levee breaches, and floodplain wetting is guided by the channel network. The corresponding floodplain flow patterns are highly variable, including current reversals, and the variability appears to be dependent on thresholds in stage. The onset of overbank flow is spatially variable but becomes continuous, and the through-bank channels persist as preferential pathways, while near-stagnant zones develop between through-bank channel mouths, where water is temporarily stored and routed to the channel network. Overall, floodplain wetting and draining processes significantly influence flow direction, and characteristics of the flood wave over the floodplain surface such that a single stage in the main channel does not uniquely define floodplain flow hydraulics.

Chapter 4 focuses on the effects of the characteristics of the river hydrograph on the dynamics of floodplain flows. Impacts of the rate of change of stage of both falling and rising limbs were assed using the Delft3D Flexible Mesh model with synthetic forcing. The characteristics of synthetic hydrographs were constrained by observations. During both sub-bankfull and overbank floodwaves, shallow rising gradients augment floodplain inundation and results in lower river water levels for both sub-bankfull and overbank inundation, while steeper rising gradients deter inundation processes while causing higher water levels in the main river channel. River-floodplain exchange for shallow rising stages is initiated at lower river stages than for the same stage during a steep rise. Shallow falling stages promote overall floodplain drainage processes for both sub-bankfull and overbank inundation. Steep falling stages, however, leave larger amounts of water in the floodplain. Slow stage increases, allow the distribution of floodwater to keep pace with river stage, and more water will be transported into the floodplain at the same stage than with a steep rising wave. Shallow falling stages stimulate overall floodplain drainage processes for both sub-bankfull and overbank inundation. Steep falling limbs indicate that the river and floodplain are out of phase as drainage processes cannot keep pace with the falling river stage and outflow, resulting in larger amount of water left in the floodplain.

CHAPTER 2

A NOVEL METHOD FOR GAINING NEW INSIGHT ON FLOWS OVER INUNDATED LANDSCAPES[1]

We present a novel approach for detecting surface water flows over flooded terrain. The approach requires a minimum of three stage measurements and can be applied to any inundated surface, across a range of temporal and spatial scales. This method creates new and robust opportunities for field observation and for validation of numerical simulations and remote sensing analyses. In this proof-of-concept study, we found that floodplain free surface gradients were particularly variable during sub-bankfull inundation, including abrupt current reversals. Also, flow direction varied with stage and the rate of change in stage. The “triangular facet” approach provides a new type of mesoscale insight of flow processes over inundated landscapes, highlighting flow complexity. Moreover, the approach provides information on floods that represent a compromise between point velocimeter measurements and satellite remote sensing and it can provide substantial benefits to society by aiding in flood hazard and mitigation assessment and planning.

2.1 INTRODUCTION

Low-relief and low-gradient landscapes, particularly along some continental margins, are increasingly susceptible to flooding, and this view is especially relevant given

---

[1] van der Steeg, S., Xu, H., Torres, R., Elias, E. P., Sullivan, J. C., Viparelli, E., ... & Lakshmi, V. (2021). A novel method for gaining new insight on flows over inundated landscapes. *Geophysical Research Letters*, *48*(20), e2021GL094190.

the role of modern climate change in compound flooding (*IPCC, 2021*). Floodplains are a distinct type of low-relief and low-gradient landscape with a land cover that can range from dense urban centers to largely uninhabited. Although floodplain floods may be considered natural hazards that affect many people at great cost, it has been shown that floodplains and floodplain processes provide substantial benefits to society (e.g., *Jakubínský et al., 2021; Mazzoleni et al., 2021; Rak et al., 2016*). Therefore, detailed insight on water circulation over inundated areas and the processes that facilitate inundation and drainage can aid in, for example, flood hazard and mitigation analyses and in maintaining floodplain ecosystems and water quality (e.g., *Fischer et al., 2019; Funk et al., 2020; Osterkamp & Hupp, 2009*). Moreover, despite their limited extent of ~0.5–1% of land area worldwide (e.g., *Sutfin et al., 2016*), they have a disproportionately large role in the global carbon cycle largely driven by cycles of inundation (e.g., *D'Elia et al., 2017; Lininger et al., 2019; Sutfin et al., 2016*).

Remote sensing of inundated floodplains reveals extensive temporal and spatial variability in water surface elevation and current direction (*D. Alsdorf et al., 2007; D. E. Alsdorf et al., 2007; Mertes, 1997*). The flow complexity is largely associated with spatially variable inundation that arises from a disequilibrium with the water surface of the main channel and the floodplain (*D. E. Alsdorf et al., 2007*). For instance, *Filgueira-Rivera et al. (2007)* show that elevations of the free surface between the main river and floodplain differ by up to 0.12 m, giving rise to complex flow patterns. Also, *Girard et al. (2009)* show that water surface elevation gradient across a river–floodplain system varied by a factor of ~9. Further, numerical simulations of floodplain inundation suggest that the timing and pattern of flows are strongly influenced by the local, albeit low-relief geomorphic features (e.g., *Czuba et al., 2019; Pinel et al., 2020*).

Analyses of floodplain topography (*David et al., 2017; Lindroth et al., 2020*) and hydrodynamic modeling (*Czuba et al., 2019*) reveal that floodplain inundation occurs in the absence of overbank flow. These studies contrast with the typical view of inundation by overbank flows. In particular, sub-bankfull flows give rise to frequent, low-magnitude inundation (*Czuba et al., 2019; Kaase & Kupfer, 2016; Park & Latrubesse, 2017*). These observations are important because sub-bankfull flows facilitate a persistent hydraulic connectivity in floodplains (*Passalacqua, 2017; Wohl et al., 2019*) without overbank floods. Therefore, understanding floodplain inundation during low-frequency overbank inundation and high-frequency, but low-magnitude, sub-bankfull inundation is essential to understanding floodplain sustainability.

Although the above studies provide details on inundation pathways and dynamics, there remains a dearth of information on in situ flow paths at a scale suitable for the characterization of inundation and drainage processes. Therefore, advancements in understanding floodplain flow dynamics ultimately require detailed insight on floodplain inundation processes and pathways, and the hydraulic framework that drives them. Currently, gaining in situ knowledge on flow patterns and pathways requires the deployment of multiple velocimeters across the floodplain with the hope of measuring the dynamics of an anticipated flood event. However, despite the availability of fully autonomous current measuring devices, such as acoustic current profilers, the literature is completely devoid of such observations over floodplains. Part of the problem is likely related to the high cost of these devices (~20 times the cost of sensors used here) and the researcher's limited ability to predict floodplain inundation events. Also, in deploying an autonomous device, the researcher must do an informal cost-benefit analysis that includes vandalism when the device is subaerial. This notwithstanding, acoustic devices have been used to show highly complex flow patterns for tidal inundations over salt marshes (e.g., *Torres & Styles, 2007*) and they reveal the important role of topography to inundation and drainage flow processes of an intertidal "floodplain." However, these approaches offer only point measurements and given the potential for acoustic interference by accumulations of large and small woody debris or sediment covering the acoustic sensor heads, the data may or may not be representative of actual floodplain flow conditions.

The work presented here introduces a low-cost, robust, in situ approach to estimating maximum free surface gradients that can help fill a knowledge gap on floodplain flow dynamics. Hence, this work is a proof-of-concept study for gaining mesoscale (~0.01 km^2) insight on inundation that can help improve our understanding of flooding, circulation, and drainage processes over a complex, but low-relief and low-gradient floodplain. However, the approach can be applied to any inundated surface, at any field location and over a large range of spatial scales (e.g., >>0.01 km^2). We hypothesize that interactions of decimeter scale relief and water stage collectively impart complex flow patterns onto floodplain circulation, across a range of spatial and temporal scales. This hypothesis will be tested by analyzing maximum free surface gradient data from a range of inundation levels. In the following narrative, we use "gradient," "flow," and "vector" interchangeably for "the maximum free surface gradient" determined by the "triangular facet" approach.

2.2 STUDY REGION AND HYDROLOGIC CONDITIONS

The study site is a river-floodplain system of the southeastern North American coastal plain (Figure 2.1a), the Congaree River, SC, USA, in the Congaree National Park (CNP). The densely forested study site is 18.8 km long, and up to 5.9 km wide with a total area of 93 km^2. Mean floodplain valley elevation declines from 35.0 to 24.5 m giving an average valley gradient of 4×10^{-4} (*Xu et al., 2020*). The floodplain is bound by the Congaree River to the south and southwest and by bluffs to the north (Figure 2.1a).

The main channel along the CNP boundary is 39.1 km long with a gradient of 1.5×10^{-4}. *Xu et al. (2020)* showed that the bank elevation profile has a highly variable levee/bank crest height, thereby facilitating irregular along-channel inundation patterns. In particular, the levees in the upstream reach require a higher river stage for overbank inundation and therefore favor through-bank inundation, while in the downstream reach, the levees are lower and overbank inundation occurs at lower river stages (*Xu et al., 2020*). The locations for sub-bankfull inundation are the 32 well-developed through-bank channels, channels that cut through the local bank or levee, with mouth widths ranging from 7 to 30 m and some through-bank channels extend several kilometers into the floodplain interior. Hence, for a single discharge, floodplain inundation can occur by a combination of sub-bankfull and overbank flows (e.g., *Lindroth et al., 2020*).

The United States Geological Survey (USGS) Congaree River station in Columbia, SC (#02169500), provides the nearest long-term discharge record, 38 river kilometers upstream of the study site. Discharge from 1984 to 2020 range from 30 to 4,200 m^3/s with a median value of 146 m^3/s. Water levels at the USGS Gadsden station (#02169625, Figure 2.1a) at the upstream park boundary show that the local stage (discharge not reported) varies by 8 m. We estimate that sub-bankfull inundations based on the Gadsden gauge occur 11% of the time, while overbank inundations occur at 5%.

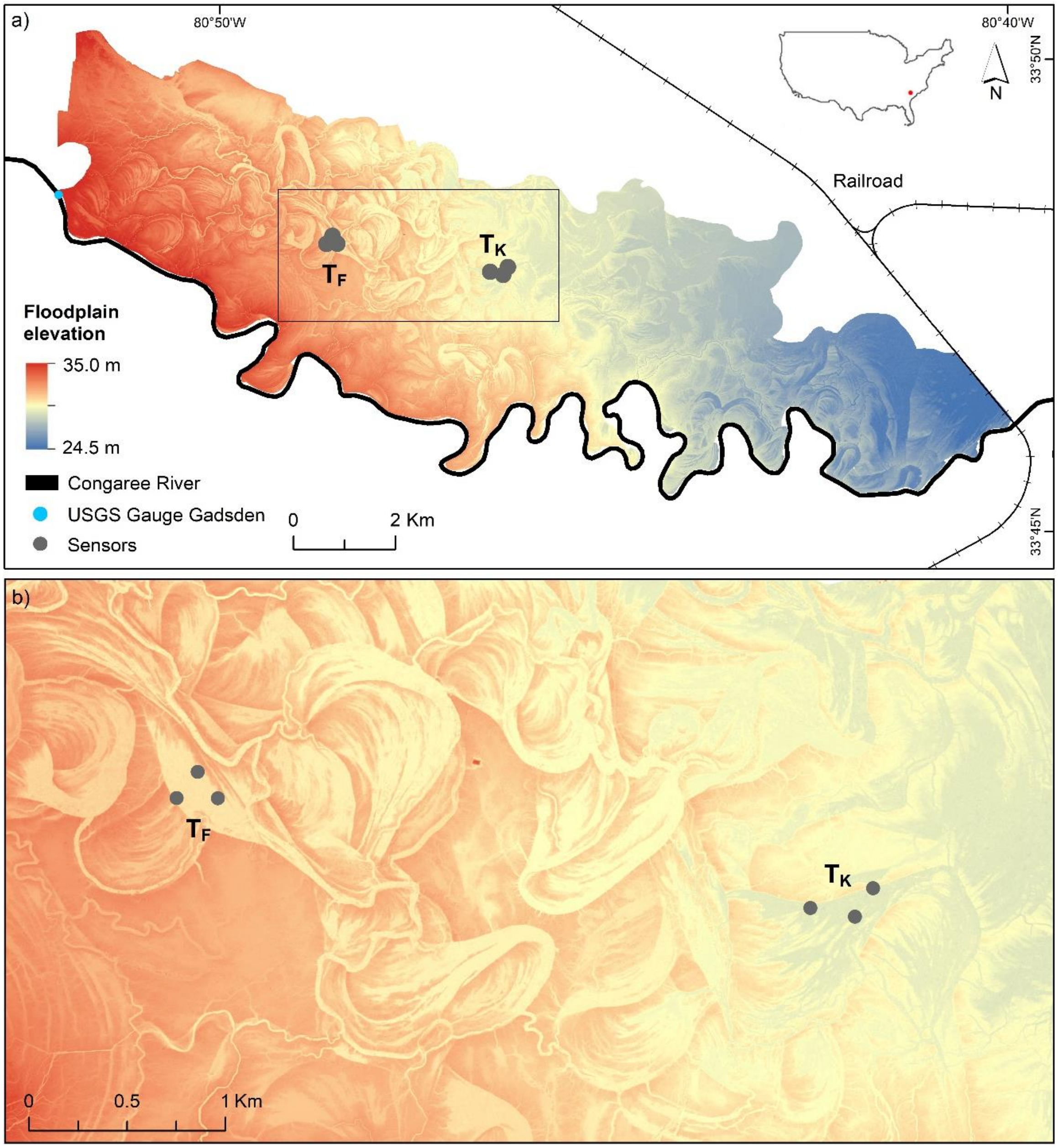

Figure 2.1: Study site. (a) Lidar DEM of the floodplain. Light green symbols show the location of water level sensors. Blue symbol is the United States Geological Survey (USGS) Gadsden station (#02169625). The inset map shows the location of Congaree National Park (CNP). (b) Subarea of the DEM showing the detailed topography around the sensors. The elevation within the subarea declines from 31.9 to 27.3 m

2.3 METHODOLOGY

Water depths on the floodplain were measured using Onset HOBO U20 absolute pressure transducers (hereafter "sensors") set to record at 0.25-hr intervals. Sensors were deployed in protective enclosures, mounted to ~1 m long stakes, and installed 2–3 km inland of the main channel, in subtle depressions (Figure 2.1a). Individual sensors have a typical accuracy of 0.004 m. The pressure readings were compensated for atmospheric pressure with an identical sensor deployed as a barometer. The resulting pressure readings were converted to water depth using the Onset HOBOware Pro software suite.

Each set of three sensors was arranged into a triangular configuration with the assumption that three sensor values define an average free surface plane; the triangle sites are French Pond (T_F) and Kingsnake (T_K; Figure 2.1a). The instrument accuracy has implications for the minimum detectable free surface gradient, and thus it influences the minimum distance between vertices of a triangle. Three sensors combined have a maximum error of 0.0069 m. To measure expected water surface slopes of $\sim 10^{-4}$ (e.g., the regional floodplain gradient) or larger, and accounting for propagation of uncertainty (*Andraos, 1996*) related to instrument accuracy and sensor deployment (e.g., GPS accuracy), we determined that the sensors must be placed a minimum of 123 m apart, giving an area of ~0.0075 km^2 for an equilateral triangle. Error analyses show that these factors give rise to a maximum error of $\sim 10^{-8}$ for a free surface gradient of $\sim 10^{-4}$. The distances between sensors (Figure 2.1b), starting from the north, in an anticlockwise direction for T_F are 171, 210, and 170 m, respectively, with area and mean elevation of 0.018 km^2 and 27.82 m, respectively; meanwhile for T_K, the values are 330, 231, and 172 m and 0.014 km^2 and 28.79 m, respectively.

Computing free surface orientation requires that the corresponding depth data be referenced to a common vertical datum. After several field excursions, we determined that the forest canopy precludes the acquisition of high-precision GPS measurement of sensor elevation, even during winter, or “leaf-off” months. To circumvent this problem, we account for differences in elevation between sensors by referencing sensors of each triangle to a local static water surface. Here, we defined the steady-state stage for a “zero” elevation as an interval with maximum variations of 0.005 m over a period of 6 hr. We went on to determine the maximum free surface gradient magnitude and direction over specific inundation intervals. To enhance the visualization of graphical representations of results, vector thinning was applied to the 0.25-hr data; thus, we present one vector per 2-hr interval instead of eight (Figure 2.2).

This “triangular facet approach” is a novel application for defining inundation water free surface orientation, but it is identical to applications used to visualize groundwater flow dynamics (e.g., *Freeze & Cherry, 1979*) and coastal ocean gradients (*Yankovsky, 2003*). The main goal of our efforts is to capture the free surface gradients and maximum gradient direction every 0.25 hr as they vary with synchronous water level fluctuations at the vertices of the triangles. We assume that the inferred flow directions taken as the maximum gradient direction can be used to shed light on flow dynamics. Free surface gradients were only calculated when all sensors per triangle and corresponding areas were fully inundated.

Estimates of the free surface gradient allowed us to infer velocities computed with the Manning formula (e.g., *Harvey et al., 2009*). Note, however, that the computation of velocity is performed as a validation of the triangular facet approach to determine if the computed gradients give velocity values that are consistent with those in the literature. Application of the formula requires estimates of the hydraulic gradient and the Manning coefficient. We estimated the hydraulic radius as mean depth within a triangular array (e.g., *US Department of Agriculture-Natural Resources Conservation Service, 2007*). Roughness parameters are estimated based on the USGS (*Arcement & Schneider, 1989*) and we use $n = 0.11$ s/m$^{1/3}$, well within the range (0.015–0.40 s/m$^{1/3}$) reported in the literature (e.g., *Czuba et al., 2019; Juez et al., 2019; Liu et al., 2019).* Finally, rainfall-induced floodplain inundation is not considered here and its effects were excluded from all analyses of flow dynamics. The pluvial style of inundation generates a “bathtub-style” filling of the basin (e.g., *Williams & Lück-Vogel, 2020*) as opposed to a wave advancing over the floodplain (e.g., *González-Sanchis et al., 2012*), the latter being the main focus of this work.

Analyses of free surface gradients, flow directions, and velocity estimates were performed for sub-bankfull and overbank flow conditions. River water depth measurements and bank elevations at six locations along the main channel were collected and converted to a common vertical reference using a high-precision GPS (horizontal and vertical accuracy ±0.015 and 0.025 m, respectively). Bank elevations and water level readings were combined to determine the occurrence of sub-bankfull or overbank flow conditions. Sub-bankfull flow conditions occur when water levels at the Gadsden gauge are between 29.95 and 31.54 m, while overbank flow occurs when water levels exceed 31.54 m. Field observations indicate that the area around the sensors is fully submerged at stages that exceed ∼1.0 m (Figure 2.1b).

2.4 RESULTS

Free surface gradients range from 0.1 to 2.27×10^{-4}, and the inferred flow directions reveal several levels of complexity, from subtle reorientations with stage to complete current reversals. We elaborate on these findings by evaluating the stage hydrographs in response to two sub-bankfull inundation intervals for local water depths reaching 1.0–1.1 m (Figures 2.2a–2.2d). In both cases, stage increases at approximately the same rate from September 14 to 17 before reaching a single peak of ∼1.0 m. Thereafter, a concave-up recession occurs, although a break in slope on September 20 is not apparent in both (Figures 2.2a–2.2d). The April 6–30 hydrographs are similar showing the stage increasing from about 0.5 to 1.1 m, and with three peaks several days apart (Figure 2.2b and 2.2d), followed by a much steeper recession rate.

2.4.1 SUB-BANKFULL INUNDATION

For T_F stages <29.58 m, one sensor is subaerial and the data are not analyzed (Figure 2.2a). Above 29.58 m, the sub-bankfull inundation flow paths are initially eastward but become directed northward, with a slight component in the down valley direction (Figure 2.2a). Within this general trend are approximately day-long intervals where the free surface gradients develop a greater downslope component or 20°–30° rotation eastward. The gradient magnitude generally increases with stage. It has a mean of $0.23 \times 10^{-4} \pm 0.084 \times 10^{-4}$ and a maximum of 0.49×10^{-4}. Note that maximum gradients precede maximum stage by about 1 day (Figure 2.2a). Flow paths directed northward occur once the stage exceeds ∼29.62 m, the elevation of the northern edge of the local depression (Figure 1b). On the other hand, at a slightly higher sub-bankfull stage, the time series of T_F flow vectors (Figure 2.2b) differ substantially from the lower hydrograph stage. At stages

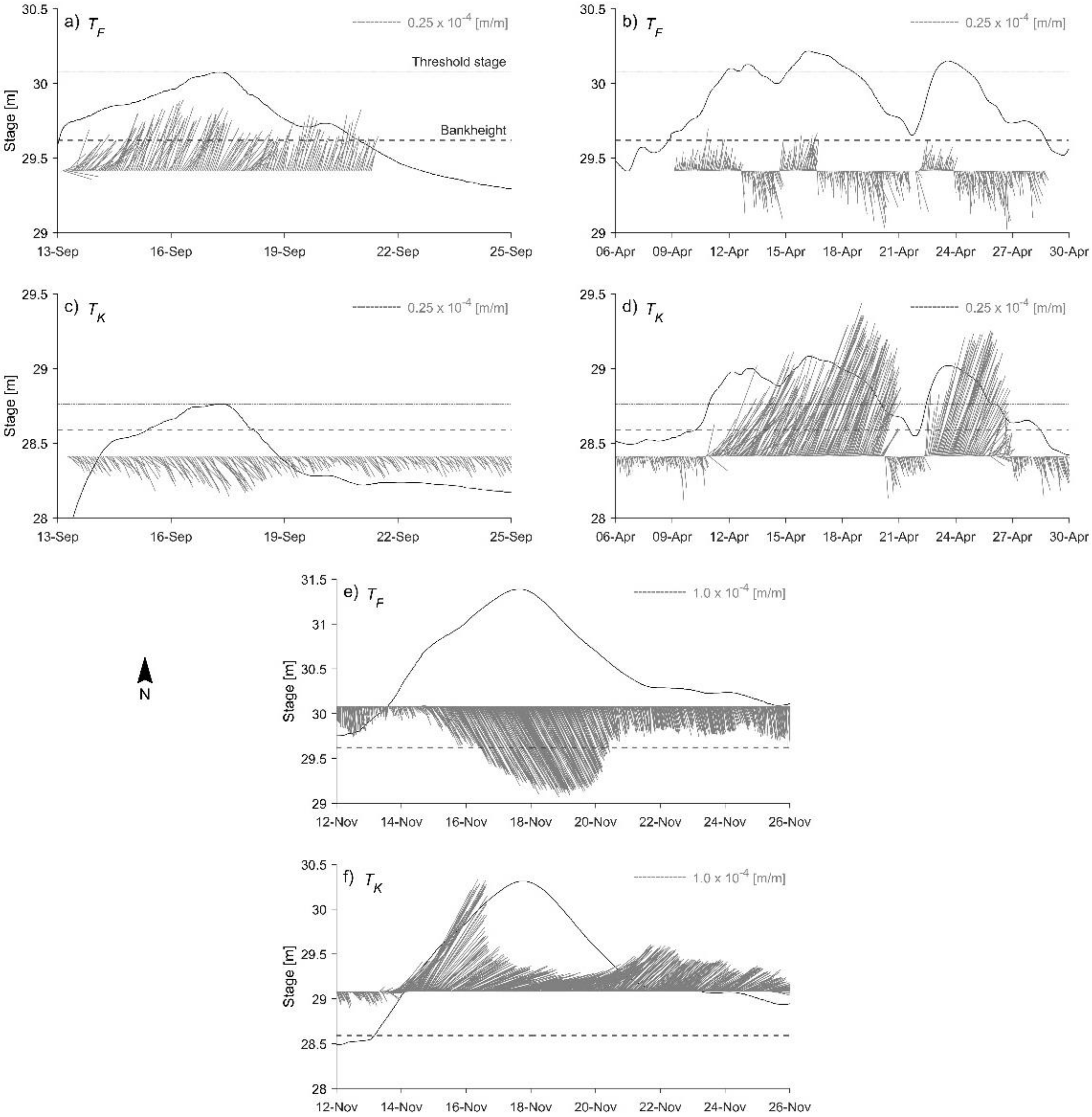

Figure 2.2: Flow dynamics of sub-bankfull inundation at T_F (a, b for different stages), sub-bankfull inundation at T_K (c, d for different stages), and overbank inundation at T_F (e) and T_K (f). The black line indicates the maximum stage hydrograph observed within a triangular facet. The horizontal dashed lines indicate average depression height containing the triangular arrays. The horizontal dashed-dotted line indicates a threshold stage. Gray vectors indicate magnitude and direction, with north at the top. Note that due to thinning of the data, each vector represents a 2-hr interval.

>30.08 m, flow directions shift between northerly and southerly trends, and each cycle persists for >1.5 days (Figure 2.2b). In particular, during the rising stages of the three peaks, the flows are to the north, while during recession they are to the south (Figure 2.2b).

Gradients associated with the falling limbs are slightly larger than during the rising limb, with a mean of $0.11 \times 10^{-4} \pm 0.069 \times 10^{-4}$ and a maximum of 0.43×10^{-4}.

For T_F stages <29.58 m, one sensor is subaerial and the data are not analyzed (Figure 2.2a). Above 29.58 m, the sub-bankfull inundation flow paths are initially eastward but become directed northward, with a slight component in the down valley direction (Figure 2.2a). Within this general trend are approximately day-long intervals where the free surface gradients develop a greater downslope component or 20°–30° rotation eastward. The gradient magnitude generally increases with stage. It has a mean of $0.23 \times 10^{-4} \pm 0.084 \times 10^{-4}$ and a maximum of 0.49×10^{-4}. Note that maximum gradients precede maximum stage by about 1 day (Figure 2.2a). Flow paths directed northward occur once the stage exceeds ∼29.62 m, the elevation of the northern edge of the local depression (Figure 1b). On the other hand, at a slightly higher sub-bankfull stage, the time series of T_F flow vectors (Figure 2.2b) differ substantially from the lower hydrograph stage. At stages >30.08 m, flow directions shift between northerly and southerly trends, and each cycle persists for >1.5 days (Figure 2.2b). In particular, during the rising stages of the three peaks, the flows are to the north, while during recession they are to the south (Figure 2.2b). Gradients associated with the falling limbs are slightly larger than during the rising limb, with a mean of $0.11 \times 10^{-4} \pm 0.069 \times 10^{-4}$ and a maximum of 0.43×10^{-4}.

At T_K, for stages of about 27.98–28.76 m, flow directions are largely to the southeast, with occasional rotations to the east-southeast (Figure 2.2c). The gradient values vary within a range of 1.1×10^{-4} and seem independent of stage and rate of change in stage. However, as the stage approaches 28.76 m, the vectors become proportional to stage height, but peak stage occurs about one half-day after peak gradient. On the other hand, for the slightly higher hydrograph of April, flows differ substantially for stage >28.76 m (Figure 2.2d). From April 6 to 11, weak flows are to the south, but on ~April 11, there is a short-lived factor of 3 increase in southerly gradient that precedes a current reversal (Figure 2.2d). From April 11 to 20, flows are to the northeast and gradients appear strongly correlated with stage, and the cycle is repeated. Flow paths are directed northeast when stage exceeds bank elevation (Figure 1b). This is in stark contrast to flow paths for stages <28.76 m (Figure 2.2c), where flow paths continue southeast, even after the stage exceeds the local bank elevation. Mean and maximum gradients during lower stages are $0.1 \times 10^{-4} \pm 0.061 \times 10^{-4}$ and a maximum of 0.36×10^{-4}, which are substantially smaller than observed during higher, albeit sub-bankfull flow, where gradients have a mean $0.39 \times 10^{-4} \pm 0.32 \times 10^{-4}$ and maximum 1.1×10^{-4}.

In summary, the sub-bankfull inundation process gives rise to temporally and spatially complex flow patterns identified through analyses of free surface gradients. The flow system complexity is exemplified through current reversals that occur in response to a threshold in stage. On the other hand, at lower levels of inundation, flows tend to have a preferred orientation, mostly to the south. Also, hydrograph peaks have a maximum gradient that is not correlated with maximum stage; in one example, it precedes the maximum and in the other it occurs after the peak has passed.

2.4.2 OVERBANK INUNDATION

Overbank flows are apparent as a ~2 m rise in stage at both T_F and T_K (Figure 2.2e and 2.2f), and gradient magnitudes have a mean of $0.80 \times 10^{-4} \pm 0.62 \times 10^{-4}$ and a maximum of 2.18×10^{-4}. During November 12–15, the gradients are initially low, but they double within a day before declining to below the initial values by November 14.5.

Thereafter, they steadily increase and attain peak values that correspond with the peaks in the hydrographs at ∼31.39 m on November 18. The gradual increase is accompanied by a ∼20° easterly rotation before returning to due south on November 21 when the stage is at 30.20 m. Overall, for site T_F, the response is substantially subdued relative to the sub-bankfull responses (Figure 2.2a and 2.2b).

As with T_F, the gradients for T_K are initially small, the lowest gradients directed southward (Figure 2.2f). After 2 days, the vectors rotate >90° resulting in north-northeasterly flows, and they increase with stage, reaching a maximum value at less than halfway along the rising limb. As stage continues to rise, flows rotate to the east and gradients decline; hence, the peak gradient precedes peak stage by nearly 4 days. As the stage continues to rise, the flows become more easterly until November 20 when the falling limb stage is at ∼29.49 m. Thereafter, the gradients are to the northeast with a declining stage (Figure 2.2f). Overall, gradients are not directly associated with stage, with a maximum of 2.72×10^{-4} and gradients do not acquire similar magnitudes during the falling as for the rising limb, for the same stage. The mean gradient is $1.31 \times 10^{-4} \pm 0.57 \times 10^{-4}$. The occurrence of the magnitude maximum during early increase in stage is different from observed gradients during sub-bankfull inundation and for T_F (Figure 2.2e), where gradients appear to be proportional to stage.

In summary, inundation by overbank flow leads to inconsistent maximum gradient responses between sites. In one case, maximum gradient is directly proportional to stage, while in the other the relationship is the inverse. Moreover, despite the higher overbank stage, the maximum gradients are associated with sub-bankfull flow. On the other hand, flow reversals are limited to sub-bankfull conditions, although there is substantial flow vector reorientation for bankfull.

2.4.3 FLOW VELOCITY

At site T_F, for stages <30.08 m, maximum flow velocity of 0.06 m/s occurs at a stage of 30.03 m on the rising limb, and it is northward, while average velocity is 0.03 ± 0.01 m/s (Figure 2.2a). For depths >30.08 m, but still sub-bankfull, the largest velocities occur at a stage of 30.21 m, reaching 0.06 m/s, while the mean velocity is 0.02 ± 0.01 m/s (Figure 2.2b). For overbank inundation, a velocity maximum of 0.23 m/s occurs, while it averages 0.10 ± 0.06 m/s, and the largest velocity is obtained at a stage of 31.13 m prior to the maximum stage (Figure 2.2e).

For site T_K, at <28.76 m stage, flow is limited to 0.04 m/s with a mean of 0.01 ± 0.001 m/s. Maximum velocity of 0.04 m/s occurs at a stage of 28.61 m, during falling stages and is toward the southeast (Figure 2.2c). For the slightly higher hydrograph, depths >28.76 m result in a maximum velocity of 0.11 m/s with an average of 0.05 ± 0.03 m/s (Figure 2.2d); maximum velocity precedes maximum stage. Overbank inundation results in an average velocity of 0.13 ± 0.06 m/s with a maximum of 0.22 m/s. The magnitudes of velocity appear to be related to stage, with the maximum velocity occurring at maximum depth, likely resulting from the effects of increased depth in the Manning expression. Overall, these estimated velocities compare favorably with those reported from floodplain field studies giving a range of 0.01–0.67 m/s (*Arcement & Schneider, 1989; Girard et al., 2009; Harvey et al., 2009*).

Overall, we apply a technique novel to floodplain research to show that floodplain flows can be predictably simple and highly complex in time and space. We found that the controlling factors on flow dynamics are largely a function of stage and rate of change of stage, where the rate of change is largely controlled by the style of inundation. In particular, we show that sub-bankfull inundation and overbank inundation influence the rate and magnitude of changes in stage and these, in turn, impart distinctly different features to the prevailing flows (Figures 2.2a–2.2d vs. Figures 2.2e and 2.2f).

2.5 DISCUSSION AND INTERPRETATIONS

To glean deeper insight into processes governing the wetting, circulation, and draining of inundated landscapes, we present a method that is a compromise in spatial scale between point measurements from acoustic devices and satellite remote sensing of water surfaces, the two most common approaches of direct measurement. Given the minimum surface area of individual sensor deployment triangles, we propose that the triangular facet provides “mesoscale” observations of average flow conditions. Moreover, in assessing system flow dynamics, these free surface measurements can be considered, at times, superior to point measurements from velocimeters as acoustic signals can be degraded by large and small floating debris or sediment accumulation on acoustic sensor heads. In these cases, the pressure sensors are only marginally affected. Also, the facet data provide a tremendous advance over satellite remote sensing in that the latter may be complicated by forest canopy or are acquired over a large spatial scale. Finally, the facet data can be acquired every few minutes, much more frequently than satellite passes. Overall, the facet approach creates new research opportunities for inundated landscape hydrodynamics. Also, the facet approach has inherent flexibility in that any number of pressure sensors can be arranged in any number of configurations, and within each configuration occurs multiple sets of adjacent triangles. Hence, the facet approach can promote the creation of new knowledge on local to broader scale flow dynamics over inundated landscapes.

Although the facet method does not provide direct point measurements of water velocity, or velocity profiles, as with autonomous acoustic devices, it could be used to augment such measurements over larger spatial scales. Additionally, acoustic devices that record velocity data at the 0.25-hr interval of this study will have a limited battery life of ~0.1 year, whereas the pressure transducers used here can record data for ~1.5 years before running out of memory. This notwithstanding, we propose that a combination of acoustic and facet field data can be expected to more fully represent complex flow systems or system dynamics, and thereby shed greater light on, for example, floodplain hydraulic connectivity, a topic of increased interest requiring transdisciplinary approaches over small and large temporal and spatial scales (e.g., *Passalacqua et al., 2017; Wohl et al., 2019*).

At our floodplain study site, the gradients computed at T_F and T_K for sub-bankfull flows show that local flow dynamics are threshold dependent. The threshold is governed by the elevation at which flows in floodplain networks merge and inundate the local topography, similar to the initiation of infiltration excess overland flow that occurs with the infilling of local storage (e.g., Horton overland flow). Further, field observations reveal that channel networks at each site become connected at different stages and flow during low stages the connections occur through channel networks. When the stage exceeds the threshold, the free surface gradients of the rising limb may be nearly opposite or perpendicular to directions observed on the falling limb. Meanwhile with stage below the threshold values, the flow orientations are approximately uniform (Figure 2.2). Therefore, we infer that the channel network-linking determines and limits potential flow pathways, and thus control directional variability.

Moreover, we demonstrate the utility of the triangular facet approach to estimating flow direction and speed that are representative of mesoscale flows averaged over ~0.01 km^2. This approach and corresponding results are not limited by the uncertainties of decimeter or small-scale point measurements of acoustic devices, nor the impediments to acquiring remote sensing data. The facet approach provides new knowledge with respect flow dynamics. Further, this mesoscale insight provides a foundation for an improved understanding of floodplain dynamics and hydraulic connectivity of a floodplain (e.g., *Wohl, 2017*) at a much higher temporal frequency than can be acquired with satellite remote sensing, and at a much finer spatial resolution.

Overall, we show that flows and currents estimated with the facet approach shed light on understanding flow processes, and can be used to help guide the development of hydrodynamic models, and help target questions to be addressed through simulations. For example, the approach can identify locations where a highly resolved computational domain of subtle topographic features may be necessary to detect and understand the role of complex mesoscale hydrodynamic processes in floodplain hydraulic connectivity, ecosystem responses, and floodplain sustainability. Further, the corresponding stage, gradient, and flow direction data provide a robust data set necessary to effectively assess a model's capability of resolving spatial variation floodplain hydrodynamics. We contend that the combination of multiple pressure readings and corresponding flow directions and inferred velocities that all arise from the application of the facet method can enhance validation of numerical simulations and thereby improve their representation of actual field conditions (e.g., *Czuba et al., 2019; Kupfer et al., 2015*). Hence, the "triangular facet" approach to assessing inundated landscape flow dynamics helps fill a knowledge gap regarding inundation–drainage processes and it provides multiple data sets for model and remote sensing validations.

2.6 CONCLUSIONS

An in situ three-point approach for the estimation of mesoscale (~0.01 km^2) free surface gradients and flow directions for inundated landscapes is presented as the "triangular facet approach." Analyses of the maximum gradient data acquired at, and averaged over, 0.25-hr intervals show that floodplain flows can be predictably simple or complex, for different water stages and between locations, and the effects are largely controlled by inundation process. Flows during sub-bankfull inundation are particularly variable, including multiple abrupt flow reversals, while overbank inundation gives a more subdued response with slow ~90° rotations. During sub-bankfull inundation, the local relic geomorphic structures influence flows that are routed through the floodplain interior. However, with higher overbank flows, the rate of change of stage is a more important driver of flow complexity than local relief. Overall, the triangular facet approach provides robust information on flow dynamics that can greatly enhance the utility of data from satellite remote sensing and acoustic current measuring devices, and numerical simulations of flow.

DATA AVAILABILITY STATEMENT

The lidar data set are available from NOAA Digital Coast website at https://chs.coast.noaa.gov/htdata/lidar1_z/geoid18/data/4815/. The river stage and discharge records at the USGS stations are available at https://waterdata.usgs.gov/sc/nwis/uv?site_no=02169625 (Congaree River at Columbia, SC) and at https://nwis.waterdata.usgs.gov/nwis/inventory/?site_no=02169625 (Congaree River at Congaree National Park near Gadsden, SC). All water depth data are available at https://doi.org/10.4211/hs.eab35a0af8104dd5921ef3ebbefddd87. All URLs were accessible as of August 15, 2021

CHAPTER 3

FLOODPLAIN SURFACE-WATER CIRCULATION DYNAMICS: CONGAREE RIVER, SOUTH CAROLINA, USA[2]

A robustly calibrated and validated hydrodynamic model depicts flow patterns over a topographically complex floodplain with a heterogeneous main channel levee. Simulations highlight floodplain inundation dynamics for two conditions, the passage of sub-bankfull and overbank flood waves. Sub-bankfull inundation commences with the passage of the flood wave crest beyond the lower elevation levee breaches, and floodplain wetting is guided by the channel network. Hence, the upstream sub-bankfull inundation area expands while much of the downstream floodplain remains dry. The onset of overbank flow is spatially variable but becomes continuous, and the through-bank channels persist as preferential pathways that produce higher velocity flows several kilometers inland. Meanwhile, near-stagnant zones develop between through-bank channel mouths, where water is temporarily stored and routed to the channel network. Also, 48% of the inundation water is from the river while 52% enters the study area from the upstream floodplain. Overall, floodplain wetting and draining processes significantly influence flow direction, and characteristics of the flood wave over the floodplain surface such that a single stage in the main channel does not uniquely define floodplain flow hydraulics. Given these findings

---

[2] van der Steeg, S., Torres, R., Viparelli, E., Xu, H., Elias, E., & Sullivan, J. Floodplain Surface-water Circulation Dynamics: Congaree River, South Carolina. *Water Resources Research*, e2022WR032982.

we propose that assessments of floodplain hydraulic connectivity account for the effects of heterogeneous levee structure and intra-floodplain exchanges, as well as the typical flow thresholds associated with submergence and emergence of topography.

3.1 INTRODUCTION

Floodplains typically are low relief but topographically complex landscapes (e.g., *Xu et al., 2020; Park, 2020; Lewin and Ashworth, 2014*) with a structure reflecting the range of drivers operating at different temporal and spatial scales (e.g., *Dunne and Aalto, 2013; Trigg et al., 2012; Mertes et al., 1997*). Floodplain features are readily identifiable in satellite imagery for large rivers (e.g., *Mertes et al., 1997; Rowland et al., 2009; Lewin & Ashworth, 2014*), and in data from airborne lidar for much smaller systems (e.g., *Xu et al., 2020; Lindroth et al., 2020; David et al., 2017;*). These data reveal that floodplains often contain extensive channel networks (e.g., *Xu et al., 2020; David et al., 2017; Fagan & Nanson, 2004*), including networks originating with levee breaches (*Lewin and Hughes, 1980; Xu et al., 2021; Day et al., 2008;*).

Likewise, floodplain hydraulic connectivity, defined here as the degree of surface water exchange between a river and its floodplain (e.g., *Amoros and Bornette, 2002; Passalacqua, 2017; Wohl et al., 2019),* can be expected to vary considerably with variations in stage (e.g., *Amoros & Bornette*, 2002*; Xu et al., 2021; Czuba et al., 2019*). For instance, floodplains may experience frequent low-magnitude floods under high, but below bankfull river stages (e.g., *Xu et al., 2021; Pinel et al., 2021; Day et al., 2008*) giving rise to sub-bankfull inundation. Discrete river-floodplain segments may experience the simultaneous occurrence of sub-bankfull and overbank flooding, or no flooding at all depending on heterogeneity in the along-channel and vertical structure of riverbanks and levees. The net result is highly a variable and complex floodplain flow (*Xu et al., 2021*), that can present abrupt current reversals (*van der Steeg et al., 2021*). Hence, complex flow dynamics develop in response to along-channel variations of river-floodplain coupling-decoupling, and by flow interactions with local topography. Indeed, complex floodplain flow dynamics have been reported by remote sensing (e.g., *Alsdorf et al., 2007; Hamilton et al., 2007; Mertes, 1997*) and by direct field observations (*Girard et al., 2009; Filgueira-Rivera et al., 2007; van der Steeg et al., 2021*).

For detailed analyses of flows over a floodplain, researchers often resort to process-based hydrodynamic models (e.g., *Pinel et al., 2020; Byrne et al., 2019; Czuba et al., 2019*). One major advantage of numerical flow modeling is the capability to increase the spatial and temporal resolution of point-oriented field observations. If constrained with suitable field data, model results can provide near-realistic predictions of flows with high spatial and temporal resolution, which allow for hydrodynamic assessments across the model domain. Recent floodplain modeling efforts provide insight into floodplain flows, but the model constructs lack sufficient calibration to account for realistic, time-varying flow conditions (e.g., *Tull et al., 2022; Pinel et al., 2020; Czuba et al., 2019*). For example, *Czuba et al.* (*2019*) highlight how floodplain channels affect hydraulic connectivity under steady boundary conditions. This approach precludes the assessment of inundation dynamics of floods with highly variable stages. Similarly, *Tull et al.* (*2022*) used quasi-steady boundary conditions to demonstrate that during sub-bankfull river stages complex floodplain flows can result due to prior flooding. This approach improves on the work by *Czuba et al. (2019)* but it provides limited insight on flow processes because the boundary conditions fail to represent actual drivers of system dynamics, hence advances in floodplain science through numerical modeling require the application of unsteady forcing conditions. In addition to representative boundary conditions, models require careful incorporation of floodplain structure (i.e., topo-bathymetry) as part of the computational grid (e.g., *Yamazaki et al., 2012; Neal et al., 2012; Verwey et al., 2001*). This approach requires a priori knowledge of often overlooked floodplain channel networks (e.g., *van der Steeg et al., 2021; Xu et al., 2020; Wohl et al., 2011*) and a priori knowledge of flow processes.

Finally, an insightful modeling strategy also should include opportunities for “intra-floodplain” exchanges. In other words, models should have the flexibility to account for floodplain fluxes into and out of the immediate study site or domain of interest. By excluding this modeling capability, the modeler implies that flow dynamics are principally linked to river stage (*Czuba et al., 2019, Byrne et al., 2019*) or stage plus ponding (*Tull et al., 2022*).

The work presented here applies: 1) dynamic boundary conditions based on observations, 2) an entire floodplain computational domain much larger than the area of interest, 3) detailed measurements of channel bathymetry in the computational grid, and 4) a well-developed calibration and validation protocol with long term field observations. Motivation for this work is driven by a dearth of information on overall water circulation in the absence of steady state drivers. This work is also expected to highlight floodplain drainage, a poorly documented process. We hypothesize that interactions between floodplain structure and hydrograph shape result in complex floodplain inundation and drainage patterns. A robustly calibrated and validated Delft3D Flexible Mesh numerical flow model is presented, and simulations are forced to be as-realistically-as-possible (i.e., quasi-real-time) by multiple sets of observations. Model results represent synoptical, near-realistic views of high spatial and temporal resolution flow dynamics to acquire new knowledge on the characteristics of, and controls on floodplain wetting, circulation and draining.

3.2 STUDY REGION AND HYDROLOGIC CONDITIONS

The study site is the ~93 km^2 floodplain of the Congaree National Park (CNP) and the surrounding floodplain, from Columbia (Figure 3.1a) to the Wateree River. The entire floodplain is ~60 km long and on average, about 4.5 km wide, with a total area of ~300 km^2. The park has been held in conservation since the mid-1970s to aid in the preservation of the large stands of old growth tree communities *(Kinzer, 2017)*. CNP is bound by the Congaree River to the south, bluffs to the north, and the Wateree River to the east. The floodplain has almost complete forest cover where ~80% of the canopy is above 10 m. Two small, upland tributary channels discharge water to CNP (Figure 3.1a; *Xu et al*., 2021), but they contribute little to the overall water prism (e.g., *Doyle, 2009*).

Within the park, floodplain elevation declines from 35 to 23.5 m (Figure 3.1b), resulting in an average valley gradient of ~4×10^{-4} m/m (*Xu et al., 2020*). The main channel consists of straight and relatively stable meandering reaches (*Williams et al., 2017*; Figure 3.1b). Channel width varies between 80 and 160 m and the reach-averaged riverbed gradient is 1.5×10^{-4} m/m. Bank and levee height are highly variable, thereby facilitating irregular inundation patterns (*Xu et al., 2021*). The levees in the upstream part of the study reach require high river stage for overbank inundation, while levees downstream are less developed and overbank inundation occurs at lower stages.

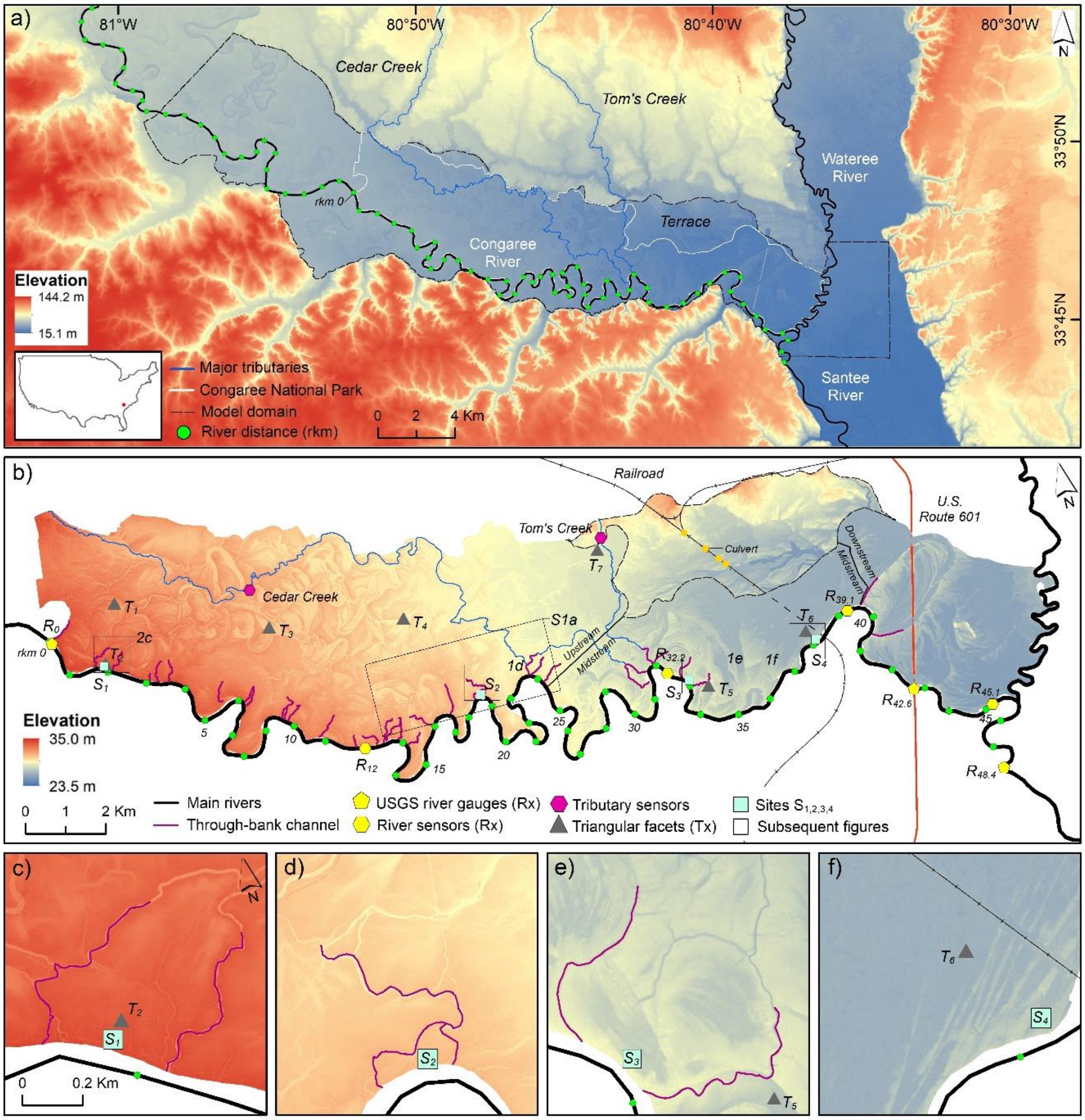

Figure 3.1: Study site. (a) Regional DEM of the Congaree-Wateree-Santee River floodplain valley. The model domain includes regions outside of CNP necessary for determining accurate model results within the park. Cedar Creek and Tom's Creek are two major tributary channels. (b) DEM of Congaree National Park. The two solid lines divide the floodplain into three reaches: upstream, midstream, and downstream. (c-f) subarea of the DEM showing detailed topography surrounding the near-bank locations (S_1, S_2, S_3, S_4)

Within the park boundary are 32 well-developed through-bank channels, having mouth widths ranging from 7 to 30 m (*Xu et al., 2020, 2021;* Figure 3.1b). Some channels are anthropogenic and extend hundreds of meters into the floodplain. Other channels are parts of natural networks that extend up to several kilometers inland (*Xu et al., 2020*) and thereby connect the river with an expansive network of channels, conduits and isolated depressions of the floodplain interior. Across the river from the park the local floodplain area is fragmented by active land use with agricultural dikes, ditches, and roads, comprising 19% of the total local floodplain area. This part of the system has limited access due to private ownership; hence, these conditions led us to focus the field observations on the much larger CNP floodplain (Figure 3.1).

For reference, the along channel distance is reported with the prefix “rkm” for “river kilometer”, with rkm 0 at the upstream park boundary, increasing downstream. Railroad (rkm 38.3) and highway (rkm 42.6) berms are the major anthropogenic structures in the floodplain, consisting of embankment-bridge systems, that likely affect floodplain circulation during high flows (*Sharitz & Allen, 2009; Patterson et al. 1985; Shelley, 2007*). The railroad embankment extends 3.7 km into the floodplain, after which the bridge is supported by 4.5 by 6.8 m piers, spaced ~50 m apart that continues for 1.8 km (Figure 3.1b). The embankment has three 4 m high culverts that allow for water passage at times of exceptionally high flow (*Kinzer, 2017*). The highway embankment, locally interrupted by a pillar structure to allow for the passage of water, runs for 3.5 km into the floodplain and the pillar structure with 2.5 m diameter circular pillars, spaced ~35 m apart, continues 0.3 km (Figure 3.1b).

The United States Geological Survey (USGS) Congaree River gauge in Columbia, SC (#02169500) provides the nearest long-term discharge and stage records, and it is located 38 river kilometers upstream. The discharge from 1984 to 2021 ranges from 30 to 4200 m^3/s and water levels vary between 35 and 43 m. Data from the USGS Gadsden station (#02169625), rkm 0 (Figure 3.1b), show that since 1984 the local stage (discharge not reported) varies by 8 m. Further downstream at rkm 42.6 (Figure 3.1b) the USGS Highway 601 station (#02169750) was established in 2018 and records water levels and daily mean discharge only. Here, the water level signal is subdued relative to the Gadsden station; the range of 4.5 m is likely associated with poor levee development (*Xu et al., 2021*). Within the park, the USGS records water level at Cedar Creek (USGS Cedar Creek station, #02169672, Figure 3.1b). Water levels at this location are affected by both river inundation and runoff from upland source areas (*Xu et al., 2020*; *Shelley et al.*, 2012). Two additional gauging stations outside of the study area provide water levels for the Santee River (USGS Santee River in Fort Motte, #02169810, rkm 48.4) and for the Wateree River (USGS Wateree River in Camden, #02148000, north of the study region, not shown Figure 3.1). Flood wave travel time between the Gadsden and Santee gauges (distance ~ 48.4 rkm) depends on stage. Sub-bankfull wave crests traverse the distance faster (49 ± 8 hrs) than overbank flows (63 ± 3 hrs). Inundation intervals vary across the floodplain; for sub-bankfull inundation, the wetting period is 8.4 ± 5.6 days, while for overbank exchange the period is 19.6 ± 7.7 days, and mostly during the winter and spring (*Kinzer*, *2017*).

The floodplain structure is highly variable, but it is arranged into sections with distinct geomorphic frameworks (after *Xu et al., 2021*; Figure 3.1b): upstream (rkm 0 to 24.2), midstream (rkm 24.2 to 39.5), and downstream (rkm 39.5 to 45.3). Within these sections, four locations were selected for the analyses of flow dynamics along the riverbanks. The first site, S_1 (rkm 2.9) is at the bank in the upstream reach (Figure 3.1b). Two of the through-bank channels (TBCs) cut through the levees at rkm 2.7 and 3.1, surrounding the observation location, but the channels and the network are not extensive

(Figure 3.1b). S_1 has an average elevation of 32.26 ± 0.36 m and requires higher river stage for overbank exchange to occur relative to the midstream sites. Site S_2 at rkm 18.8 is also in the upstream but at an elevation of 29.21 ± 0.34 m. Local TBCs occur at rkm 18.6 and 18.9. Site S_3 at rkm 33 is in the midstream reach but in a local depression adjacent to the main channel, and at 25.96 m. Likewise, TBCs occur 200 m upstream and 100 m downstream of the site. The levee near S_3 has an average crest elevation of 27.12 ± 0.41 m and the downstream TBC is directly connected to the S_3 depression via a channel network that loops around and enters the depression from the northeast. Site S_4 is also in a depression near the railroad tracks at rkm 38, at an average elevation of 24.99 ± 0.31 m. S_4 has no TBCs, however, the poorly developed levee contains multiple low laying sections that allow for heterogenous sub-bankfull exchange.

3.3 METHODS

3.3.1 FIELD DATA COLLECTION

River water depth and bank elevation at four locations along the main channel were collected using *Onset HOBO U20* absolute pressure transducers (hereafter "sensors") at rkm 12, 32.2; 39.1; and 45.1 (Figure 3.1b). Pressure readings were compensated for atmospheric pressure with an identical sensor deployed as a barometer. The resulting pressure readings were converted to water depth using the *Onset HOBOware* software suite. All water levels were converted to a common vertical reference (NAVD88) using a *Trimble R10* GPS (horizontal and vertical accuracy ± 0.015, 0.025 m, respectively). Elevation measurements of bank height were combined with water level readings to determine the occurrence of sub-bank and overbank flow conditions (after *Xu et al., 2021*).

To characterize the fine scale structure of currents in response to flood waves over the floodplain in-situ measurements were collected using a total of 22 sensors. Of this set, 21 sensors were arranged in 7 approximately equilateral triangles with vertices ~200 m apart (T_{1-7}; Figure 3.1b). Separately, these sensors provide water level measurements at each point, and with each triangular configuration flow direction can be estimated for a ~0.1 km^2 area (*van der Steeg et al., 2021*). Furthermore, to augment the inland Cedar Creek data, one sensor was installed in Tom's Creek, a channel draining a local upland watershed (Figure 3.1b), and about 7 m wide.

3.3.2 NUMERICAL FLOW MODELING

To quantify flow dynamics and the coupling-decoupling of the river-floodplain system, the open-source Delft3D Flexible Mesh modeling suite (Delft3D FM) is used in depth-averaged mode (2D) (*Deltares, 2022a,b)*. Hydrodynamic modeling of the field site is challenging due to the highly variable inundation patterns (*Xu et al., 2021*), and the complex, albeit low relief topography and their interactions (e.g., *Yamazaki et al., 2011; Neal et al., 2012; van der Steeg et al., 2021*). Also, the dynamics of wetting and drying (*Lewin & Hughes*, 1980) further complicate the problem. Previous research, however, demonstrated that the process-based Delft3D FM modeling suite applied to both tidal and river wetland systems is capable of accurately simulating flow processes (e.g., *Stevens et al., 2021; Muñoz et al., 2021, Straatsma & Kleinhans, 2018*).

A detailed description of the model set-up for this study is provided in *Appendix 3.1*. The model was forced with unsteady discharge and water level boundary conditions obtained from USGS gauging stations (Figure 3.1). Surface and bed roughness were schematized using the Manning formulation, which relates bed friction to water depth. The roughness coefficients were described during the calibration and validation process and initial estimates were guided by *Arcement and Schneider (1989)*, and *Barnes (1967)*. Model calibration and validation focused on the accurate representation of 1) water level in the main channel 2) water level in the floodplain, 3) flow direction and 4) flow gradient over the floodplain. Simulated water levels were compared with observed water levels from six locations in the river (R_{1-6}, Figure 3.1b), and seven locations in the floodplain (T_{1-7}, Figure 3.1b) for varying river discharge conditions. Simulated flow direction and gradient in the floodplain were compared to observations using the 'triangular facet approach' (*van der Steeg et al., 2021*) for model validation. Model sensitivity for flow was examined for a range of spatially varying Manning roughness coefficients in multiple but otherwise identical simulations.

To accurately capture floodplain processes, a flexible mesh computational grid with a varying spatial resolution, guided by topo-bathymetric measurements and floodplain channel extraction (*Xu et al., 2020*), was constructed through a grid independence analysis, but over a much larger domain of 247 km^2 including the Wateree and Santee rivers, inclusive of the eastern floodplain (Figure 3.1a; 247 km^2 versus 93 km^2). The larger domain was required to account for "intra floodplain" water exchange (i.e., floodplain valley flows into and out of the CNP study site). Floodplain channels were delineated by higher resolution grids, guided by geomorphic floodplain feature extraction results (Figure A.1; *Xu et al., 2020)*. Furthermore, sensitivity testing revealed that a realistic and unsteady modeling approach using boundary conditions developed from observations is necessary to accurately represent complex floodplain flow processes. For example, the flow reversals of Figure 3.2 could not be reproduced in model configurations using the steady- or quasi-steady boundary conditions of *Tull et al*., (2022), *Czuba et al*., *(2019*), and *Meitzen (2011*).

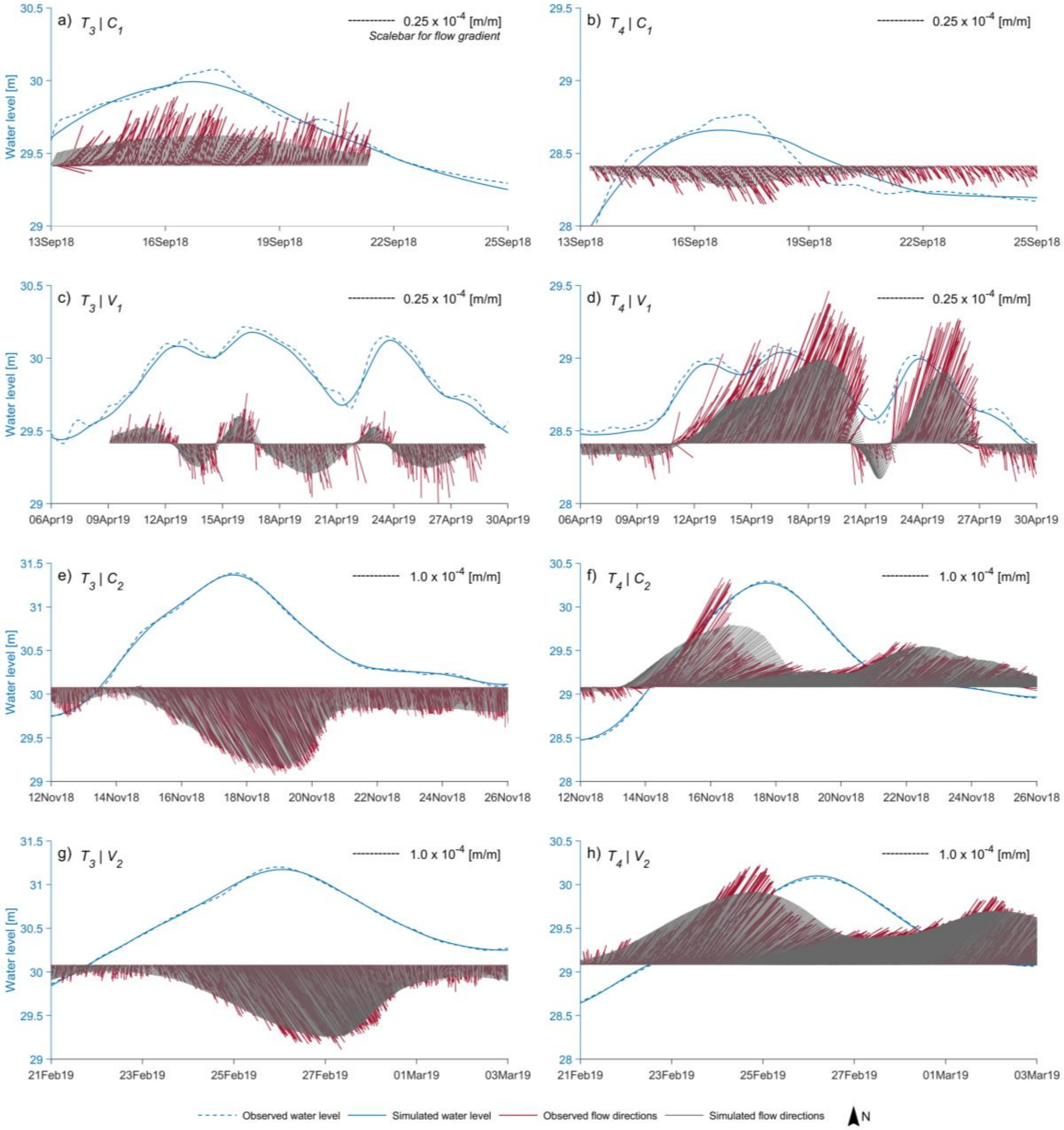

Figure 3.2: Comparisons of observed and simulated water levels and flow directions for two observation locations in the floodplain interior. Dates are formatted as day/month/year. Model performance for other observation sites is presented in *Appendix A.2*. See Figure 3.1b for the along-channel locations of sensors. Vectors indicate magnitude and direction, with north at the top. Flows to the north are generally directed into the floodplain while flows to the south are toward the main channel. Note, due to thinning of the data, each vector represents a 2-hour interval. C_1: lower sub-bankfull calibration scenario; V_1: higher

sub-bankfull validation scenario; C_2: higher overbank calibration scenario; V_2: lower overbank validation scenario.

Two separate calibration hydrographs were required: one for sub-bankfull (C_1, Figure A.2a) and one for overbank (C_2, Figure A.2c) flow processes. For C_1, the water levels in the river are below bankfull and water enters the floodplain as through-bank (breach) flow. For C_2 water enters as both overbank and through-bank flow. A spatially varying roughness field consisting of six different Manning roughness coefficients (*Appendix A2*) was required to determine accurate model results, largely based on geomorphic features defined by *Xu et al., (2020*), and local to regional gradients. Moreover, the model was successfully validated with sub-bankfull (V_1, Figure A.2b) and overbank (V_2, Figure A.2d) flow events in otherwise identical model configurations, but model performance is better for higher flow events. Simulated water levels had an average total RMS of 0.02 ± 0.05 m and 0.07 ± 0.05 m respectively in the river and the floodplain (Figure 3.2, *Appendix A.2*). The maximum average deviation for flow directions is 39°± 18°, while the magnitude of the free surface gradients has a maximum error of 51%.

As with all numerical studies, the hydrodynamic model and simulation outputs have an inherent uncertainty resulting from the schematizations and approximations of real-world flow processes, and computational time restrictions that may impact the interpretation of results. Nevertheless, for the calibration and validation the model accurately represents the flow processes of interest. Also, by focusing the analyses of model results at scales beyond a single computational cell (i.e., grid-cell averaging), we show that valuable insights in floodplain flow processes can be obtained. An overview of model limitations is provided in *Appendix A.3*.

3.3.3 ANALYSES OF FLOODPLAIN CIRCULATION

The hydrodynamic response is evaluated at high temporal resolution (15 min intervals), at multiple sites ($S_{1,2,3,4}$) near the riverbanks and in the floodplain interior (Figure 3.1b). The near bank sites allow us to readily differentiate between sub-bankfull and overbank exchanges, and circulation. Furthermore, these sites are representative of the spatially varying geomorphic conditions along the riverbanks, from reaches with well-developed, high gradient levees with TBCs to sections with poorly developed levees and no TBCs. Therefore, data pertaining to these sites will improve comprehension of inundation and drainage, and the influence of breaches on the dynamics of river-floodplain coupling and exchange. Their locations are fundamental elements of river-floodplain interactions (e.g., *Tull et al., 2022; Byrne et al., 2019; Czuba et al., 2019; David et al., 2017*) and they produce a type of “fuzzy” inundation (*Xu et al., 2021*). Flow vectors were averaged over 25 cells (excluding dry cells) of ~150 m^2. Averaging of flow vectors damps any spurious model outputs and ensures more representative products.

Analyses at a larger (>150 m^2) spatial scale help characterize general, system-wide flow patterns during multiple events differentiated by the type of river-floodplain exchange. Both inundation extent and flow vectors (directional and velocity magnitude) were extracted from the model output. For overbank inundation events, flow vectors were aggregated (based on their means) to a coarse ~400 m grid and are only shown for inundation depths larger than 0.05 m. This decision is expected to enhance the visualization and interpretability of model results. For sub-bankfull inundation, the automatic clustering of flow vectors to a ~400 m or finer grid was inadequate for visualization and interpretation of model results. Part of the problem is related to the nature of sub-bankfull flow dynamics that occur at scales of ~20 m or smaller with floodplain channels, or 20-100 m for other floodplain features. Therefore, fine clustering will enable flow visualization at scales of 100s of meters, but for the entire CNP (1000s of meters) it would be inadequate. Thus, for sub-bankfull inundation, vectors were hand-selected and clustered to ensure relevant flow dynamics can be graphically represented. Both inundation extent (depths > 0.05 m) and flow vectors were assessed at rkm -20, -10, 0, 10, 20, 30, 40, 50 with respect to the along-channel wave crest (i.e., the highest peak) propagation. By tracking the wave crest in this manner and visualizing the inundation extent and flow vectors, the model output can be managed to provide meaningful spatial and temporal coverage of flood waves through the system. Further, this approach allows for simultaneous evaluation of the rising and falling stage, and flow dynamics (e.g., flooding and drainage).

3.4 RESULTS

Flow dynamics and large-scale circulation patterns were analyzed for one sub-bankfull and one overbank inundation event used to calibrate and validate the model. The results for the sub-bankfull inundation corresponds to the hydrograph for flow scenario V_1 (Figure 3.2c and 3.2d, 3.3a and 3.3b, and A2b) and the overbank inundation response for C_2 (Figure 3.2e and 3.2f, Figure 3.3c-3.3f and Figure A.2c). The near-bank results are presented using combined stage and flow vector diagrams (Figure 3.3); flows to the north are directed into the floodplain while flows to the south are toward the main channel. Larger-scale circulation patterns are presented using both spatially averaged flow vectors and inundation extent (Figure 3.4 and Figure 3.5)

3.4.1 NEAR-BANK FLOW DYNAMICS

3.4.1.1 SUB-BANKFULL INUNDATION

Sub-bankfull inundation associated with V_1 is driven by a hydrograph with three crests several days apart, and water depths up to 0.9 m at the near-bank sites (Figure 3.3a and 3.3b). The rising and falling limbs are 2-3 times steeper near the river (Figure 3.3a and 3.3b) compared to the floodplain interior (Figure 3.2c and 3.2d). During sub-bankfull inundation, only sites S_3 and S_4 experienced inundation. At S_3 (Figure 3.1b), on 10 April, for stages < 26.62 m, the flow is initially directed to the southwest (Figure 3.3a). Above 26.63 m it gradually rotates ~200° clockwise to the north, and persists for ~2.5 days (10.5 – 13 April) with a maximum gradient of 0.52×10^{-4} on 11 April. On the falling limb of ~12 April, with stages below 26.67 m, the gradient decreases and flow rotates clockwise, to the southeast, toward a local TBC (Figure 3.3a, 13 April). On the rising limb of the 14 April peak, flows rotate to the north when the stage exceeds 26.62 m and persists for ~4.5 days. The higher gradients fluctuate with stage and the maximum of 0.60×10^{-4} occurs on 15 April. The 19 April falling limb, for stages from 26.58 m to 26.67 m, flow rotates to the southeast and persists for ~0.5 days, but at stage <26.58 m flows gradually rotate to the northeast. The cycle between southwesterly and northerly flows on the rising limb, and between northerly, southeasterly, and northeasterly flows on the falling limb is repeated for the remainder of the hydrograph and denote an elevation threshold for flow direction.

Meanwhile, the S_4 site initially has flows towards the south with occasional rotations to the southeast, but with a maximum gradient of 0.16×10^{-4} (Figure 3.3b). On ~11 April, as stage approaches 24.99 m, the flow rotates toward the northeast. Here, the flow magnitude appears to be proportional to stage, with a maximum gradient of 0.26 ×

10^{-4} occurring near peak stage. On the falling limb of the first peak on 13 April, water movement continues northeastward until the stage falls below 25.07 m, after which the general water movement is towards the southwest. The southeasterly and northeasterly flows on the rising limb, and the northeasterly and southwesterly flows on the falling limb are repeated (Figure 3.3b). These observations indicate that the flow reversals are stage dependent. Also, the surface gradient magnitude is strongly correlated with stage, with a maximum of 0.51×10^{-4}.

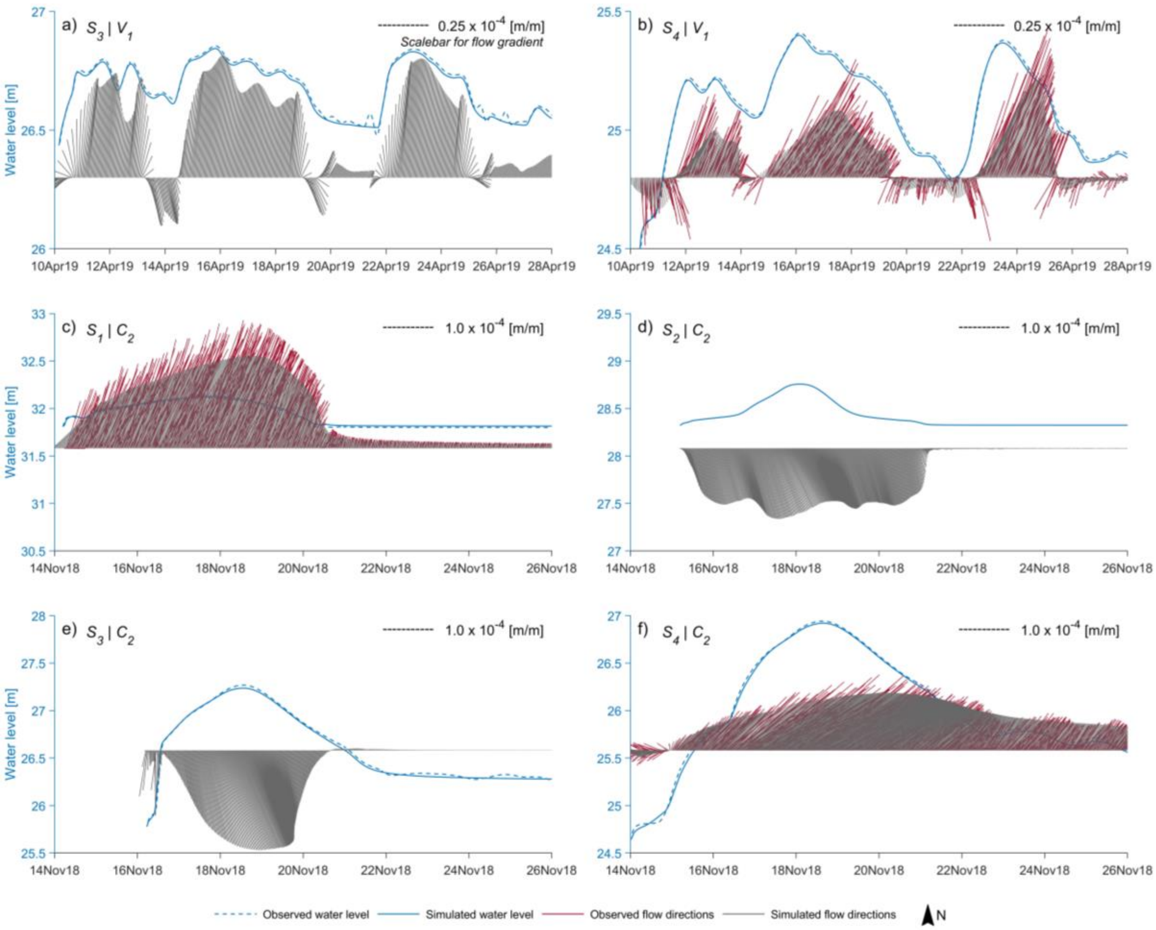

Figure 3.3: Observed and simulated results of flow dynamics of sub-bankfull inundation (flow scenario V_1) at S_3 and S_4 (a,b) and overbank inundation (flow scenario C_2) at S_1, S_2, S_3, S_4 (c,d,e,f). Dates are formatted as day/month/year. S_2 does not show does observed flow dynamics due the absence of nearby observation sites. S_3 does not show observed flow directions due to a missing sensor. Flows to the north are generally directed into the floodplain while flows to the south are toward the main channel. Note, due to thinning of

the data, each vector represents a 2-hour interval. Southward directed flows are toward the river, northward flows are to the floodplain interior. V_1: higher sub-bankfull validation scenario; C_2: higher overbank calibration scenario.

In summary, localized river-floodplain coupling by sub-bankfull inundation processes gives rise to temporally and spatially complex flow patterns associated with the submergence-emergence of local topography. For example, near-bank flows produce current reversals that depend on threshold stage height that differs for wetting or draining. At both S_3 and S_4 initial inundation occurs from the floodplain interior but above a threshold stage, flows are directed from the river to the floodplain. On the falling limbs, flows generally rotate towards the river. At both the near-bank locations (Figure 3.3a and 3.3b) and in the floodplain interior (Figure 3.2c and 3.2d) flow gradients are generally proportional to stage. The relation between stage and the occurrence of flow reversals at the near-bank locations show strong correlation but in the floodplain interior the relationship between stage and flow reversals is undefined. Taken together, the results show that flow directions are not uniquely defined by stage.

3.4.1.2 OVERBANK INUNDATION

When the river-floodplain system are coupled by the overbank flow process, all sites experience inundation, although the stage hydrographs and inundation depths vary substantially (Figure 3.3c-3.3f). Overbank inundation for C_2 occurs as a rise in stage from 0.5 to 2.27 m amongst the most upstream and downstream locations, respectively (Figure 3.3c and 3.3f). The rising limb close to the river is 30% steeper than at locations in the floodplain interior (Figure 3.2e and 3.2f). Similarly, recession limbs are ~2.5 times steeper near the bank, as observed during sub-bankfull inundation.

At the most upstream location, S_1, overbank flow directions are consistently towards the northeast (Figure 3.3c), along the levee-induced topographic gradient (Figure 3.1b). Flow gradients are initially variable until about 14 November when the stage reaches 31.92 m. Thereafter, the gradients steadily increase and attain peak values (up to 2.0×10^{-4}) that correspond with the hydrograph peak of ~32.13 m on 17 November. The flow remains northeastward on the falling limb, until 20 November, but as the stage falls below ~31.83 m gradients decrease gradually to $< 0.21 \times 10^{-4}$, accompanied by a ~22° northerly rotation.

At S_2 the gradients are initially small ($\sim 0.14 \times 10^{-4}$) and directed towards the southeast (Figure 3.3d). Further along the rising stage gradients increase to 1.17×10^{-4} (16 November) and the vectors rotate gradually, >30°, towards the river. As the stage continues to increase, a short-lived rotation of >10° occurs on 17 November, at ~28.47 m, after which flow directions rotate back ~10°. Maximum gradient of 1.45×10^{-4} occurs on 18 November near the maximum stage (28.76 m). Recession starts on 18 November, with a slight counterclockwise rotation (~16°) until the stage falls below ~28.54 m, after which the vectors attain their original directions on 20 November with a gradient of $\sim 1.16 \times 10^{-4}$. Thereafter, no change in flow directions occur until 21 November, and as the stage obtains values below 28.36 m flow vectors gradually rotate eastward. For stages below 28.33 m, the magnitudes decrease abruptly, but remain primarily eastward.

As with S_2, flow directions at S_3 are primarily towards the southeast (Figure 3.3e), nearly perpendicular to the main channel (Figure 3.1b). On 16 November, as stage increases from 25.77 to 26.59 m, the steeper rising limb produces flow towards the south with occasional rotations to the southwest, with gradients reaching 0.90×10^{-4}. After 16

November, for stages exceeding 26.59 m, the rising limb vectors gradually rotate ~10-30° resulting in southeasterly flows that persist for ~2.5 days (16.5 – 19 November). Magnitudes increase proportionally with stage and attain a maximum value of 2.1×10^{-4} on 18 November. On the falling limb, stage is accompanied by overlapping flow vectors that continue until 19 November when stage falls below ~27 m. Afterwards, the vectors attain their original directions while magnitude gradually decreases. On 20.5 November, for stages below ~26.69 m, flow directions gradually rotate ~100° counterclockwise, resulting in northeastward flows, and gradients decline to $<0.03 \times 10^{-4}$.

At S_4 (Figure 3.1b), a site without levees, flow is initially towards the southwest with a variable gradient reaching 0.38×10^{-4} (Figure 3.3f). A current reversal occurs on 15 November at ~25.03 m, near a break in the hydrograph, causing a rotation of 135°. A second break in the hydrograph on 16 November does not appear to influence flow direction. The gradient magnitudes are strongly correlated with stage, reaching 1.72×10^{-4} near the peak on 18 November. When on 22 November the stage falls below 25.76 m, the vectors slowly rotate counter-clockwise towards the northeast, and gradients remain strongly correlated with stage.

In summary, the overbank inundation process leads to varying flow directions along the riverbanks. At three locations, flow during the majority of the hydrograph is primarily directed from the river into the floodplain, while at one downstream location, the general movement of water is from the floodplain to the river, hence, this latter location is a site of floodplain drainage. As with sub-bankfull inundation, maximum gradients show strong correlation with stage. This is in general agreement with flows of the floodplain interior (Figure 3.2 and 3.2f).

3.4.2 RIVER-FLOODPLAIN COUPLING AND LARGE-SCALE CIRCULATION

3.4.2.1 SUB-BANKFULL INUNDATION

River-floodplain coupling starts ~2 hours after the wave crest passes the larger TBCs, therefore peaks in floodplain stage can be expected to lag river stage peaks. Flow vectors and inundation patterns indicate no substantive hydrodynamic response until the wave crest reaches rkm 10 (Figure 3.4a). However, with the passing of the crest the TBCs near rkm 6 become the initial source of flood water. Flow directions are variable but mostly toward the floodplain interior. Flooding is also observed at locations where the levee is not well-developed, specifically at ~rkm 5 to 8, near a set of point bars (Figure 3.1 and 3.4)

By the time the crest reaches rkm 20, it passed eleven more TBCs, of which seven show inundation due to their low bed elevations. Corresponding flow vectors are directed into the floodplain and primarily aligned with the orientation of TBCs (Figure 3.4b), and again coupling initiates near bends. Meanwhile, TBCs upstream of rkm 10 continue to route river water into the floodplain, increasing the extent and depth of inundation. The general flow pattern transitions from nearly perpendicular to the river to more northwesterly - northeasterly, towards lower elevations (Figure 3.1b), with flow velocities limited to a maximum of 0.05 m/s and a mean of 0.03±0.02 m/s (Figure 3.4b); the higher values are near the river-floodplain interface. These observations indicate that local storage dictates the initial flow gradients and velocity.

When the river crest reaches rkm 30 the flow and inundation fields demonstrate the ability of TBCs and connected networks to route river water across the entire floodplain. These conditions create floodplain wide hydraulic connections with the edge effects apparent as large shifts in both flow magnitude and direction; meanwhile higher velocities are aligned with the larger TBCs (Figure 3.4c). Moreover, the orientations of flow directions differ amongst channel networks. For example, when the flood crest is upstream of rkm 10 the flows are towards the north-northeast, but with the crest at rkm 10 to 20 flows are primarily northward, becoming northeastward when the flood crest is between rkm 20 and rkm 30 (Figure 3.4c). In the floodplain interior, when the flood crest is at rkm 30 flows are aligned with the floodplain channel network, indicating that TBCs and their connected networks dictate flow directions. Meanwhile, Cedar Creek becomes active and routes water to the northwestern edge of CNP, changing local flow patterns from northwest to southeastward. With this latter phase of the flood, maximum flow velocities do not necessarily occur within the channels. Both channelized and non-channelized flow speeds reach 0.12 m/s, with mean 0.08 ± 0.06 m/s.

With the crest at rkm 40 (Figure 3.4d) the inundation extent increases laterally, and the TBCs between rkm 30 and 40 disperse water into the floodplain. Flow velocities in TBCs upstream of rkm 30 decrease. In the region between rkm 35-38, no well-defined TBCs are identified, however, river water enters the floodplain through local, poorly developed levees and bank breaches. At some locations (rkm: 8, 9, 14-15, 21-23, 28-29, 31-32 and 35-36) flow vectors are directed from the floodplain toward the river, indicating floodplain drainage near point bars, TBCs and breaches (Figure 3.1 and 3.4d). Moreover, TBCs located within 0.5 km of the channel show both floodplain inundation and drainage patterns. For example, TBCs at rkm 31.7 and 31.8 show floodplain drainage, while the TBC at rkm 32 shows water transport into the floodplain. Besides changes in inundation extent, there appears to be a general, large scale, transport of water towards the southeast. Near the main channels, flows are aligned with local topography, but deeper into the

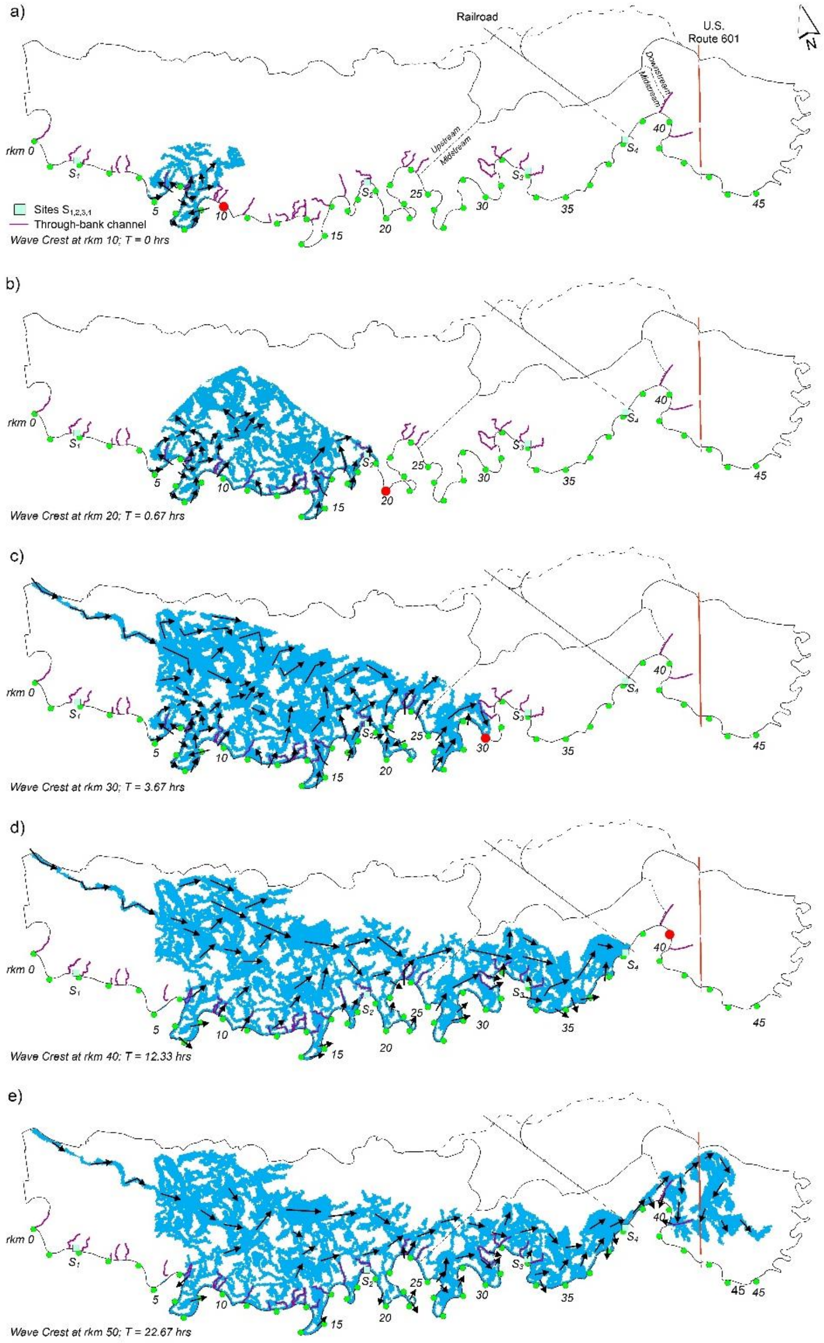

Figure 3.4: Inundation extent (blue, depths > 0.05 m) and flow vectors (arrows) during sub-bankfull inundation. The flow vectors were hand-selected and aggregated from model output as automatic aggregation to a larger scale grid was inadequate to visualize sub-bankfull flow directions. The solid black line depicts the boundary of CNP. The dashed black line indicates the extent of a terrace that borders CNP. The two solid lines divide the floodplain into three reaches: upstream, midstream, and downstream. The red dot indicates the location of the wave crest. For f) wave crest has exited the study region and is located at rkm 50, ~4 km downstream of the confluence. Inundation not indicated with a flow

vector, occur at velocities < 0.01 m/s. The straight-line inundation fronts observed in c) and d) result from limiting the visualized inundation to depths equal or greater than 0.05 m.

floodplain there is an overall southeasterly flow. Hence, the TBCs distribute water from the main channel towards the floodplain interior, where water is transported downvalley. The maximum flow velocities occur in the interior and is 0.13 m/s, while the maximum velocity in TBCs near the river is 0.04 m/s; the overall mean is 0.09 ± 0.03 m/s.

With the wave crest at rkm 50, ~ 4 km downstream of the Congaree-Wateree confluence (Figure 3.1), the region downstream of the railroad and the highway experience inundation (Figure 3.4e). Between them, inundation occurs mainly near the riverbanks, while downstream of Highway 601 (Figure 3.1) flooding is observed in the interior and occurs via a TBC consisting of an oxbow (rkm 39.6). In the upstream reach, well-defined water transport through TBCs weakens substantially (e.g., velocities < 0.03 m/s), but patterns of water transport away from the river can still be observed. Similarly, the southeastward flow observed when the wave crest was at rkm 40 weakens, but the overall flow pattern in the interior remains approximately east and southeastward. Near the riverbanks, flow vectors are locally directed towards the river. The maximum flow velocity occurs in the floodplain interior and is 0.08 m/s; while the maximum velocity in TBCs near the river are 0.03 m/s; the overall mean velocity is 0.05 ± 0.03 m/s.

In summary, system wide sub-bankfull inundation results in local velocities that are highly variable. Flow patterns vary but depend on TBCs and their passage by the wave crest in the main channel. Initially, river water is transported into the floodplain interior along creek networks. As inundation progresses, flow patterns become southeastward near the northern inundation front. Also, TBCs transport water inland, where it is then routed southeastward. Apart from local drainage near the riverbanks, no clear drainage patterns are observed. Hence, the more distant accommodation space remained largely unfilled. The circulation vectors at or near $S_{1,2,3,4}$ are generally in agreement with the flow dynamics of near-bank locations (Figure 3.3a and 3.3b). Sites S_3 and S_4 do not show a hydrodynamic response until the wave crest arrives at rkm 40 (Figure 3.4d), when the general flow pattern at site S_3 is northward, but the flow at Site S_4 is northeastward. These directions are in agreement with the primary flow directions observed at the hydrograph scale at sites S_3 (Figure 3.4a) and S_4 (Figure 3.3b), and appear related to higher stages in the floodplain (peaks of local hydrographs). When the wave crest is at rkm 50 (Figure 3.4e), the general flow direction at S_4 and S_5 is northeastward. Site S_4 indicates local floodplain drainage towards the south. These larger-scale flow directions appear to be linked with stage recession when compared to local flow dynamics (Figure 3.3a and 3.3b). Overall, heterogeneity in river-floodplain coupling-decoupling dynamics control the local and inland patterns of circulation.

3.4.2.2 OVERBANK INUNDATION

Higher discharge events produce spatially variable overbank inundation at various locations along the park boundary that precedes the arrival of the river crest. For instance, with the crest at rkm -20, water enters the floodplain primarily via through-bank flow and via levee breaches (Figure 3.5a). In the upstream reach, TBCs transport water into the floodplain but the extent of inundation is limited. At the western park boundary, water enters the floodplain via TBCs upstream of the Gadsden gauge. Further along the river, the midstream reach experiences widespread inundation before the upstream, and TBCs transport water deep into the floodplain interior. At locations where river water reached the northern bluff several kilometers inland, the flows are deflected down valley. The mean flow velocity across the floodplain is 0.16 ± 0.12 m/s and a maximum velocity of 0.34 m/s occurs in the midstream. Overall, flow directions near the main channel are aligned with the TBCs while deeper in the floodplain interior, specifically in the midstream reach, the flow is generally oriented towards the northeast.

With the flood crest at rkm -10 the extent of inundation continues to increase, accompanied by local velocity increases (Figure 3.5b). In this case, water is transferred to the floodplain as overbank flow. Also, in the upstream reach, floodwaters enter the park across the western boundary as intra-floodplain flow. In other words, the water inundating the Park arrives from the upstream floodplain, not from the river, and flow directions are variable but generally downvalley. Where floodwaters reach the northern bluffs, the flow is deflected eastward. In the midstream reach, there is simultaneous through-bank and overbank flow. Also, the local terrace, which is ~1 m higher than the surrounding floodplain, forces flow around its perimeter. The downstream region experiences inundation from the midstream floodplain as water enters via conduits near the northern boundary at Highway 601, and levee breaches. Flow downstream of the highway, close to the river is generally directed north - northwestward, while flows near the northern park boundary are towards the south and southeast. Along the interface between the floodplain and the Wateree River, flows are north-northwestward, indicating that the Wateree River also inundates the area of interest. The maximum velocity occurs in the midstream at approximately the same location as when the flood wave crest was at rkm -20, and is 0.91 m/s, while the average is 0.16 ± 0.15 m/s.

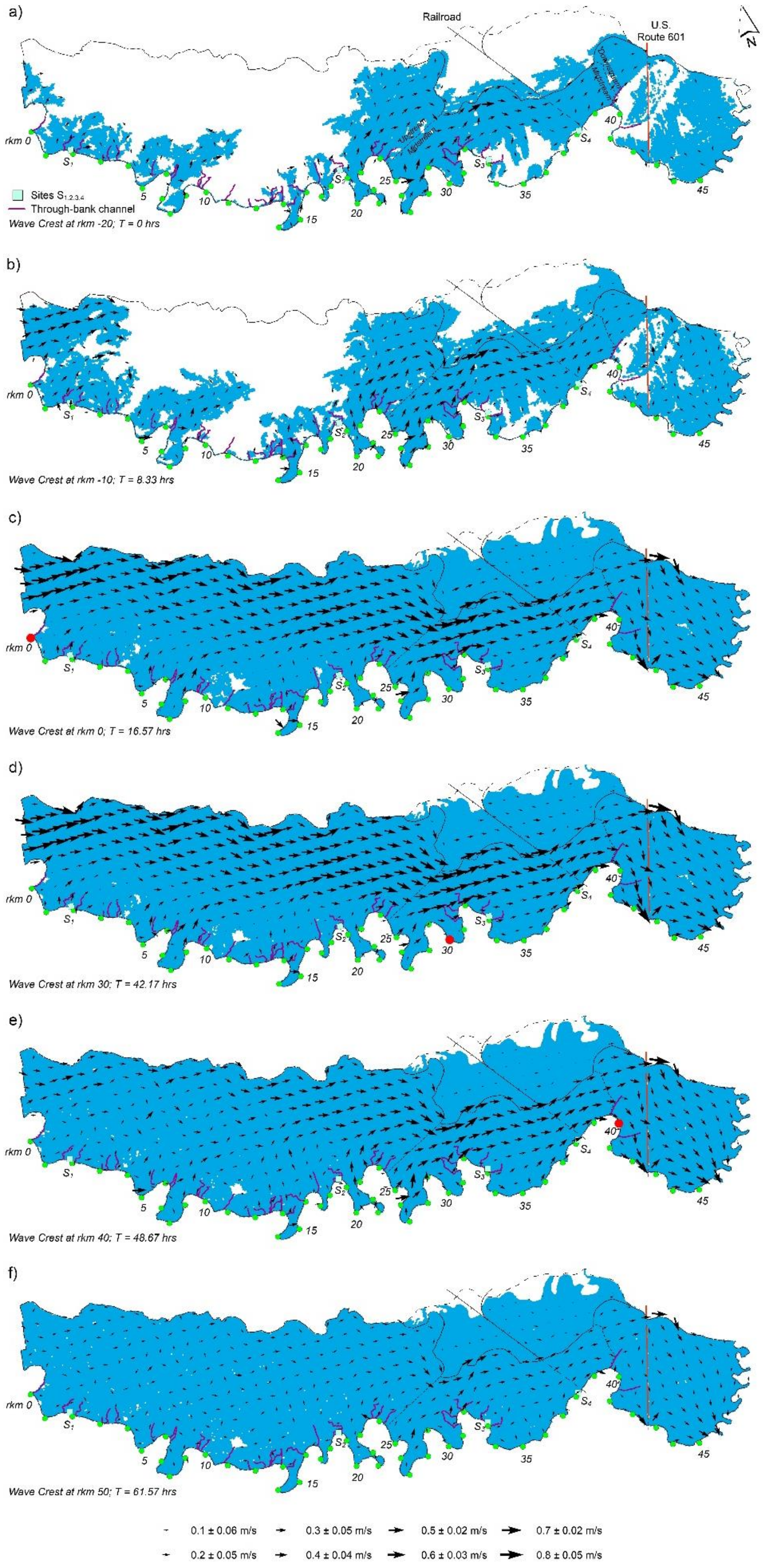
a)
Railroad
U.S.
Route 601
N
Downstream
Midstream
Upstream
Midstream
rkm 0
S1
S2
S3
S4
5
10
15
20
25
30
35
40
45
Sites S1,2,3,4
Through-bank channel
Wave Crest at rkm -20; T = 0 hrs
b)
Wave Crest at rkm -10; T = 8.33 hrs
c)
Wave Crest at rkm 0; T = 16.57 hrs
d)
Wave Crest at rkm 30; T = 42.17 hrs
e)
Wave Crest at rkm 40; T = 48.67 hrs
f)
Wave Crest at rkm 50; T = 61.57 hrs
0.1 ± 0.06 m/s
0.3 ± 0.05 m/s
0.5 ± 0.02 m/s
0.7 ± 0.02 m/s
0.2 ± 0.05 m/s
0.4 ± 0.04 m/s
0.6 ± 0.03 m/s
0.8 ± 0.05 m/s

Figure 3.5: Inundation extent (blue, depths > 0.05 m) and flow vectors (arrows, ≥ 0.01 m/s) during overbank inundation. The flow vectors show average flow directions aggregated over an ~400 m grid. The solid black line depicts the boundary of CNP. The dashed black line indicates the extent of a terrace that borders CNP. The two solid lines divide the floodplain into three reaches: upstream, midstream, and downstream. The red dot indicates the location of the wave crest. For (a) wave crest is located 20 km upstream of Gadsden (rkm 0), for (b) wave crest is located 10 km upstream of Gadsden (rkm 0), and for (f) wave crest has exited the study region and is located at rkm 50, ~4 km downstream of the confluence. Inundation extent and flow vectors for wave crest locations rkm 10 and 20 are not shown as flow circulation patterns remain relatively stable as the flood wave propagates through the main river from rkm 0 to 30.

By the time the wave crest arrives at rkm 0 the floodplain is fully inundated, except for a few small patches (Figure 3.5c). 52% of the total flow volume enters the CNP floodplain via the western park boundary and is transported downstream along the northern bluff. In the upstream region, water originating from the main channel is conveyed to the floodplain interior via high velocity regions near TBCs (rkm ~ 0-23). Between these high velocity water streams are relatively stagnant flow zones (rkm 3, 10 and 18) with average velocities of <0.05 m/s and this water is directed towards higher velocity streams. In the midstream reach, floodplain flows are primarily eastward; flows are not aligned with TBCs but occur approximately perpendicular to the TBCs near rkm 32. As floodwaters are transported further downstream, flows at the railroad pillar-embankment are deflected to the southeast (not visible at scale of figure). Downstream of the railroad, flows are northeastward, aligned with the northern boundary and the riverbanks to the south. Further downstream, near Highway 601, part of the flow is deflected southward by a large oxbow (Figure 3.1b; *Xu et al., 2021*) and water exits the floodplain. Additionally, floodwater passes through this area where the bridge is supported by pillars. Most of the flow that reaches the region downstream of HW601 gradually rotates towards the south-southeast and exits the floodplain at the Congaree and Wateree confluence.

It is noteworthy that during inundation, with the river crest between 0-30 rkm the TBCs continue to function as efficient pathways that preferentially convey water from the main river toward the northern boundary (Figure 3.5c and 3.5d), while the general circulation patterns remain relatively stable and to the southeast. For example, with the river crest between 0-30 rkm, variations in average flow directions are limited to 12° but the velocity decreases by a factor of ~2. On the other hand, flow paths adjust substantially with the wave crest at rkm 40 (Figure 3.5e). For instance, the northeastward directed flow becomes less pronounced and weakened. TBC flows continue to reach the deeper floodplain interior. However, flows in the most upstream TBCs become erratic, with poorly defined flow paths. In the midstream and downstream reaches, flow patterns remain similar to when the wave crest was at rkm 30, although an increase in current can be observed at rkm 23. Flow velocities over the terrace are relatively low (< 0.04 m/s).

At rkm 50, ~4 km downstream of confluence, flow velocities across the floodplain weaken (Figure 3.5f). In the upstream, the southeastward water transport along the northern park boundary is not visible. Flow velocities decrease, and directions become erratic while the floodplain is still fully inundated, and regions of high velocity surrounding TBCs have dissipated. TBCs in the midstream reach, downstream of ~rkm 23, continue to transport river water towards the deeper floodplain interior, but at reduced velocities. Water that is transported towards the northern boundary via TBCs is conveyed eastward where it exits the floodplain near the highway, or downstream into the Congaree and Wateree rivers.

In summary, 52% of flood water on the study site is from the upstream floodplain, not from the local river reach. River water contributions to inundation are preferentially routed through TBC-networks, and as overbank flow. Water near the riverbanks is nearly stagnant, providing flood storage that is gradually routed to TBCs. In the midstream, at higher elevations, flow is aligned with TBCs while in the lower elevations flow is perpendicular to the TBCs for varying inundation conditions. Further downstream water eventually exits the floodplain between Highway 601 and the Wateree River. The large-scale flow vectors and small-scale flow dynamics at near-bank locations demonstrate these similarities and differences. S_1 shows overbank flow directions consistently towards the northeast and is in accordance with the system scale vectors. S_2 experiences predominantly southeastern flows, however, system scale flow vectors indicate eastward flows. While local and large-scale flow vectors are in disagreement at S_2 flow vectors at S_3 show consistent southeastward patterns. A rotation of flow towards the northeast is consistent with the flow reversals observed at the local scale. At the most downstream location, S_4, large scale flow vectors are consistent with local flow dynamics. Overall, higher discharge events produce a different type of river-coupling and corresponding spatial variability in flow complexity.

3.5 DISCUSSION

Floodplain flows and currents in the interior (Figure 3.2) and near the banks (Figure 3.3) can be simple or highly complex for different river stages, and topographic frameworks. Moreover, the complexity in floodplain flow is largely controlled by temporal and spatial dynamics in river-floodplain coupling-decoupling effects on inundation processes. For sub-bankfull wetting, inundation occurs primarily through large TBCs after the river wave has passed. As the channel wave crest propagates, an increasing number of TBCs become active and this enhances the routing of river water into the floodplain. The result is inundation patterns that are controlled by the orientation of floodplain channels.

As inundation progresses and flow patterns evolve, a general southeastward flow develops near the center of the floodplain, where the floodplain channel network is not well developed or where the floodplain elevation is lower (Figure 3.4d).

At intermediate spatial scale (~100m) and temporal resolution (15 min) sub-bankfull flows are complex. Floodplain inundation occurs after the wave crest passes major TBCs (Figure 3.4). Flow reversals are frequent with flow orientation alternating away from and towards major TBCs (Figure 3.3a) or levee breaches (Figure 3.3b). These flows appear to be threshold dependent, with the threshold set by the elevation at which flows in the floodplain network merge and then submerge local topography. For example, site S_3 is flooded from the northeast for stages below the threshold, while for higher stages inundation occurs directly from the TBC mouth. Similar patterns are observed on the falling limb (i.e., drainage). Further, flow reversals near the banks appear to be correlated with thresholds in stage, while in the floodplain interior there does not appear to be a similar relationship (Figure 3.2c). Hence, for a single stage at the floodplain sites multiple flow directions were detected at the same location. These observations indicate that near the river, flow dynamics are more directly controlled by stage variations in the main channel, while in the floodplain interior the local channel network and storage effects influence circulation. Thus, for a single stage in the main channel, floodplain flows show significant temporal variability.

Inundation during overbank flows primarily starts at the midstream reach, while in the upstream, inundation is limited to TBCs because the levees are well-developed. Hence, a single discharge can give rise to three simultaneous inundation conditions, through-bank flow, overbank flow, or no flow. Later, but prior to the arrival of the wave crest, inundation is augmented by flow across the western park boundary, e.g., intra-floodplain water (Figure 3.5a and 3.5b). The floodplain is fully inundated by the time the wave crest reaches the upstream edge of the study area, which is in stark contrast with the initiation of sub-bankfull inundation. Meanwhile, near the northern bluff boundary a high velocity southeastward flow develops, and along the channel some zones surrounding TBCs function as efficient pathways to transport water from the main river, inland. Also, between TBCs, low velocity zones develop and appear to store water prior to reaching the nearest TBC.

At a smaller spatial scale (~100 m) and higher temporal resolution (30 min), the overall flow pattern for overbank inundation appears less complex, but flow directions differ along the banks. Flows are generally directed into the floodplain, but at one reach (rkm 18.8) flow is towards the main channel, coming from a “stagnant” zone. Maximum velocities have higher correlation with stage. System-wide, the flow vectors during overbank inundation reveal higher velocity streams near the larger TBCs. However, this is not the case where flow towards the river was observed. Overall, preferential pathways, stagnant zones, intra-floodplain transfers of water, current reversals and flows that result from heterogenous levee development create highly complex flows and connections amongst flows throughout the floodplain. Therefore, these properties combined with thee spatial and temporal variations in floodplain storage give rise to the condition that a single river stage does not uniquely define characteristic floodplain flow patterns.

Overall, floodplain flow systems can have a range of complex inundation and drainage pathways. Exactly how the temporally and spatially complex flow conditions translate to quantifying hydraulic connectivity in floodplains and wetlands remains poorly defined. Understanding the dynamics of hydraulic connectivity, taken as the degree of surface water exchange between river-floodplain systems, (*Amoros & Bornette*, 2002; *Passalacqua*, 2017; *Wohl et al*., 2019), typically relies on numerical models that allow for estimates of flux at the river-floodplain interface (e.g., *Tull* et al., 2022; *Bryne et al*. 2020; *Czuba et al*., 2019), or the temporal and spatial variability in hydraulic river-floodplain coupling-decoupling. On the other hand, at times a substantial portion of floodwater, can be expected to enter the area of interest from the floodplain upstream of the study area (e.g., Figure 3.5). Thus, meaningful assessments of hydraulic connectivity must account for upstream floodplain sources of water that are beyond the immediate area or river reach of interest.

This study highlights complex flows in response to floodplain wetting and draining by real flood waves. Our work underscores the need for flow models that are forced to be as-realistically-as-possible to gain insight on floodplain circulation processes. For example, numerical evaluation of river-floodplain hydraulic connectivity has been investigated with unrealistic steady or quasi-steady forcing conditions (e.g., *Tull et al., 2022; Pinel et al., 2020; Czuba et al., 2019*) and although the results were insightful they are not easily generalized. Here, we demonstrate the dynamic nature of hydraulic connectivity with realistic scenarios and the non-unique flow response for a given stage that must be addressed to make it a meaningful system wide metric. This is especially relevant to floodplains that function are sinks for carbon (e.g., *D'Elia et al., 2017; Lininger et al., 2019; Sutfin et al., 2016*), and nutrients and sediments (e.g., *Funk et al., 2020; Fischer et al., 2019; Osterkamp & Hupp, 2010)*. Furthermore, understanding the dynamics of floodplain coupling-decoupling aids flood hazard and prediction and mitigation analyses through, for example, floodplain wave attenuation. Additionally, accurate modeling can provide robust background information on computations of river and floodplain water parameters to validate remote sensing applications, such as the Surface Water Ocean Topography mission (e.g., *Pavelsky et al. 2014*).

3.6 CONCLUSIONS

Hydrodynamic simulations of floodplain flow were conducted for two discharge events; one that led to partial floodplain inundation, and one for full inundation. Detailed analyses of flow within a smaller 93 km^2 part of a 247 km^2 computational domain were used to characterize flow patterns over the low-gradient, but topographically complex area of Congaree National Park. Quantitative analyses of model performance indicate that simulation results are representative of actual field conditions. Moreover, we found that numerically replicating these complex flows requires the application of realistic or unsteady boundary conditions with computational grids including detailed bathymetry of the main river.

Flow vector analyses show that flows can be predictably simple or complex, largely controlled by inundation process. In particular, during high, but below bankfull conditions river-floodplain coupling is limited to levee and bank breaches, or via through-bank channels, becoming more fully developed after the passing of river flood wave crest. The corresponding floodplain flow patterns are highly variable, including current reversals, and the variability appears to be dependent on thresholds in stage.. Flow reversals at locations near the river show strong correlations with stage, but less so in the floodplain interior. For overbank stage conditions, expansive inundation precedes the arrival of the river wave crest due to inundation by flows from the upstream floodplain, accounting for nearly 52% of the total flow volume. Also, inundated through-bank channels operate as efficient, high velocity pathways that directly connect the river to the interior.

DATA AVAILABILITY STATEMENT

The lidar dataset is available from NOAA Digital Coast website at https://chs.coast.noaa.gov/htdata/lidar1_z/geoid18/data/4815. The river stage and discharge records at the USGS stations are available at https://waterdata.usgs.gov/monitoring-location/02169500 (Congaree River at Columbia, South Carolina), https://waterdata.usgs.gov/monitoring-location/02169625 (Congaree River at Congaree National Park near Gadsden, South Carolina), https://waterdata.usgs.gov/monitoring-location/02169750 (Congaree River at United States Highway 601 near Fort Motte, South Carolina), https://waterdata.usgs.gov/monitoring-location/02169810 (Santee River at Trezesvants Landing near Fort Motte, South Carolina), and https://waterdata.usgs.gov/monitoring-location/02148000 (Wateree River near Camden, South Carolina). The Delft3D Flexible Mesh Suite can be obtained via Deltares (https://www.deltares.nl/en). Field data and model output can be accessed through the HydroShare repository associated with this manuscript (https://doi.org/10.4211/hs.859b3b546ec749a09b15b52f2163c5f5).

CHAPTER 4

HYDROGRAPH AND INITIAL WETTING EFFECTS ON FLOODPLAIN SURFACE-WATER STORAGE[3]

Floodplain hysteresis in the river stage and floodplain storage relationship has been investigated using a robustly calibrated and validated hydrodynamic capable of reproducing flow patterns over a topographically complex floodplain that includes a heterogeneous main channel levee. Synthetic hydrographs were used to reduce the complexity in the analyses of floodplain inundation dynamis and model output, and to help characterize governing flow processes. Four hundred observed sub-bankfull and overbank waves from a long-term data set were analyzed to obtain estimates of rising and falling gradients, stage variations, and wave periods and were used to guide the development of synthetic hydrographs. Findings indicate that shallow rising gradients produce enhanced floodplain inundation and result in lower river water levels for both sub-bankfull and overbank inundation. Steeper rising gradients deter inundation processes and cause higher water levels in the river. River-floodplain exchange for shallow rising stages is initiated at lower river stages than for the same stage during a steep rise. Similarly, shallow falling stages enhance overall floodplain drainage processes for sub-bankfull and overbank inundation. Steep falling stages, however, result in greater floodplain water retention. The substantial variation in inundation and drainage processes results from highly variable and

---

[3] van der Steeg, S., Torres, R., Viparelli, E., Xu, H., Elias, E., & Sullivan, J. Hydrograph and initial wetting effects on floodplain surface-water storage. To be submitted to *Water Resources Research*.

complex flow patterns resulting from various rates of change of stage that appear to be dependent on flow thresholds associated with submergence and emergence of topography. A single stage in the main does not uniquely define floodplain hydraulics, rate of change of stage is a controlling factor. Given these findings, we propose that assessment of floodplain hydraulic connectivity accounts for the effects of rates of change of stage as determining factor controlling river-floodplain surface-water connectivity.

4.1 INTRODUCTION

Floodplains are spatially complex landscapes with a variety of low relief surface features and landforms (e.g., *Xu et al., 2020*; *Park*, 2020; *Lewin and Ashworth*, 2014). The locally variable floodplain features are visible in satellite imagery for large river floodplains (e.g., *Mertes et al*., 1996; *Rowland et al*., 2009; *Lewin & Ashworth*, 2014), and in high-resolution lidar data for smaller systems (e.g., *Xu et al.*, 2020; *David et al.*, 2017; *Lindroth et al.*, 2020). These data reveal that floodplains contain extensive networks of well-defined channels and topographically connected depressions, (e.g., *Xu et al*., 2020; *David et al*., 2017; *Fagan & Nanson*, 2004), and in some cases, the channels originate as cuts across levees or banks of the main river, referred to as through-bank channels (*Xu et al*., 2021; *Day et al., 2008*; *Lewin and Hughes, 1980*). Corresponding complex patterns of inundation and flow have been detected through remote sensing (*Alsdorf et al., 2007a; Alsdorf et al., 2007b; Mertes, 1997*), in field observations (*van der Steeg et al., 2021; Girard et al., 2009; Filgueira-Rivera et al., 2007)*, and in numerical simulations of floodplain circulation (e.g., *Van der Steeg et al., 2022; Tull et al., 2022; Pinel et al., 2020*). Therefore, floodplain topography exerts a considerable influence on surface inundation and flows (e.g., *Xu et al., 2021; van der Steeg et al., 2021; Lindroth et al., 2020*).

Complex flows are also influenced by a variable floodplain surface gradient, and the temporal and spatial variability of tributary or main channel exchanges (*Mertes, 1997; Van der Steeg et al., 2022; Tull et al., 2022*). For example, along-channel variability in river-floodplain coupling-decoupling associated with heterogeneous levee development will give rise to the simultaneous occurrence of through-bank (i.e., sub-bankfull) and overbank inundation (*Xu et al., 2021; Lewin and Huges, 1978; van der Steeg et al., 2022*) along different reaches of the river. Furthermore, the submergence-emergence of vegetation (e.g., *Baptiste et al., 2004); Box et al., 2021; Mertes et al., 1995*), and spatial and temporal variability in short-lived tributary inflows (e.g., *Alsdorf et al., 2000; Mertes, 1997, van der Steeg et al., 2022*) enhance flow complexity.

Lewin and Hughes (1980) were the first to propose that floodplain flow processes can be summarized in the context of river stage and floodplain storage. For instance, complex flows associated with floodplain wetting and drying may lead to a type of hysteresis, a non-unique relationship between river stage and inundated area (e.g., *Makungu and Hughes, 2021; Zhang and Werner, 2015; Lewin and Hughes, 1980*), or water storage (Figure 4.1a) (e.g., *Lewin and Hughes, 1980; Makungu and Hughes, 2021; Zhang et al., 2017*). *Lewin and Hughes (1980)* proposed that an envelope of stage-area (storage) is defined by equilibrium wetting curve and drainage curves (Figure 4.1a). Typically, a wetting floodplain stage-storage condition will tract, in a counter-clockwise fashion, will track or parallel to the main wetting curve. When wetting is interrupted by a decreasing water supply, drainage occurs, and the system stage-storage conditions will shift toward the main draining curves. The opposite occurs when a draining system is suddenly rewetted. Hence, there is a multitude of pathways between the main wetting-draining

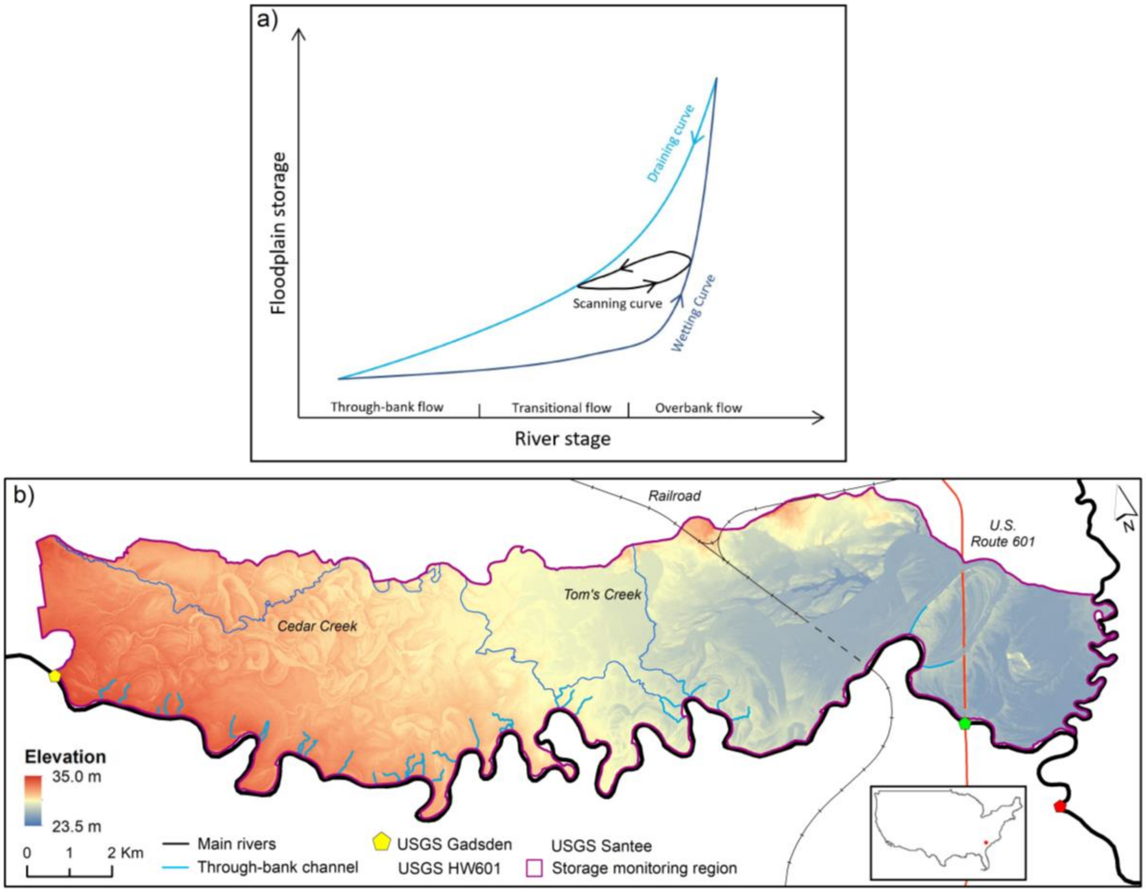

Figure 4.1: (a) Conceptual diagram of the stage-storage relationship showing hysteresis (i.e., a non-unique relationship between river stage and floodplain water storage). The hysteresis curve consists of a wetting curve and a draining curve. The wetting curve depicts the increasing floodplain storage as river stage rises, while the draining curve the reduction of floodplain storage as a function of the decreasing river stage. River stage is divided into three sections that range from the occurrence of through-bank flow, transitional flow (through-bank and overbank flow), and overbank flow. Between the wetting and drainage curves there are an infinite number of curves in between depending on the flow conditions. (b) DEM of Congaree National Park. Locations of sub-bankfull river-floodplain exchange are depicted with light blue lines. The storage monitoring region is indicated in pink. Cedar Creek and Tom's Creek are two major tributary channels.

curves that define the system. These curves are referred to as scanning curves, and together these curves define hysteresis. Therefore, for a particular river flood stage there exist different amounts of unfilled storage (Figure 4.1a). Overall, river stage, flow path characteristics and accommodation space have non-unique relationships with respect to river stage, collectively leading to hysteresis in floodplain systems (e.g., *Makungu and*

Hughes, 2021; Lewin and Hughes, 1980; Zhang et al., 2017). Hence, we propose that hysteresis may serve as a metric for evaluating the temporal and spatial variability of floodplain flows.

Another factor influencing hysteresis is hydrograph slope on the rising or falling limbs (*Lewin and Hughes, 1980; van der Steeg et al., 2021; Fleischmann et al., 2016*). For example, a steep rising limb may result in reduced floodplain inflow compared to a slow rise (Figure 4.1a) (*Lewin and Hughes, 1980; Hughes, 1980*) whereas a rapidly falling stage may lead to a greater water retention on the floodplain, for a given river stage. Conversely, low rates of rise and fall allow the overall water storage to keep pace with changing stage. The foregoing implies that gradually rising hydrographs will allow for a larger area to be inundated, and a rapid rise less so. Therefore, the rate of change of stage can produce variable inundation area or storage for a given stage. The net result is that hydrograph rate of change can cause the floodplain stage and river stage to be out of phase, and lags in the internal floodplain water transfer processes may lead to hysteresis. Although floodplain hysteresis has been documented (e.g., *Makungu and Hughes, 2021; Rudorff et al., 2014; Wolfs and Willems, 2014*), the controls of hysteresis are not well constrained due to the limited number of studies. For example, recent reports that were aimed at detecting floodplain hysteresis rely on hydrodynamic model results (*Makungu and Hughes, 2021; Zhang et al., 2017; Zhang and Werner, 2015*) to evaluate fluxes along the river-floodplain interface (e.g., *Makungu and Hughes, 2021; Byrne et al., 2019*), but the study provided limited insight on processes and process dynamics.

Understanding the effects of hydraulic rates of change for floodplain inundation dynamics can help provide a more physically based, and system wide understanding of flow complexity over inundated floodplains, and it can enhance efforts to quantify hydraulic connectivity. Furthermore, a better understanding of the interplay between the rate of change of stage and hysteresis effects will provide insight on the ability of floodplains to attenuate passing flood waves (e.g., *Lewin and Hughes, 1980; Hughes, 1980; Castellarin et al., 2011*), an important element of dam management. Therefore, we propose that detailed insight on water circulation over inundated areas and the processes that facilitate inundation and drainage can aid in, for example, flood hazard and mitigation analyses and ecosystem sustainability.

The purpose of this study is to assess the effects of channel hydrograph rate of change of stage on the dynamics of floodplain inundation. Motivation for this work is partly driven by a dearth of information on the variability in a floodplains ability to absorb and attenuate flood waves under realistic forcing conditions. We hypothesize that flood waves with steeper rising stages result in reduced floodplain storage and attenuation (i.e., less flux into the floodplain), and that steeper falling stages result in greater floodplain water retention. A Delft3D Flexible Mesh numerical flow model that has been calibrated and validated by multiple sets of observations is used to quantify flow dynamics under realistic and synthetic hydrograph forcing conditions. Model output under quasi-real time forcing conditions provides synoptical, near-realistic views of flow dynamics, while simplified forcing conditions allow for the identification of governing flow processes.

4.2 STUDY REGION

This study site is a river-floodplain system located in the southeastern North American coastal plain, the Congaree River, SC, USA, in the Congaree National Park (CNP) (Figure 4.1b). The floodplain is ~19 km long, and up to 5.9 km wide with a total area of ~93 km^2 (Figure 4.1b). Two small, upland tributary channels discharge water to CNP (Figure 4.1b; *Xu et al*., 2021), but floodplain inundation is primarily from the main river (Kinzer, 2017; *Doyle, 2009*). Within the park, the floodplain elevation decreases from 35 to 23.5 m (Figure 4.1b), resulting in an average valley gradient of ~4×10^{-4} m/m to the northeast (*Xu et al., 2020*) and the reach-averaged riverbed gradient is 1.5×10^{-4} m/m. Bank and levee height are highly variable, thereby facilitating irregular along-channel inundation patterns (*Xu et al., 2021*). In particular, for a given discharge the levees in the upstream reach require a higher river stage for overbank inundation and therefore favor through-bank inundation, while in the downstream reach, the levees are poorly developed, and overbank inundation occurs (*Xu et al., 2020, 2021*). See *Xu et al. (2020, 2021)* and *van der Steeg et al. (2021, 2022)* additional study site details.

Therefore, flood waters may enter the floodplain during high, but below bankfull river stages (*Xu et al., 2021; van der Steeg et al., 2021; Kupfer et al., 2015*) via through-bank channels. There are 32 well-developed through-bank channels, having mouth widths ranging from 7 to 30 m (*Xu et al., 2020, 2021;* Figure 4.1b). Some channels extend up to several kilometers inland (*Xu et al., 2020*) and thereby connect the river with an expansive network of channels, conduits, and isolated depressions. These hydraulic openings and connected networks are important because they facilitate inundation and material exchange between the main river and the floodplain surface during below bankfull stages (*van der Steeg et al., 2021; Xu et al., 2021; Kupfer et al., 2015*), while during overbank inundation through-bank channels act as efficient pathways that produce high velocity zones several kilometers into the floodplain (*van der Steeg et al., 2022*).

The United States Geological Survey (USGS) Congaree River station in Columbia, SC (#02169500) discharge data from 1984 to 2021 ranges from 30 to 4200 m^3/s and water levels vary between 35 and 43 m. Water levels at the USGS Gadsden station (#02169625, Figure 4.1b) 38 km downstream, at the upstream park boundary, show that since 1984 the local stage (discharge not reported) varies by 8 m. Two additional gauging stations outside of the study area provide water levels for the Santee River (water level, USGS Santee River in Fort Motte, #02169810) and for the Wateree River (discharge, USGS Wateree River in Camden, #02148000, not shown in Figure 4.1b).

4.3 METHODS

To quantity flow dynamics in the river and adjacent floodplain, a validated model by *van der Steeg et al. (2022)* for the CNP and the surrounding floodplain is utilized. The Delft3D Flexible Mesh (Delft3D FM, *Deltares, 2022a*) model is operated in depth-averaged mode (i.e., 2D) to compute flow parameters resulting from unsteady discharge and water level forcing conditions obtained from nearby USGS observation stations. Model calibration and validation work focused on the accurate representation of 1) water level in the main channel 2) water level in the floodplain, 3) flow direction and 4) flow gradient over the floodplain. Simulated water levels were compared with observed water levels from six locations in the river, and 20 locations in the floodplain for varying river discharge conditions. Simulated flow direction and gradient in the floodplain were compared to observations (*van der Steeg et al., 2021*) for model validation. See *van der Steeg et al. (2022)* for more details.

One of the major assets of the quasi-realtime modeling approach is the ability, if constrained with suitable field observations, to provide near-realistic predictions of high spatial and temporal resolution that allow for hydrodynamic assessments across the flow domain. A major drawback, however, is that the identification of the governing flow processes can be complicated due to compound model output. Identification of the governing processes requires simplification, and to reduce the complexity in the analyses of floodplain circulation and model output, the boundary conditions in the model from *Van der Steeg et al. (2022)* are modified, and the model is forced with synthetic hydrographs. The use of synthetic hydrographs allows us to control properties such as discharge, the rate of change of the falling and rising limb, the duration, and initial conditions. The Congaree River boundary is forced using various discharge time series (Figure 4.2). The Wateree River, the Cedar Creek and Tom's Creek boundaries are not forced to reduce complexity in the analyses of simulation results. The downstream boundary condition at the Santee River consists of a discharge-stage relationship derived from simulations (*van der Steeg et al., 2022*) by assessing the synchronous discharge and water level at the boundary for a range of flow conditions. The boundary conditions allow for undisturbed propagation of flow out of the domain.

The characteristics of synthetic hydrographs (Figure 4.2) are constrained by observations through an analysis of the rising and falling limbs of discharge waves over the period from 2012-2022. Rising and falling limbs of individual discharge waves at the Congaree River gauge in Columbia, SC were analyzed for sub-bankfull and overbank flow conditions. The starting and end points of both the rising limbs and falling limbs were determined using an 8-hour moving gradient scanning-window starting at the start of rising limb and scans upward until the gradient becomes less than the threshold value of 0.005 (value defined empirically). After that, the window scans the falling limb until the gradients

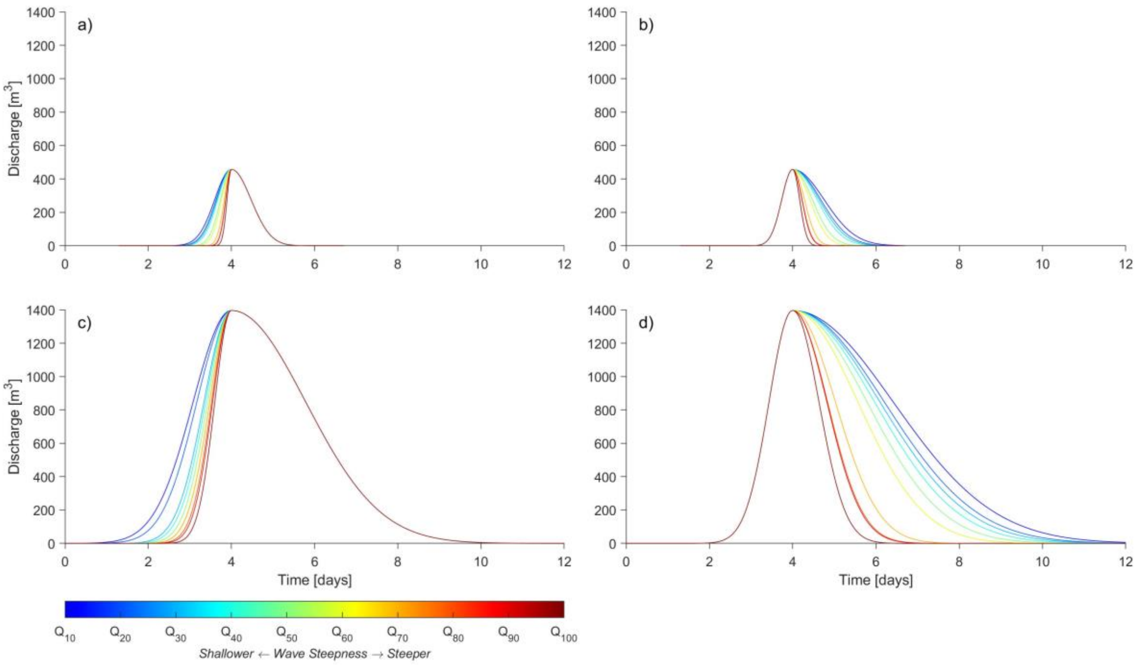

Figure 4.2: (a) Synthetic hydrographs for sub-bankfull inundation with variable rising limbs and constant falling limb. (b) Synthetic hydrographs for sub-bankfull inundation with a constant rising limb and variable falling limbs. (c) Synthetic hydrographs for overbank inundation with variable rising limbs and constant falling limb. (d) Synthetic hydrographs for overbank inundation with a constant rising limb and variable falling limbs. Constant rising limbs (b,d) and constant falling limb (a,c) correspond to the median wave gradient of the corresponding falling or rising limbs for the same wave type. Cold colors indicate shallower wave gradients, warmer colors indicate steeper wave gradients.

falls below the threshold value. An 8-hour window was required to account for possible compound wave effects. If waves are closely followed by one another and the calculated gradient does not reach the threshold value, the location of minimum gradient is determined to be the endpoint of the falling limb. Subsequently, a first order exponential function is fitted to the normalized rising and falling limbs, and the most optimum decay parameter is determined by minimizing the root-mean-square-error of the residuals. Based on the cumulative distribution function of the exponential decay parameters, rising and falling limb gradients were selected for the 10th, 20th, 30th, 40th, 50th,60th,70th, 80th, 90th and 100th gradient quantiles (Q_{10-100}) for both sub-bankfull waves (Figure 4.2a,b) and overbank waves (Figure 4.2c,d). The period of synthetic hydrographs was determined based on the median duration of observed waves. For sub-bankfull, the median wave period is 2.2 days while for overbank the period is 5.4 days. Similarly, the maximum discharge was defined by the median of the maximum discharge of waves observed in the record (sub-bankfull: 457 m^3/s; overbank: 1396 m^3/s). Note that wave duration is affected by the gradient of either the rising or falling limb; for example, steeper gradients result in shorter durations. Two sets of synthetic hydrographs were created: one with varying rising stages and a single falling limb (50th quantile) (Figure 4.2a,c), and one with a single rising (50th quantile) and varying falling stages (Figure 4.2b,d).

Analyses of model results indicate that the initial inundation state is crucial to determining accurate model products (*Van der Steeg et al., 2022*), and suggests that the presence of initial floodplain water affects inundation dynamics (e.g., *Tull et al., 2021*). Here, the effects on initial inundation are assessed by wetting the floodplain channel networks and depressions prior to the start of the simulations of the synthetic hydrographs, following the quasi-steady approach presented by *Xu et al. (2021)* to estimate inundated floodplain area. The floodplain depressions are filled with water varying from 0.1 up to 0.5 m in steps 0.1 m. Higher initial conditions result in greater surface water network connections in the floodplain (e.g., *Xu et al., 2021; van der Steeg et al., 2022*), and potentially enhance river water distribution into the floodplain. We specifically address this issue.

For the analyses performed, the CNP forms a water mass-balance monitoring area and time-dependent output of all water fluxes in and out, and the storage within the park is calculated by the Delft3D FM Water Quality module (*Deltares 2022b*). To analyze the effects of varying rate of changes and initial inundation conditions on floodplain hysteresis, the time-dependent storage output is linked to the stage at the most upstream edge of CNP, the USGS Gadsden gauge (Figure 4.1b). This allows the determination of the relationship between floodplain storage and the main river stage, and similar figures as presented in Figure 4.1a were constructed for CNP for each of the synthetic hydrographs. For clarity and brevity, we refer to the terminology presented in Figure 1a to explain the findings presented in Results.

For subsequent analyses, the total storage (i.e., integrated over the full simulation period) is normalized with the inflow discharge for each synthetic hydrograph, and the storage is expressed as a percentage of the inflow. Normalization is required to allow for relative storage comparisons amongst synthetic hydrographs as the volume of water forced into the model at the boundary varies depending on the rate of change of rising and falling stages. For simulations with these initial conditions, the storage computations do not account for water initially present in the floodplain. The computations only include newly added river water to allow for an inter-model comparison between dry and initially inundated floodplain.

Simulations are "spun-up" to a steady-state water level in the main channel corresponding to a discharge of 150 m^3/s prior to the synthetic hydrograph computations. The discharge corresponds to the minimum discharge for which accurate simulation results were obtained (*Van der Steeg et al., 2022*). At these flow conditions, no river-floodplain exchange occurs for both dry and initially wetted floodplain is dry. This 'spin-up' period, prior to the actual computations, is sufficient to dissipate the errors in hydrodynamics induced by the discrepancy between boundary conditions and the initial river state.

4.4 RESULTS

4.4.1 HYDROGRAPHS AND HYSTERESIS.

Sub-bankfull floodplain wetting is driven by a ~20 day long higher stage interval, about 3 m above background values; the hydrograph has over a dozen short-term peaks and the associated fluctuations range from 0.3 to 2.4 m (Figure 4.3a). The multiple peaks have no characteristic trends in time. The corresponding storage represents a subdued or damped version of stage, and the multiple fluctuations are not present. Total storage increases from ~3 x 10^7 m^3 to a maximum of ~9 x 10^7 m^3 before declining to ~5.5 x 10^7 m^3. The maximum change in storage amounts to a maximum area averaged inundation of ~0.6 m.

On the other hand, the overbank inundation is driven by an increase in stage that is 2.5 m higher than background, but with a peak elevation about 2 m higher than the sub-bankfull flow above (Figure 4.3b). It is noteworthy that the overbank flood has a ~6 day long quasi-steady stage interval, as expected for bankfull conditions. Likewise, the storage response is a subdued version of the hydrograph. However, the slope of the storage curve lags the rising limb, and the peak value is offset and asymmetrical relative to stage. Storage increases from about 0.6 x 10^8 m^3 to a maximum of 3.0 x 10^8 m^3. The difference in storage amounts to a floodplain averaged depth of ~2.6 m. The steep rising and falling limbs and the long duration quasi-steady maximum interval are expected to provide a clearer representation of hysteresis relative to the sub-bankfull case.

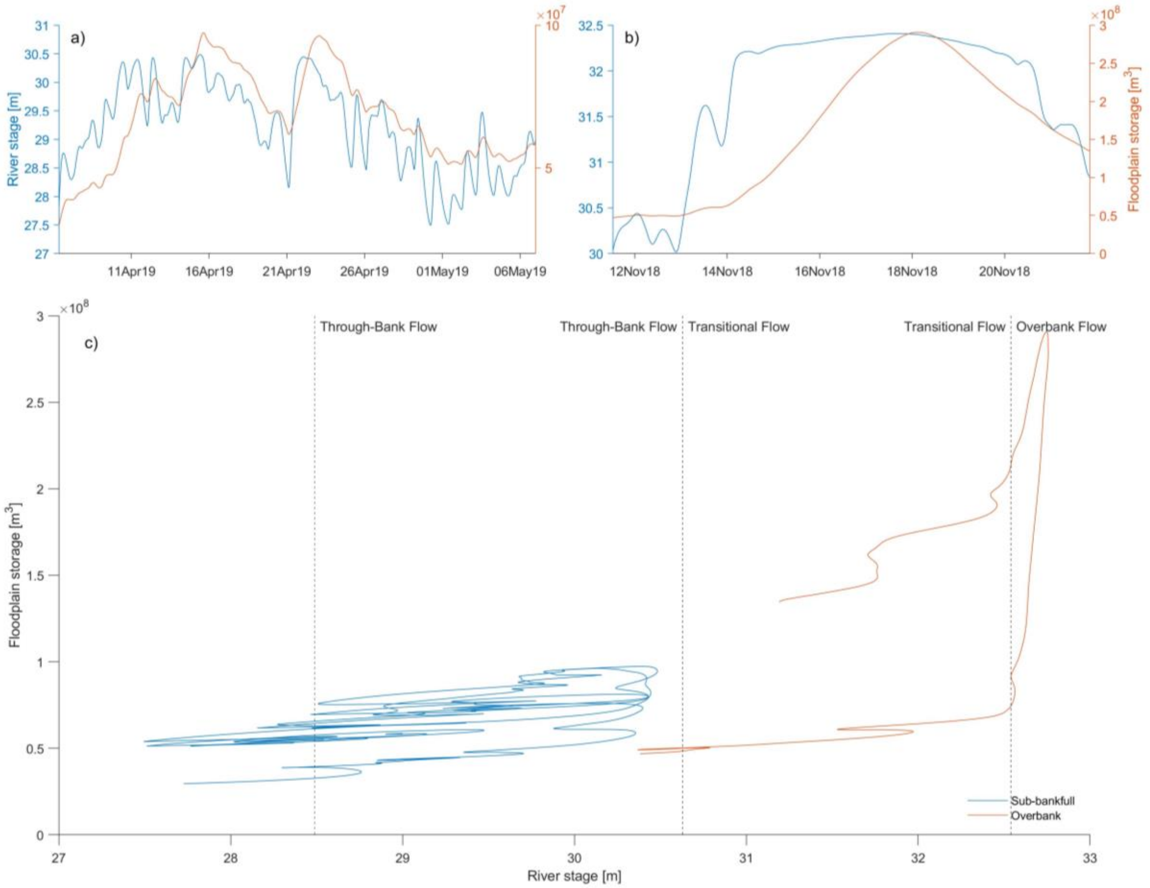

Figure 4.3: (a) Time series of river stage at USGS Gadsden and the instantaneous storage within the CNP for a sub-bankfull flow event. (b) Time series of river stage at USGS Gadsden and the instantaneous storage within the CNP for an overbank flow event. The stage-storage relationship for the sub-bankfull (a) and overbank (b) flow event. The presented data are model output from two quasi-realtime simulations (*Van der Steeg et al., 2022*).

The sub-bankfull stage-storage curve (i.e., Figure 4.3c) shows clear hysteresis (Figure 4.3a,c). As stage initially increases, the storage function gradually increases. The first peak in storage lags several earlier peaks in stage by more than one day. As stage declines after the 12 April peak, the storage declines after a half day lag. For rising stages on 14 April, the storage response lags by one day, with a maximum on 15 April. For the minimum on 21April, the storage does not decline to values observed earlier in the hydrograph for a similar stage (7 April), indicating that water is stored in the floodplain.

For the remainder of the hydrograph, the lag between stage and storage persists. The lagged response causes a counter-clockwise hysteresis. Furthermore, as water is stored in the floodplain, the hysteresis curve does not obtain initial values towards the end of the hydrograph.

During overbank flow water may enter the floodplain along the Congaree River, and from the upstream floodplain (*Van der Steeg et al., 2022*). These processes give rise to a broad and elongated hydrograph while the floodplain storage has a short-lived peak (Figure 4.3c). The peak occurs ~ 2 days after the peak in stage. The storage function does not respond to the minor peak on 12 November. Also, storage gradually increases as stage increases from 30.37 to 32.48 m. Thereafter, a rapid increase in storage occurs, while the stage remains relatively constant. The stage remains near-constant because the floodplain is actively accommodating the newly added water. At the start of the recession (stage 32.75 m), storage rapidly decreases while the stage is still above bankfull, and this rapid response is related to the overbank return of floodwaters from the floodplain to the river (*Van der Steeg et al., 2022*). Once the stage falls below the banks, storage becomes more gradual, and near steady at 31.73 and 32.35 m, corresponding the through-bank return of floodwaters to the river, or transition from wetting to draining.

Both the sub-bankfull and overbank flow events demonstrate hysteresis in the stage-storage relationship. Hysteresis for the overbank flow event is larger than for the sub-bankfull flow event. The larger hysteresis effects during overbank flow can be attributed to storage effects of the floodplain as inundation becomes more complete and water is transported to more remote locations, e.g., the system is trending toward the equilibrium wetting curve. Conversely, it takes substantially longer for the distant reaches to drain than for regions nearby the river as the system trends toward the draining curve. The hysteresis effects are smaller for sub-bankfull inundation because the total volume of water is smaller and of limited extent. Overall, the stage-storage analyses show that there is not a unique storage value for a given stage. Further, these analyses allow us to visualize how floodplains respond to flood waves, and, to identify the flow processes relevant to wetting and draining.

4.4.2 RATE OF CHANGE EFFECTS

4.4.2.1 SUB-BANKFULL WAVES

For sub-bankfull inundation, the stage-storage relationships show considerable variability for the synthetic rising limb gradient quantiles. Overall, the shallower rising limbs (Figure 4.2) give rise to conditions that favor greater transfer of water to the floodplain, and greater storage, relative to the steeper limbs (Figure 4.4a). For example, with wetting curve stages between 27.70 and 30.60 m, substantially more water is transported to the floodplain for shallower rising limbs. More specifically, the largest difference in storage occurs at ~29.25 m, where for the same river stage there is a factor of ~11 more water on the floodplain. In the transitions from wetting to draining curves, the storage initially increases as the stage starts to decline, and the overall storage is higher for gradually decreasing stage (Figure 4.4a).

Integrating storage over the hydrograph shows an overall downward trend (Figure 4.4b). The largest relative floodplain storage of ~50% is observed with the shallower rising limbs (Q_{10} and Q_{30}), and the lowest storage (20%) occurs at the steepest (Q_{100}). Storage up to Q_{60} varies slightly, centered at ~ 48% (Figure 4.4b). For waves $\geq Q_{70}$, the relative amounts of water stored decrease from nearly ~48 to ~23 %, indicating that steeper rising stages result in relatively smaller amounts of storage after the synthetic wave exited the domain and river stage has returned to initial values prior to the passing of the flood wave.

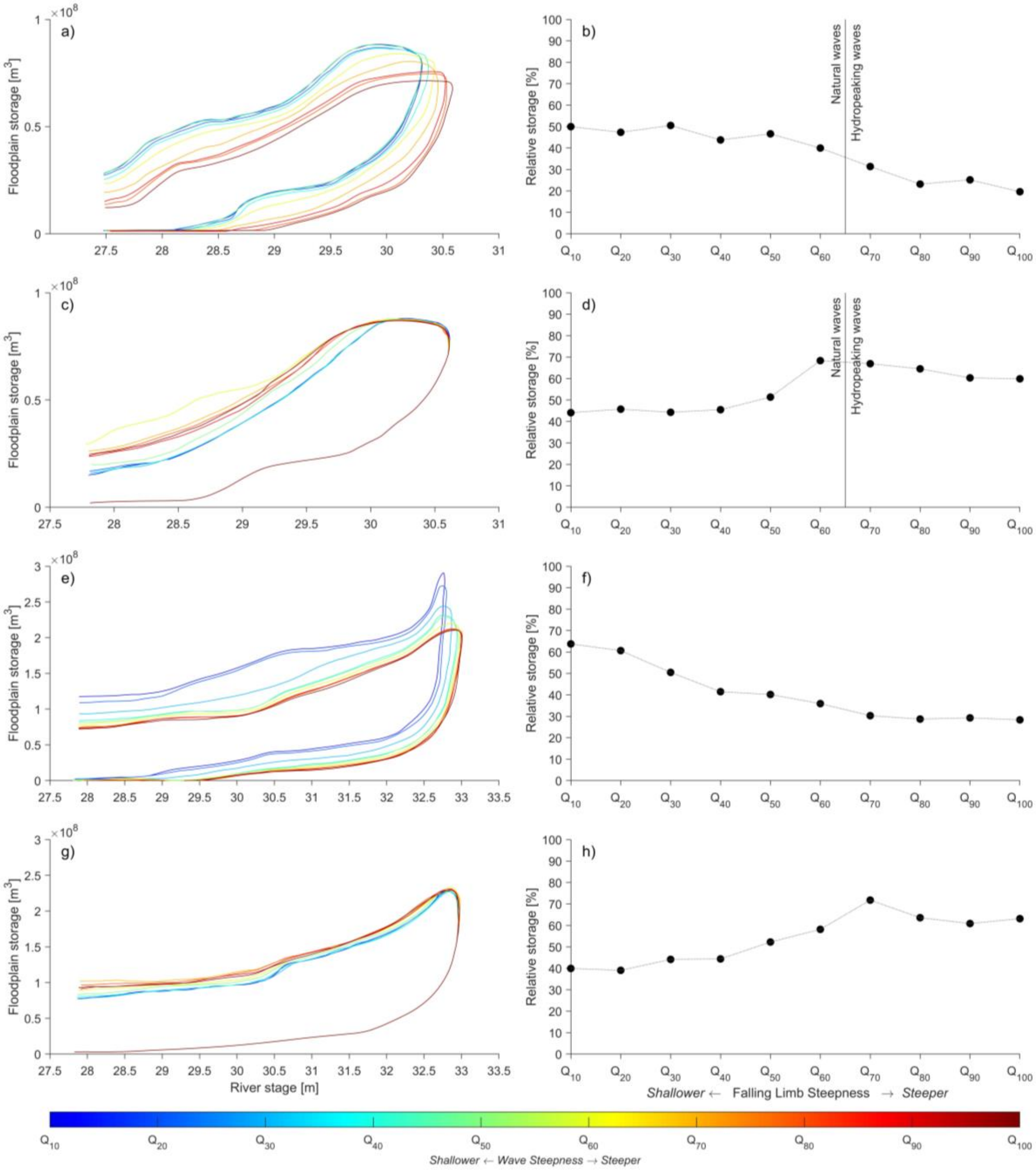

Figure 4.4: (a) the stage-storage relationship for sub-bankfull inundation with variable rising limbs and constant falling limb. (b) the relative floodplain storage as a function of the wave steepness for sub-bankfull waves with variable rising limbs constant falling limb. (c) the stage-storage relationship for overbank inundation with variable rising limbs and constant falling limb. (d) the relative floodplain storage as a function of the wave steepness

for overbank inundation with variable rising limbs and constant falling limb. (e) the stage-storage relationship for overbank inundation with variable rising limbs and constant falling limb. (f) the relative floodplain storage as a function of the wave steepness for overbank inundation with variable rising limbs and constant falling limb. (g) the stage-storage relationship for overbank inundation with a constant rising limb and variable falling limbs. (h) the relative floodplain storage as a function of the wave steepness for overbank inundation with a constant rising limb and variable falling limbs. The relative storage is the ratio of water stored in CNP over the total inflow in the river, and is calculated after the wave has passed. Cold colors indicate shallower wave gradients, warmer colors indicate steeper wave gradients.

When the hydrograph rising limb is held constant and the falling limb gradients are varied, the hysteresis curves vary considerably (Figure 4.4c). At the maximum stage of 30.35 m the drainage curves begin to separate, and they indicate an initial and slight increase in storage. Further along the drainage curve, the storage remains constant for the various recession limbs, but at ~30 m they separate further and thereafter remain approximately parallel, apart from for Q_{60}. The gradual recession curves have the least storage, progressively increasing to the steeper recession curves, although Q_{60} is distinguished as yielding the maximum storage below ~29.2 m. Assessments of total storage show a non-linear trend (Figure 4.4d), distinct from that above, with the variable rising limbs (Figure 4.4b). Initially, for falling limb attributes up to Q_{50} the storage is steady and centered around ~45% but increases to a maximum of 68% for Q_{60}. The relative amount of water stored decreases with increasing wave steepness, reaching ~60%. The floodplain storage for the steepest wave is on average larger than for the shallower waves (≤50th quantile).

In summary, for sub-bankfull inundation there are distinctly different responses in storage between hydrographs with variable rising and falling limbs. For instance, rising limbs give rise to variable floodplain storage in response to variable hydrograph gradients. Steeper rising limbs generally result in decreased floodplain storage; meanwhile, steeper hydrograph recession limbs result in increased storage. Hence, the rate of change of stage exerts a strong influence on floodplain inundation and storage, and a single stage does not define a unique degree of floodplain inundation.

4.4.2.2 OVERBANK WAVES

The overbank flow stage-storage relationships have similar trends that reveal hysteresis in all cases. In particular, the wetting curve gradually increases up to about 32.4 m but as stage continues to increase, there is an abrupt change toward a very sharp increasing trend (Figure 4.4e), indicating a factor of ~five increase for a stage increase of less than 0.4 m. The storage then reaches a maximum value, albeit at slightly different stages between hydrographs, as it transitions to the drainage curve. The drainage paths are subparallel and the Q_{60}-Q_{100} paths are indistinguishable. Likewise, the Q_{10} andQ_{20} curves differ slightly, but in all cases the more gradual hydrograph rising limbs indicate substantially more storage, nearly double at 30 to 30.5 m (Figure 4.4e). On the Q_{10-20} drainage curves, a clear “shoulder” in the storage trend occurs for stages 30.6 – 32 m (Figure 4.4e). For the remainder of the falling limb, the storage decreases gradually as river stage falls. When the river stage returns to 27.45 m, the absolute floodplain storage is smaller for steeper hydrographs. Lastly, it is noteworthy that the shapes of the $Q_{10,\ 20}$ hysteresis curves closely mimic the hysteresis detected in the analyses of field data (Figure 4.3c); the others do not. The total floodplain storage function shows an overall downward trend (Figure 4.4f), from ~61% observed with Q_{10}, and the lowest storage of 28% with Q_{100}. In between, the storage function progressively decreases with local uniform regions present in storage (Q_{40-60}). The most significant decrease in storage occurs between Q_{20-30}. The overall decreasing trend is similar to that for sub-bankfull inundation (Figure 4.4b).

Varying the hydrograph falling limb gradients shows that the hysteresis curves have considerably less variability (Figure 4.4g). Note that the rising limb is held constant, and the floodplain is initially dry. Under these conditions, the wetting curve shows a gradual increase in storage, but at 32.7 m there is an apparently exponential increase. The transition to drainage occurs at ~32.9 m. As the stage declines, for all gradient quantiles, the storage slightly increases before declining. For the remainder of the draining stage interval, the storage decreases and the drainage curves have nominal differences, although the Q_{60-100} values are consistently but slightly higher. Integrated over the hydrograph, the floodplain storage shows a non-linear trend (Figure 4.4h), albeit an overall increasing trend in floodplain storage with increasing steepness. The minimum floodplain storage of ~40% occurs with the lower falling limb Q values. Thereafter, the storage gradually increases to the maximum storage at Q_{70} with ~72%. With the falling limb conditions of Q_{80}, the storage decreases, but beyond that, the storage the storage remains nearly constant.

In summary, the overbank inundation process leads to variable relative floodplain storage as a function of the steepness of the hydrograph rising and the falling limbs. As with sub-bankfull inundation, steeper rising stages result in decreased relative floodplain storage. Steeper falling limbs, generally increase the relative amounts of floodplain storage, although the relationship is non-linear. A local maximum in floodplain storage is observed at a falling stage steepens of Q_{70}; for steeper falling limbs, the storage decreases and remains fairly constant. Hence, at bankfull the river stage remains nearly constant while the storage increases substantially, and the river stage is higher for steeper flood waves. The near-vertical storage increase indicates that, although bankfull stage is defined by the elevation of riverbanks, the response between river stage and storage for overbank flow differs based on the steepness of the hydrograph rising limb.

4.4.3 INITIAL INUNDATION EFFECTS

Here we investigate the combined influence of initial floodplain inundation and the rate of change of river stage on hysteresis. The effects of preceding inundation on floodplain storage are presented as stage-storage curve and plots of initial floodplain inundation versus relative floodplain storage (e.g., Figure 4.5a). The stage-storage curves are only shown for Q_{10} and Q_{100}, and for inundation depths of 0.1 and 0.5 m to enhance the visualization of the results. The integrated relative storages are shown for all quantiles and all inundation depths (e.g., Figure 4.5b). The computations only include newly added river water to allow for an inter-model comparison.

4.4.3.1 SUB-BANKFULL WAVES

For different sub-bankfull hydrographs, the wetting curves in the stage-storage relationships for Q_{10} and Q_{100} are nearly identical, respectively, and therefore independent of initial floodplain inundation (Figure 4.5a). A slight and initial deviation of the curves occurs in the draining phase. The drainage curves are subparallel, however, with higher prior inundation conditions that result in high water retention. The hysteresis curve shapes differ also in that the Q_{10} wetting and drainage curves generally indicate greater storage, and the steeper hydrograph rising limb produces higher river stages, but with lower storge. These results indicate that exchange with the floodplain is lower for steep hydrographs as with a dry floodplain (Figure 4.4a)

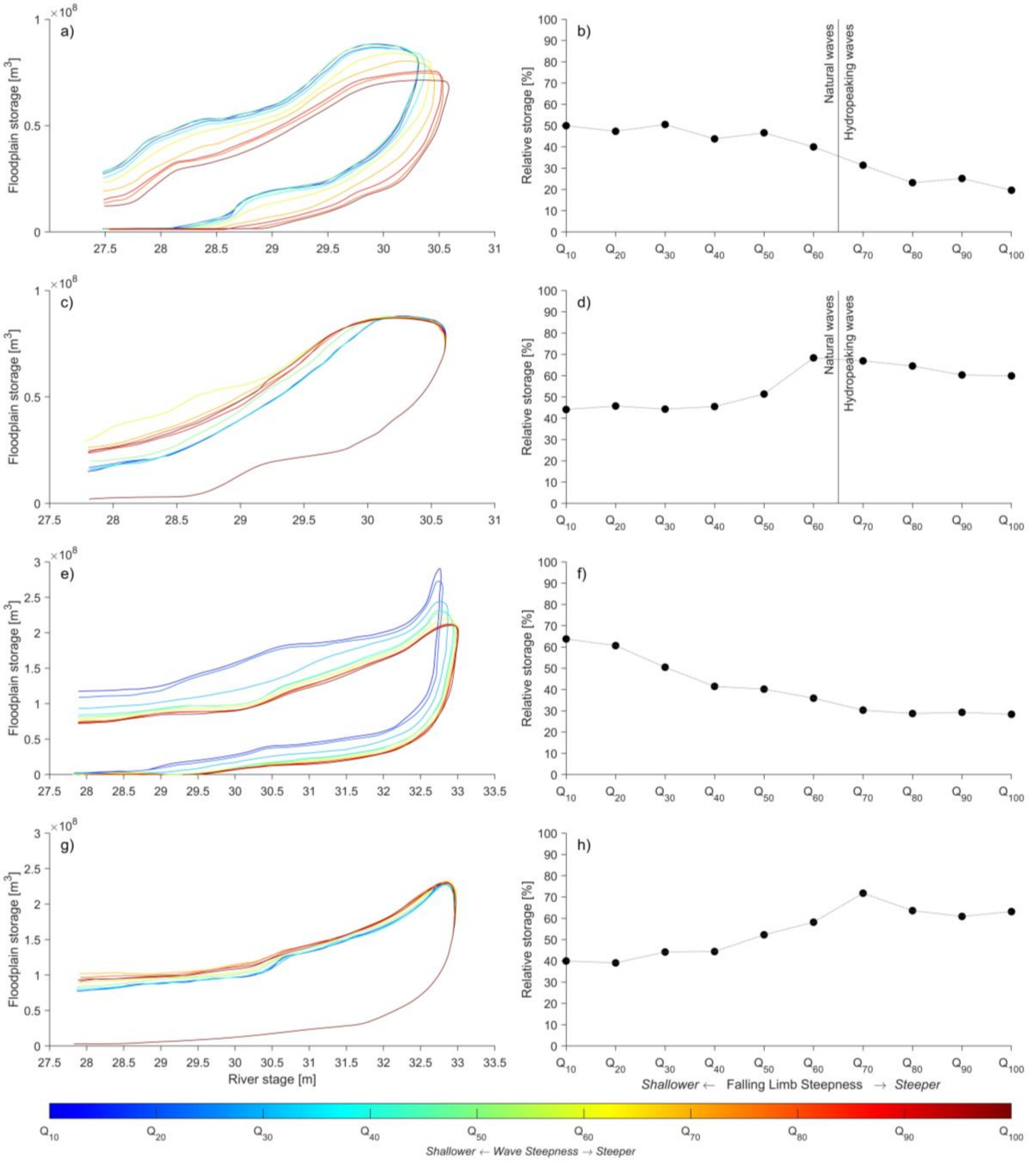

Figure 4.5: (a) the stage-storage relationship for sub-bankfull inundation with variable rising limbs and constant falling limb with initial floodplain wetting (b) the relative floodplain storage as a function of the wave steepness for sub-bankfull waves with variable rising limbs constant falling limb with initial floodplain wetting (c) the stage-storage relationship for overbank inundation with variable rising limbs and constant falling limb with initial floodplain wetting. (d) the relative floodplain storage as a function of the wave steepness for overbank inundation with variable rising limbs and constant falling limb with initial floodplain wetting. (e) the stage-storage relationship for overbank inundation with variable rising limbs and constant falling limb with initial floodplain wetting. (f) the relative floodplain storage as a function of the wave steepness for overbank inundation

with variable rising limbs and constant falling limb with initial floodplain wetting. (g) the stage-storage relationship for overbank inundation with a constant rising limb and variable falling limbs with initial floodplain wetting. (h) the relative floodplain storage as a function of the wave steepness for overbank inundation with a constant rising limb and variable falling limbs with initial floodplain wetting. The relative storage is the ratio of water stored in CNP over the total inflow in the river, and is calculated after the wave has passed. Cold colors indicate shallower wave gradients, warmer colors indicate steeper wave gradients.

Analyses of the corresponding relative storage show that the effects of initial floodplain wetting are highly variable with a largely concave-like trend for all quantiles (Figure 4.5b). For Q_{10}, the floodplain storage increases steadily from ~47% to 78% at 0.4 m. Thereafter, the relative floodplain storage declines. A similar trend is observed for Q_{20}. However, for Q_{30}, the storage increases steadily from ~46% to 72%, but the maximum occurs at initial inundation depth of 0.3 m; a different depth than observed at shallower rising stages. This trend applies to the other Q quantile values. For increasing flood wave steepness, the maximum floodplain storage occurs at smaller depths of initial floodplain wetting. The peak in storage shifts towards the left for steeper rising stages (Figure 4.5b), indicating that shallower rising stages develop enhanced storage for a higher initial inundation depth while steeper hydrographs increase storage for lower initial depths.

When the hydrograph rising limb is held constant and the falling limb gradients are varied, the wetting and drainage curves for Q_{10} are closely aligned and the impact of prior inundation on floodplain storage is negligible (Figure 4.5c). For Q_{100}, however, there is a substantial influence of initial condition. The wetting curves are similar, but some separation occurs, and more water is stored for Q_{100} with prior inundation depth of 0.1 m. Therefore, the presence of water does influence inundation, although the influence appears minimal. At the start of the drainage phase, the curves for 0.1 and 0.5 m prior inundation are identical, and separations occurs at stages lower than ~30.1 m. The curve with 0.1 m prior inundation drains less efficiently, and a larger amount of water is stored in the floodplain when the stage returns of 27.45 m. Generally, the floodplain storage functions decrease for increasing initial inundation depths for all Q quantiles (Figure 4.5d). Rates of decline of the storage is greater for steeper falling limbs while the storage function for the quantiles smaller than Q_{10} falling limb is approximately horizontal. The foregoing indicates that for steeper falling stages, larger initial inundation depths produce enhanced floodplain drainage. Lastly, it is noteworthy that the Q_{100} with a prior inundation depth of 0.5 m produces enhanced drainage compared to Q_{10} for the prior inundation values.

In summary, the effects of initial floodplain wetting on relative floodplain storage for sub-bankfull waves is highly variable but demonstrates a similar trend across the various hydrograph rising quantiles. Generally, shallower rising stages produce enhanced inundation for higher prior depths, while for a steeper rising limb, enhanced inundation occurs at lower prior inundation depths. The drainage process for steep falling limbs is enhanced by larger prior depths, resulting in less water retention. For shallow falling limbs, the drainage process appears to be independent of initial floodplain inundation.

4.4.3.2 Overbank BANKFULL WAVES

For overbank flood waves with variably sloped hydrographs, initial floodplain wetting does not have a substantial influence on the wetting and drainage curves for Q_{100} (Figure 4.5e). For Q_{10}, there is a substantially influence of initial condition. The wetting curves are similar, but some separation occurs between stage of 32.25 and 32.75 m, with higher prior inundation resulting in larger amounts of water transferred into the floodplain at a slightly lower stage. The drainage curves are near-identical at the start of the draining phase. A substantial separation occurs for stages lower than ~32.2 m, with a higher prior inundation depth resulting in enhanced drainage compared to the lower prior inundation depth. The total floodplain storage function shows an overall downward trend (Figure 4.5f) depths for all Q quantiles (Figure 4.5d). The largest rate of decrease is observed with Q_{10}, while for steepness greater than Q_{10}, the storage functions align and are approximately horizontal, indicating that inundation is independent of initial floodplain inundation. Overall, shallow rising stages are primarily affected by prior inundation, while for steeper rising stages prior inundation does not affect the floodplain storage.

In summary, the effects of initial floodplain wetting on relative floodplain storage for overbank waves is variable but demonstrates a similar trend across the various hydrograph rising quantiles. Generally, shallower rising limbs and lower prior inundation depths produce enhanced inundation. Larger prior inundation depths result in less water flux to the floodplain. The drainage process for overbank waves appears independent of initial floodplain wetting across all Q quantiles.

4.5 DISCUSSION

For sub-bankfull waves we showed that steeper hydrograph rising limbs result in a up to ~40% smaller flux to the floodplain, while causing higher water levels in the river. More gradual rising limb gradients, however, indicate enhanced storage and we interpret this as an enhanced water flux to the floodplain, and overall lower river stages. In addition, shallower rising limbs initiate detectable river-floodplain exchange at lower stages than for steeper gradients. For the same floodplain storage, shallower recession limb gradients promote floodplain drainage while steeper limbs leave more water in the floodplain after the flood passes. In both the rising and falling gradient analyses, a sudden change in river-floodplain exchange was observed in the transition from ‘natural’ and the flood waves associated with dam releases, especially for hydropower (e.g., *Doyle, 2009; Conrads et al., 2008; Patterson et al. 1985*).

For overbank flood waves, the river-floodplain flux decreases with increasing rising limb gradients, with differences in the storage of up to ~44%. The steeper rising limbs result in higher river water levels of up to 0.30 m. Shallower overbank rising limb gradients promote water flux to the floodplain and lower river stages. As with sub-bankfull waves, shallower rising limbs initiate river-floodplain exchange at lower stages than for steeper gradients. For the same initial floodplain storage, steeper recession limbs generally result in higher amounts of water left in the floodplain after the river wave passes. Shallower falling stages, enhance drainage processes resulting in lower water amounts stored in the floodplain integrated over the full hydrograph.

The presence of water in the floodplain affects floodplain inundation and drainage processes. For sub-bankfull rising stages, shallower rising limb gradients produce enhanced inundation with greater prior inundation depths while steeper stage increases benefit from lower initial depths. Larger prior inundation depths produce enhanced drainage for sub-bankfull draining process, especially for steeper falling stages, resulting in relatively less water being stored in the park. For overbank rising stages, higher initial depths result in lower amounts of water transported into the floodplain. Higher initial depths deter floodplain inundation; more water is stored for lower initial depths. For steeper rising gradients, the storage does not change with larger initial depths. Overbank drainage processes seem insensitive to initial depths for the various declining stages.

Substantial variability in flow patterns for CNP has been observed in-situ measurements *(Van der Steeg et al., 2021*) and in simulations *(Van der Steeg et al., 2022)*. Both the observations and simulations show that floodplain flows can be predictably simple or complex, for different water stages and between locations, and the effects are largely controlled by inundation processes. Flows during sub-bankfull inundation are particularly variable, including multiple abrupt flow reversals, while overbank inundation gives a more subdued response with slow ~90° rotations. During sub-bankfull inundation, the local geomorphic structures disperse or confine flows that are routed through floodplain interior. However, with higher overbank flows the rate of change of river stage is a more important driver of flow complexity than local relief. Furthermore, flow reversals at locations near the river show strong correlations with stage, but less so in the floodplain interior. For the various synthetic hydrographs, flow directions are unique due differences in the rate of change of the rising and falling stages. The unique floodplain flow patterns produce different stage-storage relationships, and indicate that that a single stage in the main channel does not uniquely define floodplain flow hydraulics; the rate of change effect substantially influences floodplain inundation and drainage dynamics.

Slowly rising hydrographs allow for the distribution of floodwater to the floodplain to keep pace with the changing river stage (e.g., *Lewin and Hughes, 1980*). When the distribution of inundating waters can keep pace with river stage (i.e., a slow rise), more water will be transported at the same stage than with a steep rising wave, as is evident by the stage-storage curve for variable rising stage for sub-bankfull and overbank flow (Figure 4.4a,e). Steep falling limbs indicate that the river stage and floodplain storage are out of phase, and has been interpreted as a condition where internal floodplain drainage processes cannot keep pace with the falling river stage (*Lewin and Hughes, 1980; Makungu and Hughes, 2021)*. This may result in larger amount of water left in the floodplain, especially at remote locations, compared to shallower falling stages with the same river stage.

To help communicate and visualize our findings, we adapt the so-called “bathtub” storage model (e.g., *Xu et al., 2021; Aucelli et al., 2017; Nobre et al., 2016*). This model considers the floodplain as a box (Figure 4.6) that fills with water once the stage in an adjoining river exceeds bank elevation, after which water fills the box instantaneously to the river stage. Hence, when the river exceeds bank elevation, an undefined amount of water may enter the box determined by river stage. When the river stage declines to elevation below the bank, water in the floodplain above bank height may return to the river, instantaneously. However, the general bathtub model does not incorporate the effects of different rates of rising and falling stages. Here, we adjust the general bathtub framework to account for these factors.

First, we ignore the notion of overbank flow (i.e., river exceeds back elevation), and define a wall with infinite height between river and floodplain (Figure 4.6). To account for through-bank and overbank flow, two pipelines go through the wall: one below bank height (S1) and one above bank height (O1). For both flow conditions, a second pipeline, with a smaller diameter is added to their respective elevations (S2 and O2). The smaller diameter accounts for different flow rates, corresponding to the different rates of increases in storage. For both sub-bankfull and overbank flow conditions, the smaller tube corresponds to steeper gradients as steeper rising stages transport less water into the floodplain than shallow gradients (Figure 4.4a and 4.4e). Steeper overbank rising stages results in a higher water level in the river (Figure 4.4a and 4.4e), however, a relatively smaller amount of water is transported into the floodplain (Figure 4.4b). The outflow also consists of 2 tubes for each flow condition, with a smaller diameter for steeper waves. As with the inflow, the smaller diameter pipeline corresponds to steeper falling stages and accounts for reduced outflow observed during steep falling limbs (Figure 4.4c and 4.4g). The transition from one pipeline to another (small to large) remains poorly defined. However, the presented improved bathtub model accounts for sub-bankfull flow and for variations of rising and falling stages; it summarizes our most important findings, and it provides a conceptual framework for an improved understanding of floodplain wetting and draining.

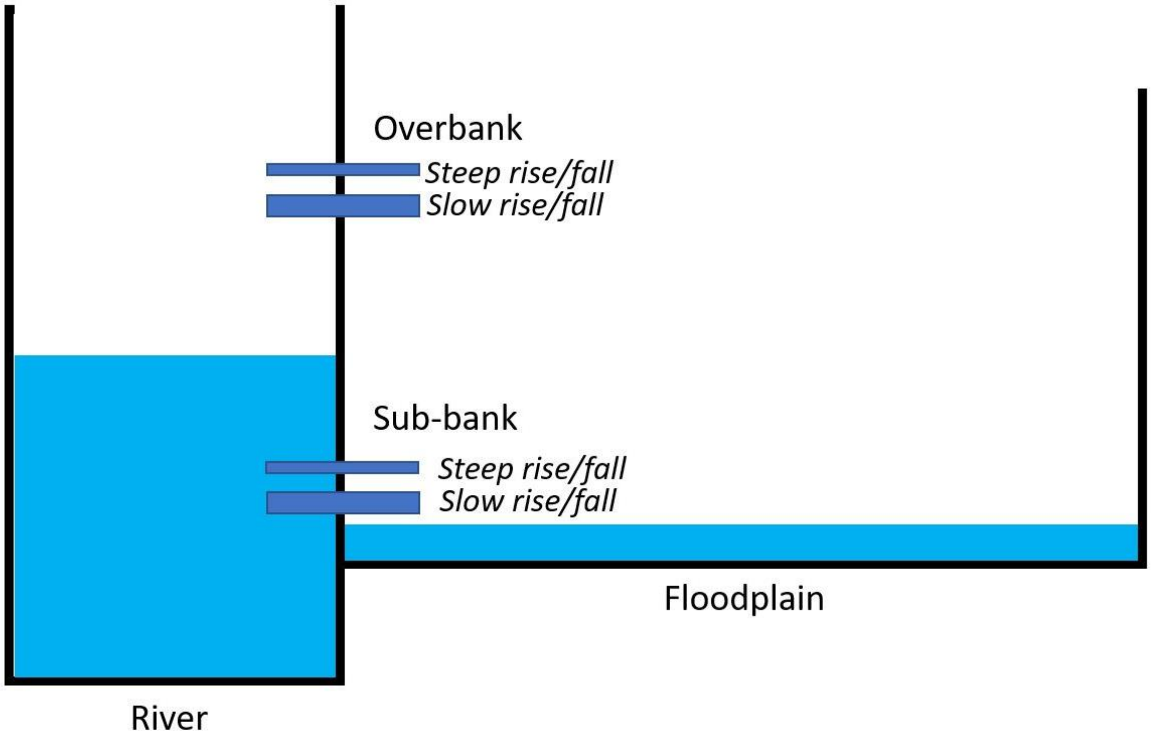

Figure 4.6: Conceptual model to account for effects of wave steepness on simplified river-floodplain storage models. An artificial, infinitely high wall separates the river from the floodplain. 4 tubes cut through: 2 for sub-bankfull inundation and 2 for overbank inundation. The two sets of tubes have varying diameters to account for varying inflow that

depend on wave steepness. The tube for slow rising waves, are larger as they allow larger amounts of water to be transported into the floodplain. These tubes are also positioned at lower elevations as slow rising waves allow river-floodplain exchange at lower river stages.

The hysteresis effects visible in the stage-area relationships are not uniquely defined for the Congaree River floodplain system. The stage measurements were taken at the most upstream edge of the storage monitoring area, the national park. Because the wave arrives at the gauge before entering the monitoring area (i.e., the park), a counter-clockwise hysteresis effect is observed (Figure 4.3c). When river stage measurements are taken further downstream the stage-storage relationship shifts to a clockwise loop. The variability in the direction of the loop is caused by the change between the stage measurements and the storage function. For example, if the stage measurements downstream of the park were related to the storage function of CNP, the stage-storage relationship loop is clockwise because the peak in storage occurs before the maximum stage. The relative position of stage and storage measurements is especially important for comparative analyses of hysteresis amongst floodplains. For example, *Ang et al. (2022)* conducts a comparative analysis of floodplains in an attempt to glean insight into the geomorphic control of the stage-area relationship of three major floodplain lakes. The approach, however, precludes the assessment of geomorphic controls on hysteric effects as relative position of stage and area measurements are not consistent among their analyzed floodplains.

Overall, our study highlights complex floodplain flows in response to varying forcing conditions consisting of sub-bankfull and overbank hydrographs with varying rising and falling limb gradients, and the effects of initial floodplain wetting. Understanding the effects of various forcing conditions on floodplain flows has implications for floodplain hydraulic connectivity, taken as the degree of surface water exchange between a river and its floodplain (e.g., *Amoros and Bornette, 2002; Passalacqua, 2017; Wohl et al., 2019)*. Hydraulic connectivity can be expected to vary considerably with variations in stage (e.g., *Amoros & Bornette, 2002; Xu et al., 2021; Czuba et al., 2019*). Here, we demonstrated that hydraulic connectivity is not solely dependent on stage height but is also influenced by the rates of rising and falling stages and the presence of initial water on the floodplain. Furthermore, understanding the dynamic response of floodplains to variable forcing conditions aids in flood hazard and prediction, and mitigation analyses. For example, steeper rising waves generally result in higher river water levels, and therefore impacts the ability of floodplains to attenuate flood waves. Additionally, hydro-peaking waves generally have steep rising limbs and impact floodplain inundation processes by reducing river-floodplain exchange. As more and more rivers are dammed (e.g., *Zhang and Gu, 2023, Arif et al., 2022; Elliott et al., 2019*) for hydropower purposes, the assumptions about ecological benefits of dam releases ultimately depend on the influence on hydrograph shape on the extent and depth of floodplain wetting.

4.6 CONCLUSIONS

Floodplain stage-storage analyses provide detailed insight on floodplain wetting and drainage processes. Field observations and simulation results show that floodplain stage-storage hysteresis is a regularly occurring feature. For both sub-bankfull and overbank floodplain inundation, steeper hydrograph rising limbs result in reduced water fluxes to the floodplain, while causing higher water levels in the river. Shallower rising gradients, however, enhance floodplain inundation and results in lower river water levels. Slow stage increases allow for the distribution of floodwater to keep pace with river stage, and more water will be transported into the floodplain at the same stage than with steep rising gradients. Shallow recession limb stage gradients produce enhanced floodplain drainage for both sub-bankfull and overbank inundation. When the floodplain stage lags the river stage the river stage and floodplain storage are out of phase and the internal floodplain drainage processes cannot keep pace with the falling river stage, resulting in greater floodplain water retention and the development of a recession wave that advances inland. The presence of initial floodplain wetting shows a non-linear trend between wave gradients, storage, and initial inundation depths. For sub-bankfull waves, higher prior depths mostly enhance inundation for shallower rising gradients, while lower initial depths produce enhanced floodplain flux for steeper waves. For overbank rising gradients, initial floodplain wetting generally reduces water fluxes to the floodplain. For drainage phase, higher initial depths augment drainage for sub- bankfull flows, while for overbank flows, drainage processes appear insensitive to initial depths. The temporal and spatial dynamics of floodplain wetting and drainage dynamics have important implications for dam management and water release strategies that are intended to improve ecosystem sustainability.

CHAPTER 5

CONCLUSIONS

The objective of this study is to increase the fundamental understanding of river and floodplain interactions, specifically focusing on surface-water floodplain circulation, inundation and drainage processes over a complex, but low-relief and low-gradient floodplain. Congaree River and floodplain in South Carolina, USA, is used as the study site because of pristine condition, the topographic complexity of the floodplain, and highly variable hydrologic conditions which allow for investigations of floodplain circulation dynamics under low, intermediate, and high flow conditions.

This work combines detailed analysis field field measurement, topographic analysis of floodplain channels and connected networks, and process-based hydrodynamic modelling to obtain deeper insight into processes governing the wetting, circulation, and draining of floodplains.

This chapter summarizes the conclusions sections of the separate chapters that make this dissertation by addressing the research questions formulated in Chapter 1

5.1 *Determine in-situ spatial and temporal variability of flow in the floodplain under variable hydrologic forcings conditions.*

An in situ three-point approach for the estimation of mesoscale (~0.01 km^2) free surface gradients and flow directions for inundated landscapes is presented as the "triangular facet approach." Analyses of the maximum gradient data acquired at, and averaged over, 0.25-hr intervals show that floodplain flows can be predictably simple or complex, for different water stages and between locations, and the effects are largely controlled by inundation process. Flows during sub-bankfull inundation are particularly variable, including multiple abrupt flow reversals, while overbank inundation gives a more subdued response with slow ~90° rotations. During sub-bankfull inundation, the local relic geomorphic structures influence flows that are routed through the floodplain interior. However, with higher overbank flows, the rate of change of stage is a more important driver of flow complexity than local relief. Overall, the triangular facet approach provides robust information on flow dynamics that can greatly enhance the utility of data from satellite remote sensing and acoustic current measuring devices, and numerical simulations of flow.

5.2 *Determine the topographic controls on flow dynamics under dynamic hydrologic conditions.*

A robustly calibrated and validated hydrodynamic model depicts flow patterns over a topographically complex floodplain with a heterogeneous main channel levee. Simulations highlight floodplain inundation dynamics for two conditions, the passage of sub-bankfull and overbank flood waves. Sub-bankfull inundation commences with the passage of the flood wave crest beyond the lower elevation levee breaches, and floodplain wetting is guided by the channel network. Hence, the upstream sub-bankfull inundation area expands while much of the downstream floodplain remains dry. The onset of overbank flow is spatially variable but becomes continuous, and the through-bank channels persist as preferential pathways that produce higher velocity flows several kilometers inland. Meanwhile, near-stagnant zones develop between through-bank channel mouths, where water is temporarily stored and routed to the channel network. Overall, floodplain wetting and draining processes significantly influence flow direction, and characteristics of the flood wave over the floodplain surface such that a single stage in the main channel does not uniquely define floodplain flow hydraulics. Given these findings we propose that assessments of floodplain hydraulic connectivity account for the effects of heterogeneous levee structure and intra-floodplain exchanges, as well as the typical flow thresholds associated with submergence and emergence of topography.

5.3 *Determine the factors of river hydrographs that control and influence floodplain flow dynamics and storage processes.*

Floodplain hysteresis in the river stage and floodplain storage relationship has been investigated using a robustly calibrated and validated hydrodynamic capable of reproducing flow patterns over a topographically complex floodplain that includes a heterogeneous main channel levee. Synthetic hydrographs were used to reduce the complexity in the analyses of floodplain inundation dynamis and model output, and to help characterize governing flow processes. Four hundred observed sub-bankfull and overbank waves from a long-term data set were analyzed to obtain estimates of rising and falling gradients, stage variations, and wave periods and were used to guide the development of synthetic hydrographs. Findings indicate that shallow rising gradients produce enhanced floodplain inundation and result in lower river water levels for both sub-bankfull and overbank inundation. Steeper rising gradients deter inundation processes and cause higher water levels in the river. River-floodplain exchange for shallow rising stages is initiated at lower river stages than for the same stage during a steep rise. Similarly, shallow falling stages enhance overall floodplain drainage processes for sub-bankfull and overbank inundation. Steep falling stages, however, result in greater floodplain water retention. The substantial variation in inundation and drainage processes results from highly variable and complex flow patterns resulting from various rates of change of stage that appear to be dependent on flow thresholds associated with submergence and emergence of topography. A single stage in the main does not uniquely define floodplain hydraulics, rate of change of stage is a controlling factor. Given these findings, we propose that assessment of floodplain hydraulic connectivity accounts for the effects of rates of change of stage as determining factor controlling river-floodplain surface-water connectivity

REFERENCES

Alsdorf, D. E., Rodríguez, E., & Lettenmaier, D. P. (2007a). Measuring surface water from space. *Reviews of Geophysics*, *45*(2).

Alsdorf, D., Bates, P., Melack, J., Wilson, M., & Dunne, T. (2007b). Spatial and temporal complexity of the Amazon flood measured from space. *Geophysical research letters*, *34*(8).

Amoros, C., & Bornette, G. (2002). Connectivity and biocomplexity in waterbodies of riverine floodplains. *Freshwater biology*, *47*(4), 761-776.

Andraos, J. (1996). On the propagation of statistical errors for a function of several variables. *Journal of chemical education*, *73*(2), 150.

Ang, W. J., Park, E., & Yang, X. (2022). Geomorphic control on stage-area hysteresis in three of the largest floodplain lakes. *Journal of Hydrology*, *614,* 128574.

Arcement, G. J., & Schneider, V. R. (1989). Guide for selecting Manning's roughness coefficients for natural channels and flood plains.

Arif, M., Jie, Z., Tahir, M., Xin, H., & Changxiao, L. (2022). The impact of stress factors on riparian and drawdown zones degradation around dams and reservoirs. *Land Degradation & Development*, *33*(12), 2127-2141.

Aucelli, P. P. C., Di Paola, G., Incontri, P., Rizzo, A., Vilardo, G., Benassai, G., ... & Pappone, G. (2017). Coastal inundation risk assessment due to subsidence and sea level rise in a Mediterranean alluvial plain (Volturno coastal plain–southern Italy). *Estuarine, Coastal and Shelf Science*, *198,* 597-609.

Baptist, M. J., Penning, W. E., Duel, H., Smits, A. J., Geerling, G. W., Van der Lee, G. E., & Van Alphen, J. S. (2004). Assessment of the effects of cyclic floodplain rejuvenation on flood levels and biodiversity along the Rhine River. *River Research and Applications*, *20*(3), 285-297.

Barnes, H. H. (1967). *Roughness characteristics of natural channels* (No. 1849). US Government Printing Office.

Box, W., Järvelä, J., & Västilä, K. (2021). Flow resistance of floodplain vegetation mixtures for modelling river flows. *Journal of Hydrology*, *601*, 126593

Byrne, C. F., Stone, M. C., & Morrison, R. R. (2019). Scalable flux metrics at the channel-floodplain interface as indicators of lateral surface connectivity during flood events. *Water Resources Research*, *55*(11), 9788-9807.

Castellarin, A., Domeneghetti, A., & Brath, A. (2011). Identifying robust large-scale flood risk mitigation strategies: A quasi-2D hydraulic model as a tool for the Po river. *Physics and Chemistry of the Earth, Parts a/b/c*, *36*(7-8), 299-308.

Conrads, P., Feaster, T. D., & Harrelson, L. G. (2008). *The effects of the Saluda Dam on the surface-water and ground-water hydrology of the Congaree National Park Flood Plain, South Carolina* (No. 2008-5170). Geological Survey (US).

Czuba, J. A., David, S. R., Edmonds, D. A., & Ward, A. S. (2019). Dynamics of surface-water connectivity in a low-gradient meandering river floodplain. *Water Resources Research*, *55*(3), 1849-1870.

D'Elia, A. H., Liles, G. C., Viers, J. H., & Smart, D. R. (2017). Deep carbon storage potential of buried floodplain soils. *Scientific reports*, *7*(1), 1-7.

David, S. R., Edmonds, D. A., & Letsinger, S. L. (2017). Controls on the occurrence and prevalence of floodplain channels in meandering rivers. *Earth Surface Processes and Landforms*, *42*(3), 460-472.

Day, G., Dietrich, W. E., Rowland, J. C., & Marshall, A. (2008). The depositional web on the floodplain of the Fly River, Papua New Guinea. *Journal of Geophysical Research: Earth Surface*, *113*(F1).

Deltares (2022a). D-Flow Flexible Mesh User Manual. Delft, The Netherlands: Deltares.

Deltares (2022b). D-Flow Flexible Mesh Technical Reference Manual. Delft, The Netherlands: Deltares.

Doyle, T. W. (2009). Modeling flood plain hydrology and forest productivity of Congaree Swamp (p. 46). US Geological Survey.

Dunne, T.*,* *&* Aalto, R. E. *(*2013*).* Large river floodplains. *In* J. Shroder*,* *&* E. Wohl *(Eds.),* Treatise on geomorphology*,* fluvial geomorphology *(Vol.* 9*, pp.* 645–678*).* San Diego, CA*: Elsevier Academic Press.*

Elliott, M., Day, J. W., Ramachandran, R., & Wolanski, E. (2019). A synthesis: what is the future for coasts, estuaries, deltas and other transitional habitats in 2050 and beyond?. In *Coasts and estuaries* (pp. 1-28). Elsevier.

Fagan, S. D., & Nanson, G. C. (2004). The morphology and formation of floodplain-surface channels, Cooper Creek, Australia. *Geomorphology*, *60*(1-2), 107-126.

Filgueira-Rivera, M., Smith, N. D., & Slingerland, R. L. (2007). Controls on natural levee development in the Columbia River, British Columbia, Canada. *Sedimentology*, *54*(4), 905-919.

Fischer, C., Damm, C., Foeckler, F., Gelhaus, M., Gerstner, L., Harris, R., ... & Scholz, M. (2019). The "habitat provision" index for assessing floodplain biodiversity and restoration potential as an ecosystem service—Method and application. *Frontiers in Ecology and Evolution*, *7*, 483.

Fleischmann, A. S., Paiva, R. C., Collischonn, W., Sorribas, M. V., & Pontes, P. R. (2016). On river-floodplain interaction and hydrograph skewness. *Water Resources Research, 52*(10), 7615-7630.

Freeze, A., and J. Cherry. 1979. *Groundwater*. Prentice-Hall, Englewood Cliffs, New Jersey. 604 pp.

Funk, A., Tschikof, M., Grüner, B., Böck, K., Hein, T., & Bondar-Kunze, E. (2020). Analysing the potential to restore the multi-functionality of floodplain systems by considering ecosystem service quality, quantity and trade-offs. *River Research and Applications, 37*(2), 221-232.

Gaddy, L. L., & Smathers, G. A. (1980). The vegetation of the Congaree Swamp National Monument. *Veroff Geobot. Inst. ETH, Stiftung Rubel, Zurich, 69*, 171-182.

Girard, P., Fantin-Cruz, I., De Oliveira, S. M. L., & Hamilton, S. K. (2009). Small-scale spatial variation of inundation dynamics in a floodplain of the Pantanal (Brazil). *Hydrobiologia, 638*(1), 223-233.

González-Sanchis, M., Murillo, J., Latorre, B., Comín, F., & García-Navarro, P. (2012). Transient two-dimensional simulation of real flood events in a Mediterranean floodplain. *Journal of Hydraulic Engineering, 138*(7), 629-641.

Hamilton, S. K., Kellndorfer, J., Lehner, B., & Tobler, M. (2007). Remote sensing of floodplain geomorphology as a surrogate for biodiversity in a tropical river system (Madre de Dios, Peru). *Geomorphology, 89*(1-2), 23-38.

Harvey, J. W., Schaffranek, R. W., Noe, G. B., Larsen, L. G., Nowacki, D. J., & O'Connor, B. L. (2009). Hydroecological factors governing surface water flow on a low-gradient floodplain. *Water Resources Research, 45*(3).

Hughes, D. A. (1980). Floodplain inundation: Processes and relationships with channel discharge. *Earth Surface Processes, 5*(3), 297-304.

IPCC, 2021: Climate Change 2021: The Physical Science Basis. Contribution of Working Group I to the Sixth Assessment Report of the Intergovernmental Panel on Climate Change [Masson-Delmotte, V., P. Zhai, A. Pirani, S. L. Connors, C. Péan, S. Berger, N. Caud, Y. Chen, L. Goldfarb, M. I. Gomis, M. Huang, K. Leitzell, E. Lonnoy, J. B. R. Matthews, T. K. Maycock, T. Waterfield, O. Yelekçi, R. Yu and B. Zhou (eds.)]. Cambridge University Press.

Jakubínský, J., Prokopová, M., Raška, P., Salvati, L., Bezak, N., Cudlín, O., ... & Lepeška, T. (2021). Managing floodplains using nature-based solutions to support multiple ecosystem functions and services. *Wiley Interdisciplinary Reviews: Water, 8*(5), e1545.

Jolliff, J. K., Kindle, J. C., Shulman, I., Penta, B., Friedrichs, M. A., Helber, R., & Arnone, R. A. (2009). Summary diagrams for coupled hydrodynamic-ecosystem model skill assessment. *Journal of Marine Systems, 76*(1-2), 64-82.

Juez, C., Schärer, C., Jenny, H., Schleiss, A. J., & Franca, M. J. (2019). Floodplain land cover and flow hydrodynamic control of overbank sedimentation in compound channel flows. *Water Resources Research*, *55*(11), 9072-9091.

Kaase, C. T., & Kupfer, J. A. (2016). Sedimentation patterns across a Coastal Plain floodplain: The importance of hydrogeomorphic influences and cross-floodplain connectivity. *Geomorphology*, *269*, 43-55.

Kinzer, M. (2017). *Nature's Return: An Environmental History of Congaree National Park*. Univ of South Carolina Press.

Kupfer, J. A., Meitzen, K. M., & Gao, P. (2015). Flooding and surface connectivity of Taxodium-Nyssa stands in a southern floodplain forest ecosystem. *River Research and Applications*, *31*(10), 1299-1310.

Lewin, J., & Ashworth, P. J. (2014). The negative relief of large river floodplains. *Earth-Science Reviews*, *129*, 1-23.

Lewin, J., & Hughes, D. (1980). Welsh floodplain studies: II. Application of a qualitative inundation model. *Journal of Hydrology*, *46*(1-2), 35-49.

Limerinos, J. T. (1970). Determination of the Manning coefficient from measured bed roughness in natural channels.

Lindroth, E. M., Rhoads, B. L., Castillo, C. R., Czuba, J. A., Güneralp, İ., & Edmonds, D. (2020). Spatial variability in bankfull stage and bank elevations of lowland meandering rivers: Relation to rating curves and channel planform characteristics. *Water Resources Research*, *56*(8), e2020WR027477.

Lininger, K. B., Wohl, E., Rose, J. R., & Leisz, S. J. (2019). Significant floodplain soil organic carbon storage along a large high-latitude river and its tributaries. *Geophysical Research Letters*, *46*(4), 2121-2129.

Liu, Z., Merwade, V., & Jafarzadegan, K. (2019). Investigating the role of model structure and surface roughness in generating flood inundation extents using one-and two-dimensional hydraulic models. *Journal of Flood Risk Management*, *12*(1), e12347.

Makungu, E., & Hughes, D. A. (2021). Understanding and modelling the effects of wetland on the hydrology and water resources of large African river basins. *Journal of Hydrology*, *603*, 127039.

Mazzoleni, M., Mård, J., Rusca, M., Odongo, V., Lindersson, S., & Di Baldassarre, G. (2021). Floodplains in the Anthropocene: A Global Analysis of the Interplay Between Human Population, Built Environment, and Flood Severity. *Water Resources Research*, *57*(2), e2020WR027744.

Meitzen, K. M. (2011). Flood processes, forest dynamics, and disturbance in the Congaree River floodplain, South Carolina (Doctoral dissertation). Columbia, SC: University of South Carolina.

Mertes, L. A. (1997). Documentation and significance of the perirheic zone on inundated floodplains. *Water Resources Research*, *33*(7), 1749-1762.

Mertes, L. A., Daniel, D. L., Melack, J. M., Nelson, B., Martinelli, L. A., & Forsberg, B. R. (1995). Spatial patterns of hydrology, geomorphology, and vegetation on the floodplain of the Amazon River in Brazil from a remote sensing perspective. *Geomorphology*, *13*(1-4), 215-232.

Mertes, L. A., Dunne, T., & Martinelli, L. A. (1996). Channel-floodplain geomorphology along the Solimões-Amazon river, Brazil. *Geological Society of America Bulletin*, *108*(9), 1089-1107.

Muñoz, D. F., Yin, D., Bakhtyar, R., Moftakhari, H., Xue, Z., Mandli, K., & Ferreira, C. (2021). Inter-Model Comparison of Delft3D-FM and 2D HEC-RAS for Total Water Level Prediction in Coastal to Inland Transition Zones. *JAWRA Journal of the American Water Resources Association*.

Neal, J., Schumann, G., & Bates, P. (2012). A subgrid channel model for simulating river hydraulics and floodplain inundation over large and data sparse areas. *Water Resources Research*, *48*(11).

Nobre, A. D., Cuartas, L. A., Momo, M. R., Severo, D. L., Pinheiro, A., & Nobre, C. A. (2016). HAND contour: a new proxy predictor of inundation extent. *Hydrological Processes*, *30*(2), 320-333.

Osterkamp, W. R., & Hupp, C. R. (2010). Fluvial processes and vegetation—glimpses of the past, the present, and perhaps the future. *Geomorphology*, *116*(3-4), 274-285.

Park, E. (2020). Characterizing channel-floodplain connectivity using satellite altimetry: Mechanism, hydrogeomorphic control, and sediment budget. *Remote Sensing of Environment*, *243*, 111783.

Park, E., & Latrubesse, E. M. (2017). The hydro-geomorphologic complexity of the lower Amazon River floodplain and hydrological connectivity assessed by remote sensing and field control. *Remote Sensing of Environment*, *198*, 321-332.

Passalacqua, P. (2017). The Delta Connectome: A network-based framework for studying connectivity in river deltas. *Geomorphology*, *277*, 50-62.

Patterson, G. G., Whetstone, B. H., & Speiran, G. K. (1985). *Hydrology and its effects on distribution of vegetation in Congaree Swamp National Monument, South Carolina.* Columbia: U.S. Geological Survey.

Pavelsky, T. M., Durand, M. T., Andreadis, K. M., Beighley, R. E., Paiva, R. C., Allen, G. H., & Miller, Z. F. (2014). Assessing the potential global extent of SWOT river discharge observations. *Journal of Hydrology*, *519*, 1516-1525.

Pinel, S., Bonnet, M. P., S. Da Silva, J., Sampaio, T. C., Garnier, J., Catry, T., ... & Seyler, F. (2020). Flooding dynamics within an Amazonian floodplain: water circulation patterns and inundation duration. *Water Resources Research*, *56*(1), e2019WR026081.

Rak, G., Kozelj, D., & Steinman, F. (2016). The impact of floodplain land use on flood wave propagation. *Natural hazards*, *83*(1), 425-443.Sutfin, N. A., Wohl, E. E., & Dwire, K. A. (2016). Banking carbon: a review of organic carbon storage and physical factors influencing retention in floodplains and riparian ecosystems. *Earth Surface Processes and Landforms*, *41*(1), 38-60.

Rowland, J. C., Dietrich, W. E., Day, G., & Parker, G. (2009). Formation and maintenance of single-thread tie channels entering floodplain lakes: Observations from three diverse river systems. *Journal of Geophysical Research: Earth Surface*, *114*(F2).

Rudorff, C. M., Melack, J. M., & Bates, P. D. (2014). Flooding dynamics on the lower Amazon floodplain: 1. Hydraulic controls on water elevation, inundation extent, and river-floodplain discharge. *Water Resources Research*, *50*(1), 619-634.

Sharitz, R. R., & Allen, B. P. (2009). Quantify Change in the Old-growth Forests of Congaree National Park. *Final Report, USDI NPS CA.*

Shelley, D. C. (2007). Geology, geomorphology, and tectonics of the Congaree River valley, South Carolina (Doctoral dissertation). Columbia, SC: University of South Carolina.

Shelley, D. C., Werts, S., Dvoracek, D., & Armstrong, W. (2012). Blujf to blujf: A field guide to floodplain geology and geomorphology of the Lower Congaree River Valley, South Carolina. *From the Blue Ridge to the Coastal Plain; Field Excursions in the Southeastern United States*, *29*, 67.

Stevens, A. W., van der Steeg, S., Wherry, S. A., & Wood, T. M. (2021). Hydrodynamic model of the lower Columbia River, Oregon and Washington, 2017-2020: US Geological Survey data release.

Straatsma, M. W., & Kleinhans, M. G. (2018). Flood hazard reduction from automatically applied landscaping measures in RiverScape, a Python package coupled to a two-dimensional flow model. *Environmental Modelling & Software*, *101*, 102-116

Sutfin, N. A., Wohl, E. E., & Dwire, K. A. (2016). Banking carbon: a review of organic carbon storage and physical factors influencing retention in floodplains and riparian ecosystems. *Earth Surface Processes and Landforms*, *41*(1), 38-60.

Thompson, A. J. (1998). *An ecological inventory and classification of an old-growth floodplain forest in the southeastern United States coastal plain* (Doctoral dissertation, University of Georgia).

Torres, R., & Styles, R. (2007). Effects of topographic structure on salt marsh currents. *Journal of Geophysical Research: Earth Surface*, *112*(F2).

Trigg, M. A., Bates, P. D., Wilson, M. D., Schumann, G., & Baugh, C. (2012). Floodplain channel morphology and networks of the middle Amazon River. *Water Resources Research*, *48*(10).

Tull, N., Passalacqua, P., Hassenruck-Gudipati, H. J., Rahman, S., Wright, K., Hariharan, J., & Mohrig, D. (2022). Bidirectional River-Floodplain Connectivity During Combined Pluvial-Fluvial Events. *Water Resources Research*, *58*(3), e2021WR030492.

US Department of Agriculture-Natural Resources Conservation Service (USDA-NRCS). (2007). Stream restoration design. *Part 654 of the national engineering handbook, 210-VI-NEH*.

van der Steeg, S., Torres, R., Viparelli, E., Xu, H., Elias, E., & Sullivan, J. C. (2023). Floodplain Surface-Water Circulation Dynamics: Congaree River, South Carolina, USA. *Water Resources Research*, *59*(1), e2022WR032982.

van der Steeg, S., Xu, H., Torres, R., Elias, E. P., Sullivan, J. C., Viparelli, E., ... & Lakshmi, V. (2021). A novel method for gaining new insight on flows over inundated landscapes. *Geophysical Research Letters*, *48*(20), e2021GL094190.

Verwey, A. (2001). Latest developments in floodplain modelling-1D/2D integration. In *6th Conference on Hydraulics in Civil Engineering: The State of Hydraulics; Proceedings* (p. 13). Institution of Engineers, Australia.

Williams, L. L., & Lück-Vogel, M. (2020). Comparative assessment of the GIS based bathtub model and an enhanced bathtub model for coastal inundation. *Journal of Coastal Conservation*, *24*(2), 1-15.

Williams, T. M., Song, B., & Shelley, D. C. (2017). GIS analysis of historical maps: A case study from an 1885 survey of the Congaree River. *Mathematical and Computational Forestry & Natural Resource Sciences*, *9*(2), 3.

Willmott, C. J. (1981). On the validation of models. *Physical geography*, *2*(2), 184-194.

Wohl, E. (2017). Connectivity in rivers. *Progress in Physical Geography*, *41*(3), 345-362.

Wohl, E., Brierley, G., Cadol, D., Coulthard, T. J., Covino, T., Fryirs, K. A., Grant, G., et al. (2019). Connectivity as an emergent property of geomorphic systems. *Earth Surface Processes and Landforms,* 44, 4-26.

Wohl, E., Polvi, L. E., & Cadol, D. (2011). Wood distribution along streams draining old-growth floodplain forests in Congaree National Park, South Carolina, USA. *Geomorphology*, *126*(1-2), 108-120.

Wolfs, V., & Willems, P. (2014). Development of discharge-stage curves affected by hysteresis using time varying models, model trees and neural networks. *Environmental Modelling & Software*, *55*, 107-119.

Xu, H., Torres, R., van der Steeg, S., & Viparelli, E. (2021). Geomorphology of the Congaree River floodplain: Implications for the inundation continuum. *Water Resources Research*, *57*(12), e2020WR029456.

Xu, H., van der Steeg, S., Sullivan, J., Shelley, D., Cely, J. E., Viparelli, E., Lakshmi, V & Torres, R. (2020). Intermittent Channel Systems of a Low-Relief, Low-Gradient

Floodplain: Comparison of Automatic Extraction Methods. *Water Resources Research*, *56*(9), e2020WR027603.

Yamazaki, D., Kanae, S., Kim, H., & Oki, T. (2011). A physically based description of floodplain inundation dynamics in a global river routing model. *Water Resources Research*, *47*(4).

Yamazaki, D., Lee, H., Alsdorf, D. E., Dutra, E., Kim, H., Kanae, S., & Oki, T. (2012). Analysis of the water level dynamics simulated by a global river model: A case study in the Amazon River. *Water Resources Research*, *48*(9).

Yankovsky, A. E. (2003). The cold-water pathway during an upwelling event on the New Jersey shelf. *Journal of physical oceanography*, *33*(9), 1954-1966.

Zhang, A. T., & Gu, V. X. (2023). Global Dam Tracker: A database of more than 35,000 dams with location, catchment, and attribute information. *Scientific Data*, *10*(1), 111.

Zhang, Q., & Werner, A. D. (2015). Hysteretic relationships in inundation dynamics for a large lake–floodplain system. *Journal of hydrology*, *527*, 160-171.

Zhang, X. L., Zhang, Q., Werner, A. D., & Tan, Z. Q. (2017). Characteristics and causal factors of hysteresis in the hydrodynamics of a large floodplain system: Poyang Lake (China). *Journal of hydrology*, *553*, 574-583.

APPENDIX A

SUPPORTING INFORMATION FOR:

FLOODPLAIN SURFACE-WATER CIRCULATION DYNAMICS: CONGAREE RIVER, SOUTH CAROLINA, USA

This appendix contains a detailed description of the model set-up and the computational grid (A.1, Figure A.1), the model performance assessment under quasi-real-time forcing conditions (A.2, Figures A.2-A.6, Tables A.1-A.4), and model limitations (A.3). system. Further, this approach allows for simultaneous evaluation of the rising and falling stage, and flow dynamics (e.g., flooding and drainage).

A.1 DELFT3D FLEXIBLE MESH MODEL SET-UP

Computational grid schematization represents a tradeoff between the processes to be modeled and the computational run time. Also, the spatial coverage (i.e., model domain) and grid resolution should be adequate to capture the processes of interest while allowing for efficient and accurate computations. For the Congaree River, floodplain inundation is controlled by 1) the Congaree and Wateree Rivers discharge and its propagation into the floodplain through an extensive channel network (*Xu et al., 2020, 2021*), and 2) inflow from upland creeks as well as upstream floodplain flows. To accurately capture these processes, a flexible mesh computational grid with a varying spatial resolution was constructed through an iterative sensitivity analysis, but over a much larger domain of 247 km^2, including the Wateree (inclusive of the eastern floodplain) and Santee rivers (Figure 3.1a). The optimized model domain starts at rkm -15.2 km and extends ~5 km eastward of rkm 48.4, while our area of interest extends from rkm 0 to 45.4 (Figure 3.1). The width of the model domain varies but is restricted by the physical boundaries of the local upland bluffs (Figure 3.1). Altogether, this region includes approximately 60.8 km of the Congaree River, 2.8 km of the Santee River, and 7.5 km (along-channel) of the Wateree River.

The optimal simulation mesh, determined through a grid independence study, consists of a rectangular grid aligned with the Congaree, Wateree and Santee rivers with a grid cell size of 12.5 m along the centerline of the main channels (Table A.1a). Grid cells of 6.25 m for the riverbanks and over the levees accurately represents levee effects (Table A.1b), and thus ensures representative fluxes between river and floodplain via overbank and through-bank channel flows. The northern floodplain mesh involves an overall 12.5 m rectangular grid and the transition between the river - floodplain mesh is constructed using triangular grid cells. In the floodplain, major channels are delineated by 6.25 m cells guided by geomorphic floodplain feature extraction results (Table A.1c; *Xu et al., 2020*). The extraction results are estimated with channel centerlines, and a 12.5 m buffer is created on both sides of a channel to sufficiently represent the channel geometry. Similarly, geomorphic features, such as lakes and oxbows, were identified and delineated using a 12.5 m buffer. Transitions between the 12.5 m and 6.25 m grids are realized using triangular grid cells. The southern floodplain mesh does not contain delineated features and sensitivity testing revealed that near-identical results could be obtained with the application of a coarser rectangular 25 m grid beyond the 6.25 and 12.5 m refinement over the levees (Figure A.1a and A.1b), while reducing the overall computational run time.

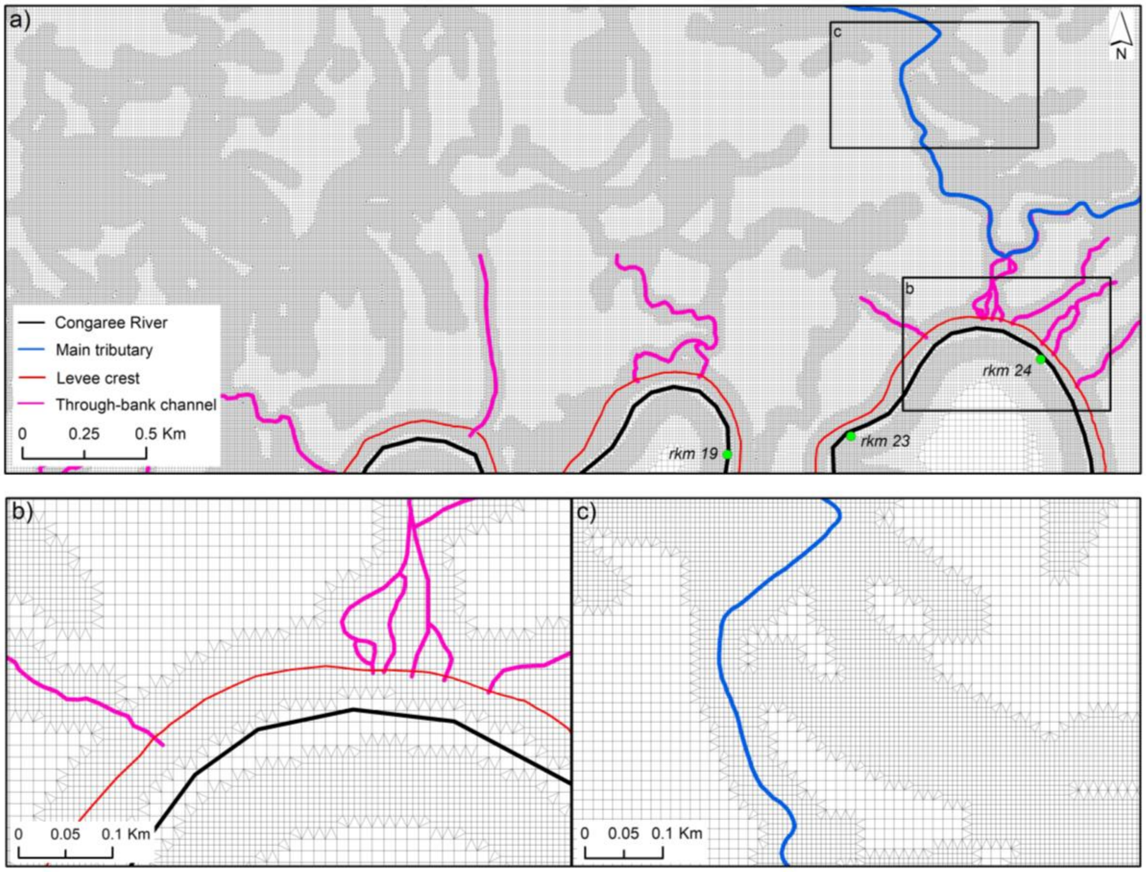

Figure A.1: Congaree River Floodplain model grid. (a) Subarea of the model grid. See Figure 3.1b for spatial extent of subarea. (b) Detail of model grid near main channel. (c) Detail of model grid in the floodplain interior.

The floodplain model bathymetry is based on the 2010 digital elevation model (*Xu et al., 2020*) and river bathymetry using a single-beam sonar (*Ohmex Sonarmite*) collected 2019 - 2020. The initial bathymetry was smoothed to reduce small-scale disturbances and improve numerical stability. Depending on the resolution of the elevation observations, depth measurements were triangularly interpolated (low-resolution data) or grid-cell averaged (high-resolution data) to the computational grid. Delft3D FM allows for a linearly varying bed level within a grid cell, and this setting results in a more accurate representation of the actual bathymetry. A comparison of observed and modeled domain volume in each gridcell shows that the above-described settings result in the most accurate representation of bathymetry with an average discrepancy of 4.3 % and a maximum of 9.1 %; the maximum discrepancy occurs outside the region of interest.

Surface and bed roughness were schematized using the Manning formulation, which relates bed friction to water depth. The exact value of the Manning's roughness coefficient is often poorly constrained due to varying conditions (e.g., *Limerinos, 1970*). In Congaree National Park (CNP), varying roughness conditions, apart from local water depth, depends on seasonal vegetation coverage (*Doyle, 2009*) and the transport and displacement of debris (*Wohl et al., 2011*). As a result, the roughness coefficients were described during the calibration process, and initial roughness estimates were guided by *Arcement and Schneider* (*1989*) and *Barnes* (*1967*). Simulated water levels were compared against measurements of observed water levels from six locations in the river and seven locations in the floodplain for varying river discharge conditions. The sensitivity of flow was examined for a range of spatially varying Manning roughness coefficients in multiple but otherwise identical simulations.

The absence of observations near the boundaries of the model domain required an extension of the grid to the nearest available United States Geological Survey (USGS) gauges with appropriate data. Therefore, the Congaree River has been extended from its model domain entry point (rkm -15.2) to the USGS gauge Congaree River at Columbia, SC (#02169500, rkm -38.8) and is schematized using a curvilinear grid aligned with the levees and land boundaries. A similar curvilinear grid is aligned with the Wateree River to extend the model domain entry point to the USGS Wateree River gauge station near Camden, SC (#02148000). The Santee River does not require an extension due to the presence of the USGS Santee River gauge near Fort Motte (#02169810, rkm 48.4). This modeling approach thus includes the capacity to simulate flows entering the CNP area of interest from both the river and from the upstream floodplain.

The Congaree River and Wateree River boundaries are forced using a discharge time series (Table A.2) obtained from the USGS gauging stations (Figure 3.1b). The Cedar Creek (USGS #02169672, in CNP) and Tom's Creek discharges were estimated based on water level measurement and cross-sectional area. The downstream boundary condition at the Santee River (rkm 48.4) consists of a time series of water levels obtained from the USGS station (#02169810). All water level data were converted to the North American Vertical Datum of 1988 prior to use. Both types of boundary conditions allow for undisturbed propagation of flow out of the domain. The eastern and southern (right of the Santee River boundary, Figure 3.1a) periphery of the computational grid were defined as zero-gradient Neumann boundaries to allow for the undisturbed propagation of flood waves out of the domain. Applying Neumann boundaries is especially important for high flow conditions in which flood waves exit the model domain naturally over the Santee and Wateree floodplain systems. All boundary conditions are located at a sufficiently large distance to preclude their influence on the area of interest.

Computations start with a uniform water level. Analyses of model results indicate that the initial inundation state is crucial to determining accurate model results, and therefore, the computations start 14 days prior to the events of interest. Sensitivity testing revealed that the adaptation period is shorter for high flow conditions. This 'spin-up' period, prior to the actual computations, is sufficient to dissipate the errors induced by the discrepancy between boundary conditions and initial state.

A.2 MODEL PERFORMANCE ASSESSMENT

Model calibration and validation are closely related and important aspects of model development. These important modeling elements help ensure the model products are representative of actual processes. In this study, the calibration and validation work focus on the representation of 1) water level in the main channel, 2) water level in the floodplain, 3) flow direction, and 4) flow gradient over the floodplain. The model performance was evaluated using the "index of agreement" or "*skill*" (*Willmott*, *1981*), which compares simulated and observed time series. *Skill* varies between 0 (complete disagreement) and 1 (perfect agreement). The advantage of using the Willmott *skill* index is that it is dimensionless, allowing a comparison of multiple parameters. The disadvantage, however, is that disagreements in either bias or in variance are masked in a single *skill* metric. To ameliorate this perceived shortcoming, in addition to *skill*, the mean bias, bias-corrected root-mean-square-error, and total root-mean-square-error are utilized to aid the calibration process (*Jolliff et al., 2009*).

Calibration is performed under quasi-real-time forcing conditions by optimizing the initial estimates of the Manning roughness coefficients. The nature of flow in the system required two separate calibration hydrographs: a sub-bankfull (C_1, Table A.2a) and an overbank (C_2, Figure A.2c) flow scenario. In C_1, the water levels in the river are below bankfull and water enters the floodplain as through-bank flow and associated channel network redistribution (e.g., *Xu et al., 2021*). During C_2, the river stage exceeds bank elevation and water enters the floodplain as overbank flow and through-bank flows. The model optimization process requires an integrative system approach rather than an elementwise approach where the river and floodplain structural features are considered separate elements. Optimizing the roughness field demonstrated that flow resistance in various floodplain features influences the hydrodynamics in the main channel and vice versa. A spatially varying roughness field consisting of six different Manning roughness coefficients was required to determine accurate model results, largely based on geomorphic features (*Xu et al., 2020*), and elevation distributions (*Doyle, 2009*). Moreover, the model was successfully validated against a sub-bankfull (V_1, Figure A.2b) and overbank (V_2, Figure A.2d) flow event in otherwise identical model configurations.

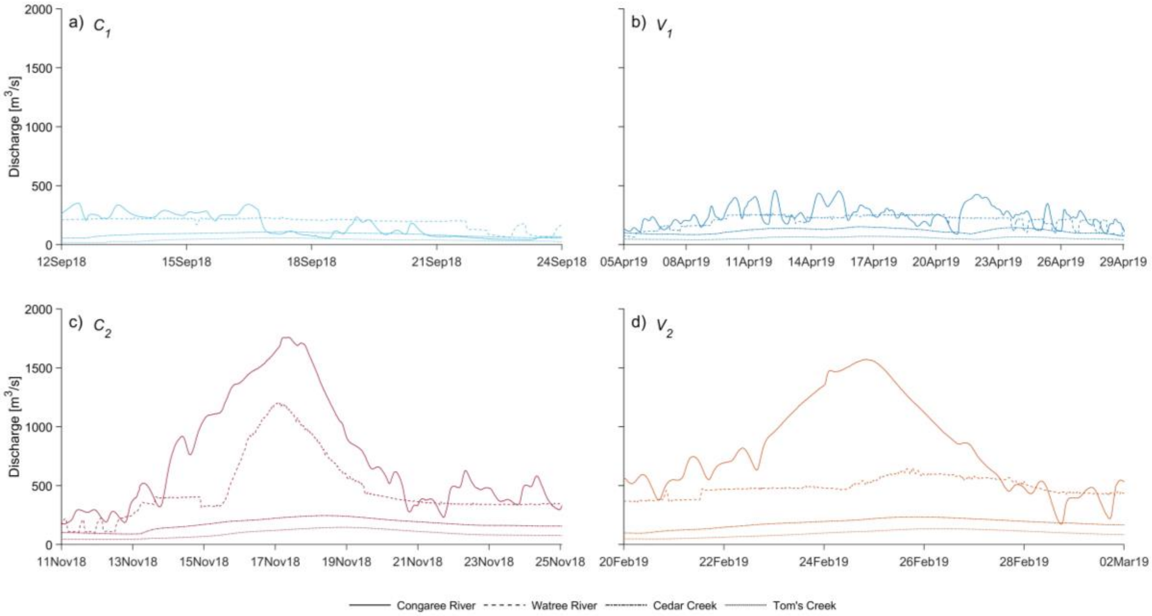

Figure A.2: Model discharge inflow boundary conditions on the Congaree River, Wateree River, Cedar Creek, and Tom's Creek. Dates are formatted as day/month/year. C1: lower sub-bankfull calibration scenario; V1: higher sub-bankfull validation scenario; C2: higher overbank calibration scenario; V2: lower overbank validation scenario.

A.2.1 Water levels

River water levels and variance were best represented by channel roughness values of 0.0021 and 0.0023 s/m$^{1/3}$ upstream and downstream (including parts of the Wateree and Santee Rivers), respectively (Figure A.3; Table A.1). Physically, this spatial distribution can be explained by an increased percentage of bedforms in strongly meandering river segments, as revealed by sonar. The roughness distribution produced accurate results during testing (Figure A.3). The *skill* varied between 0.91 and 0.95, with the best performance for higher river stages at each observation location (Table A.1). Simulated water levels have a slight lag of 1.1 ± 0.5 hours and the average total RMS is 0.02 ± 0.05 m, with a maximum of 0.08 m.

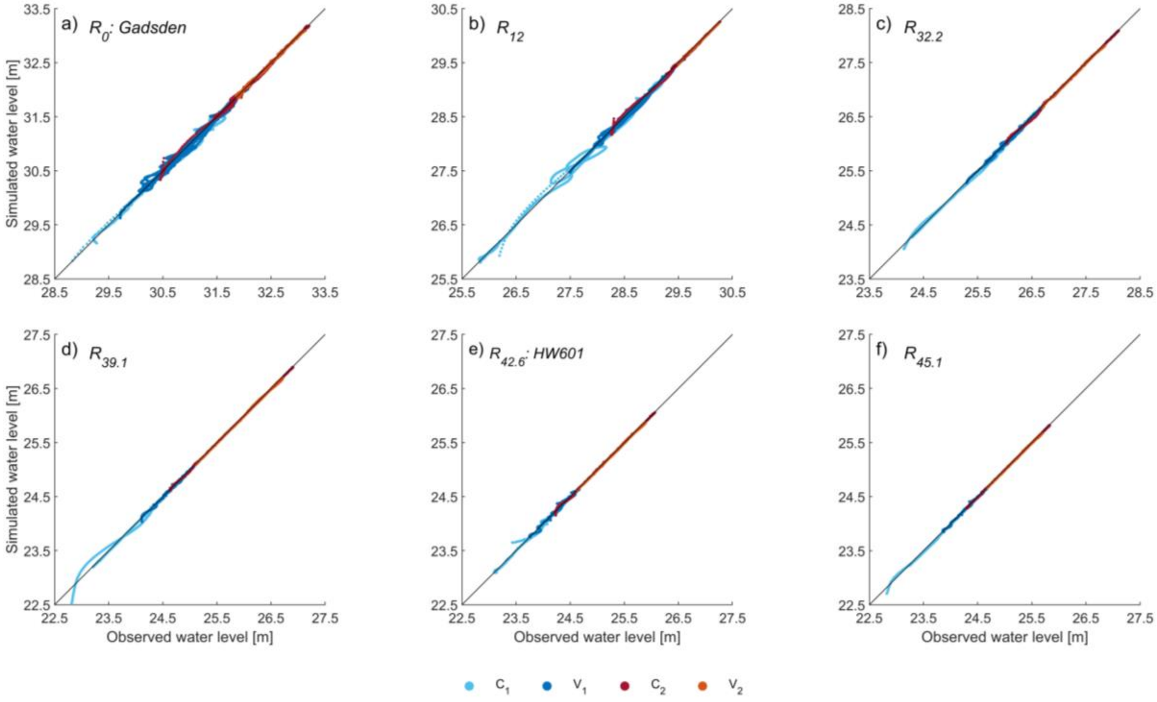

Figure A.3: Comparison of observed and simulated water levels for sensors positioned in the Congaree River. See Figure 3.1b for the along-channel locations of sensors. C1: lower sub-bankfull calibration scenario; V1: higher sub-bankfull validation scenario; C2: higher overbank calibration scenario; V2: lower overbank validation scenario.

Table A.1: Error metrics describing model performance of simulated water levels for four flow scenarios (C1, V1, C2, V2) at six observation stations along the Congaree River.

Error Metric	Scenario	*Skill* [-], error [m]					
		R_0	R_{12}	$R_{32.2}$	$R_{39.1}$	$R_{42.6}$	$R_{45.1}$
Willmott	C_1	0.90	0.91	0.95	0.93	0.92	0.92
	V_1	0.91	0.94	0.95	0.92	0.93	0.92
	C_2	0.96	0.95	0.95	0.94	0.95	0.93
	V_2	0.95	0.95	0.95	0.94	0.94	0.93
Mean bias	C_1	-0.01	-0.01	-0.02	-0.01	-0.02	-0.02
	V_1	-0.01	0.02	-0.01	-0.01	-0.01	-0.01
	C_2	-0.01	-0.01	-0.01	-0.01	-0.01	-0.01
	V_2	-0.01	-0.01	-0.01	-0.01	-0.01	-0.01
Bias-corrected RMS error	C_1	0.08	0.01	0.02	0.03	0.03	0.01
	V_1	0.05	0.03	0.02	0.02	0.03	0.02
	C_2	0.02	0.01	0.01	0.01	0.01	0
	V_2	0.03	0.01	0.01	0.01	0.01	0.01
Total RMS	C_1	0.08	0.01	0.02	0.04	0.04	0.02
	V_1	0.05	0.04	0.02	0.02	0.03	0.02
	C_2	0.02	0.02	0.02	0.01	0.01	0.01
	V_2	0.03	0.01	0.02	0.02	0.01	0.01

Water levels in the floodplain were most accurate for a floodplain channel roughness of 0.036 s/m$^{1/3}$ while 0.045 s/m$^{1/3}$was applied to the remaining floodplain (e.g., oxbows, lakes). These roughness values were determined based on scenario C_1 and confirmed by V_1 (Figures 3.2a-3.2d; Figure A.4; Table A.2). Sensitivity analyses indicate that during sub-bankfull conditions, the model performance was substantially affected by subtle variations in the channel roughness, while the surface roughness (areas not identified as channels or depressions) was insignificant. During sub-bankfull inundation, only sites T_3, T_4, T_5, T_6 and T_7 showed water level responses useful for calibration. The roughness values were, however, imposed on all floodplain channels and related features, as well as locations where no response was observed during sub-bankfull stages (T_1, T_2). The *skill* varies between 0.39 and 0.93, with better performance during higher sub-bankfull river stages at each of the floodplain observation locations (Table A.2). The model results are most erroneous near site T_7 at the northern park boundary (Figure 3.1b) and can be attributed to higher levels of uncertainty in topographic data due to the presence of standing water at the time of the lidar mission (*Xu et al., 2020*). For sub-bankfull river stages, the discrepancies between observed and simulated are primarily related to water level variability, while the mean water level is more accurate. The average total RMS is 0.07 ± 0.05 m, with a maximum of 0.18 m.

Overbank inundation events allow for the determination of the roughness coefficient of the floodplain surface. The corresponding surface roughness values of 0.10 and 0.12 $s/m^{1/3}$, upstream and downstream of rkm 12.8, respectively, best represent water levels during overbank inundation (Figures 3.3e-3.3h; Figure A.4; Table A.2). This subdivision can be physically explained by variations in vegetation coverage (*Thompson*, 1998, *Gaddy and Smathers*, *1980*), which is generally denser downstream of rkm -29.8. Sensitivity testing revealed that the floodplain surface roughness is the dominating factor in determining accurate model results during overbank inundation. The roughness of floodplain channels and lakes does not substantially affect the model performance. In fact, it performs substantially better during overbank flows. For example, the *skill* varies between 0.89 and 0.94, with the best performance during higher river stages (Table A.2). Error estimates for overbank inundation are primarily associated with discrepancies in modeled variability. The average total RMS is 0.03 ± 0.02 m, with a maximum of 0.05 m.

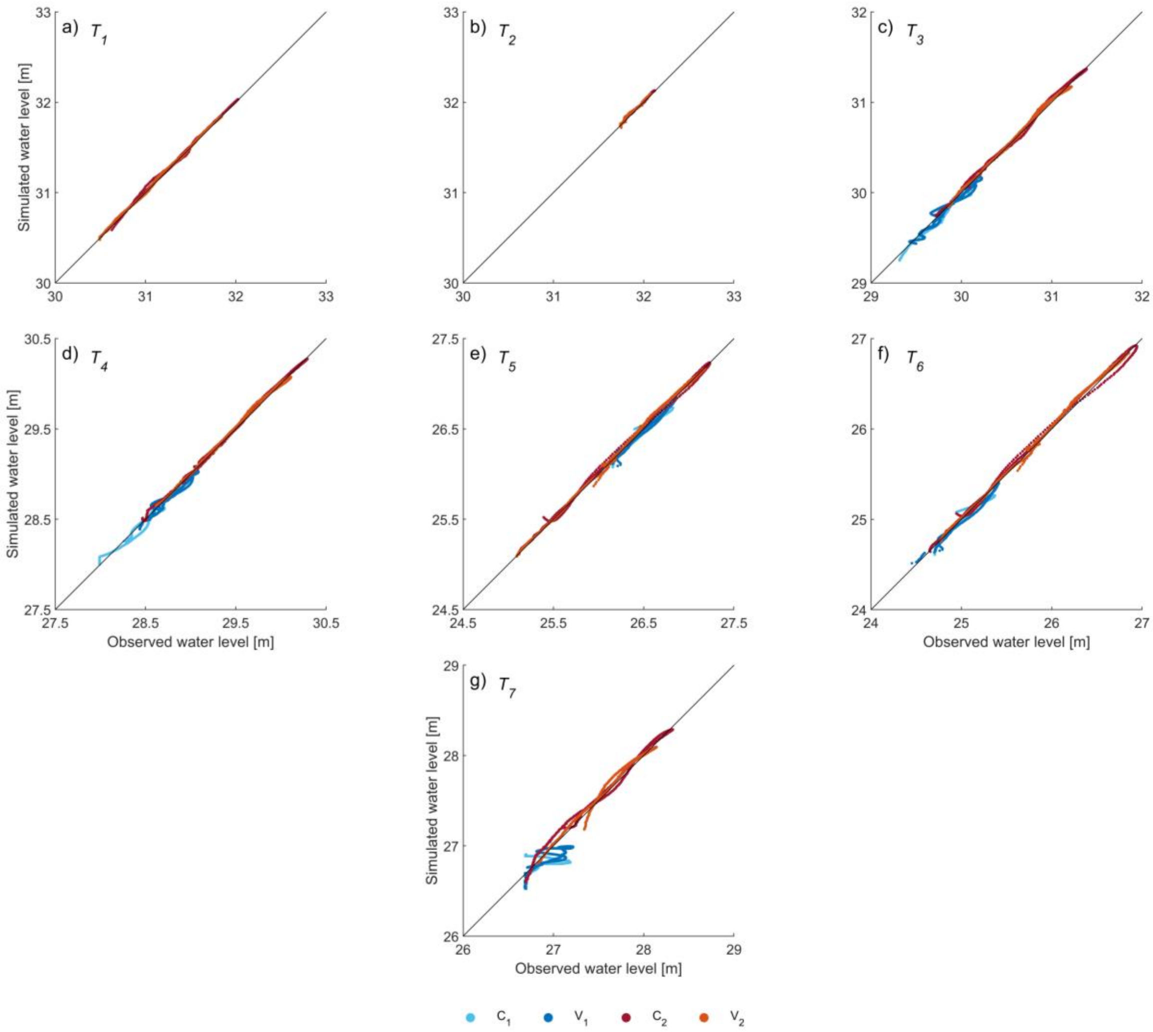

Figure A.4: Comparison of observed and simulated water levels for sensors on the floodplain. See Figure 3.1b for the location of sensors. Each triangular facet consists of three sensors (except T5 due to a missing sensor); all sensor data is shown. C1: lower sub-bankfull calibration scenario; V1: higher sub-bankfull validation scenario; C2: higher overbank calibration scenario; V2: lower overbank validation scenario.

Table A.2: Error metrics describing model performance of simulated water levels for four flow scenarios (C1, V1, C2, V2) at seven observation stations in the Congaree River floodplain.

Error Metric	Scenario	*Skill* [-], error [m]						
		T_1	T_2	T_3	T_4	T_5	T_6	T_7
Willmott	C_1	-	-	0.82	0.93	0.89	0.89	0.39
	V_1	-	-	0.88	0.92	0.89	0.89	0.52
	C_2	0.90	0.92	0.92	0.94	0.93	0.93	0.89
	V_2	0.90	0.92	0.92	0.94	0.92	0.91	0.89
Mean bias	C_1	-	-	-0.03	-0.04	-0.04	-0.04	-0.11
	V_1	-	-	-0.03	-0.03	-0.03	-0.03	-0.10
	C_2	0.02	-0.01	0.02	0.01	0.02	0.02	0.03
	V_2	0.01	-0.02	0.01	0.01	0.01	0.02	0.02
Bias-corrected RMS error	C_1	-	-	0.04	0.05	0.04	0.04	0.41
	V_1	-	-	0.04	0.03	0.03	0.02	0.10
	C_2	0.01	0.01	0.02	0.02	0.03	0.02	0.04
	V_2	0.01	0.01	0.02	0.02	0.03	0.02	0.05
Total RMS	C_1	-	-	0.05	0.06	0.06	0.05	0.18
	V_1	-	-	0.05	0.04	0.04	0.04	0.14
	C_2	0.02	0.02	0.03	0.02	0.03	0.03	0.05
	V_2	0.02	0.02	0.03	0.02	0.03	0.03	0.05

A.2.2 Flow directions

Simulated flow direction and gradient were compared to observations (after *van der Steeg et al., 2021*) for model validation. Model calibration focused on the correct representation of water level, and no changes to the roughness field were made to improve the representation of flow directions and magnitudes. However, despite being derived from simulated water levels, flow directions provide an additional valuable validation dataset. Simulated water levels contain errors (Figure 3.2; Figure A.4; Table A.2), and validation against other flow properties (e.g., flow directions) provides information on error propagation within the model configuration. Furthermore, flow direction provides a larger scale validation *area* (~0.1 km^2), while water levels are point measurements. Therefore, the method can augment assessments of model performance by helping to detect the origin of errors (e.g., inaccurate bathymetry, imposed roughness field). Flow directions for sub-bankfull conditions can only be determined at sites T_3, T_4, T_6, and T_7, while overbank flow directions can be assessed at all sites. Site T_5 was excluded due to one missing sensor. For T_3 and T_4, flow directions are visualized along with the hydrograph (Figure 3.2); for other sites, the error metrics are shown in Tables S3 and S4, and graphically shown using rose diagrams (Figure A.5 and A.6).

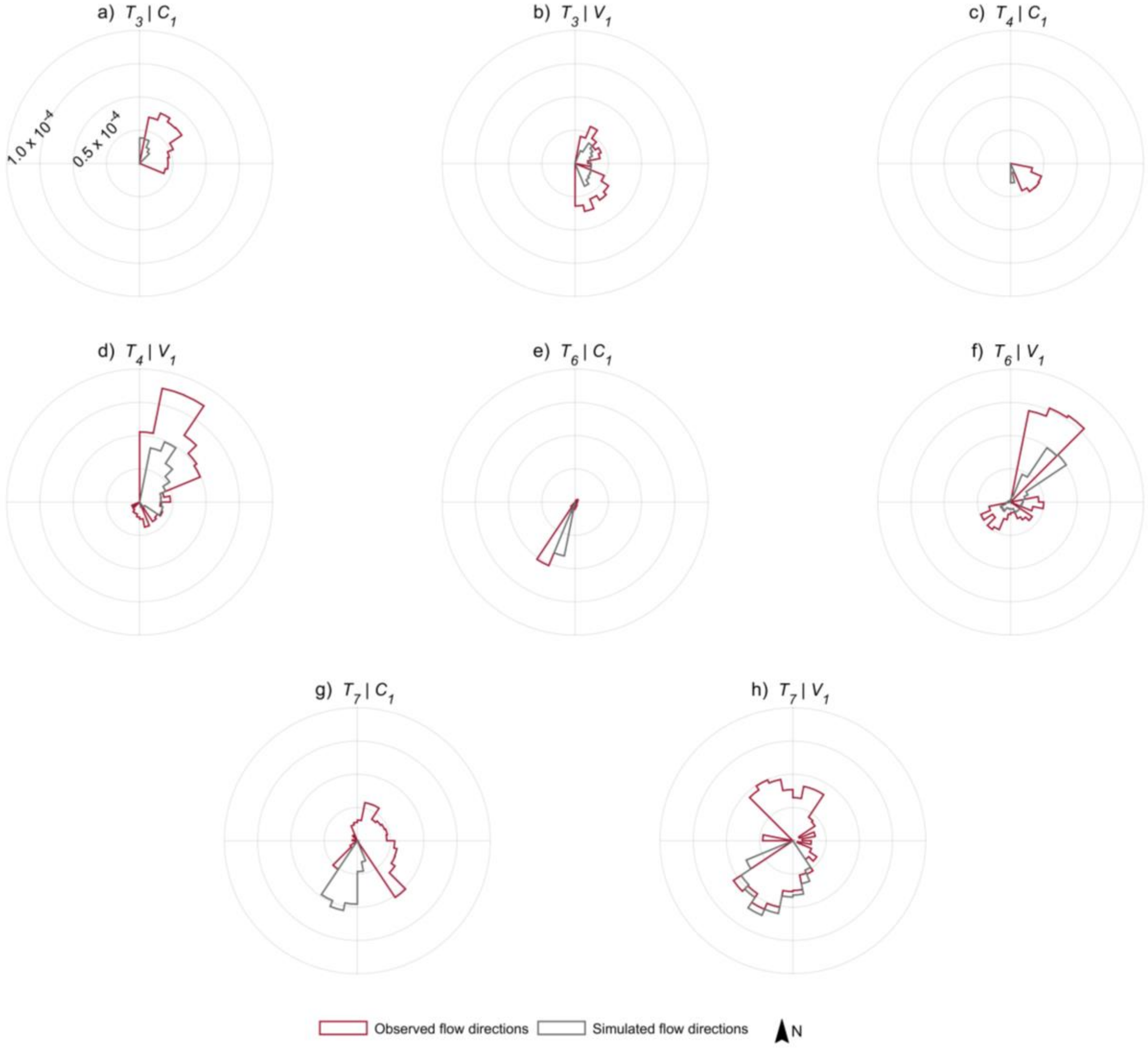

Figure A.5: Comparison of observed and simulated flow directions utilizing the Triangular Facet approach for sensors positioned in the Congaree National Park during sub-bankfull inundation conditions. See Figure 3.1b for the location of sensors. C1: lower sub-bankfull calibration scenario; V1: higher sub-bankfull validation scenario.

For C_1, the model produced representative flow directions (Figure 3.2a and 3.2b; Figure A.5a, A.5c, A.5e and A.5g; Table A.3). The simulated directions deviate an average of 39°± 18° from the observations. The best model performance is observed at site T_6 and is most erroneous at T_7. Topographic data surrounding T_7 is uncertain due to the presence of standing water at the time of the lidar mission, as is also evident in the water level *skill*. Simulated flow at T_7 results from local creek flow only, as the model does not accurately convey river discharge to the observation site.

For scenario V_1, a higher sub-bankfull flow event, the model performs substantially better, and can reproduce changes in flow directions (Figure 3.2c and 2d; Figures A.5b, A.5d, A.5f and A.5h; Table A.3). The deviation averages 26°± 16°and flow reversals have an average lag of 2.5 ± 4 hours. The best *skill* is observed at site T_3. Like scenario C_1, model results are most erroneous at T_7, likely for a similar reason. For sub-bankfull inundation, the directional *skill* varies between 0.12-0.64. For both C_1 and V_1, the simulated magnitude of the free surface gradients is substantially smaller than the observed gradients (Figures 3.2a-3.2d; Figure A.5; Table A.4). For C_1 and V_1, the gradients are, on average, 51% and 40 %, respectively, smaller than observed. Despite these discrepancies, the variability in simulated magnitude is consistent with observations in that higher observed gradients result in higher simulated gradients (Figures 3.2a-3.2d; Figure A.5). Simulated gradients are subdued as the relative water level differences between hydrographs within a triangular facet are smaller than observed. Furthermore, the simulated hydrographs are much smoother than observed, and the model is unable to resolve small-scale temporal variability (<~4 hours), resulting in increasingly subdued gradients and variability.

Flow directions during overbank flow deviate on average 21°± 18° for C_2, and 16°± 14° for V_2 (Figures 3.2e-3.2h; Figure A.6; Table A.3). The best model performance is observed at site T_3, while the model results are most erroneous at T_7, as expected. For the overbank inundation scenarios, the directional *skill* varies between 0.72-0.85 (Table A.3). The magnitude of the free surface gradients for both C_2 and V_2 is smaller than the observed gradients; for both C_2 and V_2, the gradients are, on average, 16% smaller than observed (Figures 3.2e-3.2h; Figure A.6; Table A.4;). The modeled magnitude variability is consistent with observations. The *skill* for magnitude varies between 0.52-0.89. Overall, the validation and calibration results reported here show that model construct is sufficiently robust to provide detailed insight into floodplain wetting and drainage processes, and for predicting flow dynamics.

Table A.3: Error metrics describing model performance of simulated flow directions for four flow scenarios (C1, V1, C2, V2) at five observation stations in the Congaree River floodplain.

Error Metric	Scenario	*Skill* [-], error [degrees]				
		T_1	T_3	T_4	T_6	T_7
Willmott	C_1	-	0.39	0.22	0.38	0.12
	V_1	-	0.64	0.58	0.63	0.16
	C_2	0.81	0.85	0.83	0.79	0.74
	V_2	0.79	0.84	0.84	0.80	0.72
Mean bias	C_1	-	41±38	50±34	33±21	136±43
	V_1	-	22±24	27±20	23±23	148±65
	C_2	19±18	11±12	11±23	22±21	25±27
	V_2	14±29	12±18	16±31	28±32	26±31

Table A.4: Error metrics describing model performance of simulated magnitudes of the free surface gradients for four flow scenarios (C1, V1, C2, V2) at five observation stations in the Congaree River floodplain. Mean bias is expressed as a percentage of simulated magnitude over observed magnitudes, and is calculated over bins with similar flow directions. No mean bias is shown for C1 for T4 and T7 as there are no bins with corresponding flow directions (Figure A.5c and A.5g).

Error Metric	Scenario	*Skill* [-], error [-]				
		T_1	T_3	T_4	T_6	T_7
Willmott	C1	-	0.32	0.21	0.36	0
	V1	-	0.61	0.57	0.61	0.10
	C2	0.52	0.77	0.69	0.72	0.88
	V2	0.89	0.69	0.76	0.73	0.86
Mean bias	C1	-	41	-	58	-
	V1	-	68	67	42	64
	C2	85	91	82	83	79
	V2	88	86	85	87	76

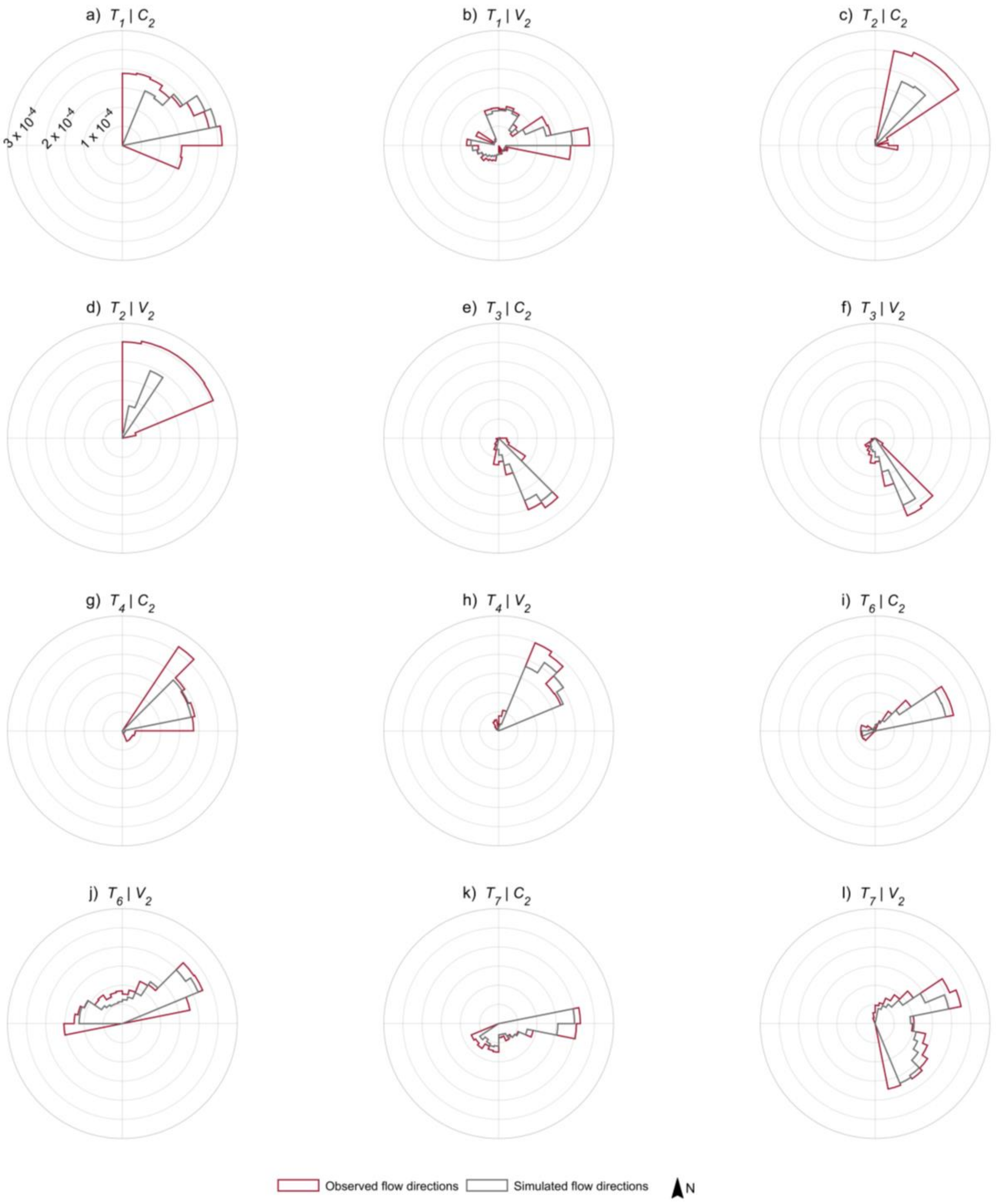

Figure A.6: Comparison of observed and simulated flow directions utilizing the Triangular Facet approach for sensors positioned in the Congaree National Park during overbank inundation conditions. See Figure 3.1b for the location of sensors. C2: higher overbank calibration scenario; V2: lower overbank validation scenario.

A.3 MODEL LIMITATIONS

As with all numerical studies, the hydrodynamic model and simulation outputs have an inherent uncertainty resulting from the schematizations and approximations of real-world flow processes, and computational time restrictions that may impact the interpretation of results. First, computational time restrictions do not allow for the full three-dimensional simulation of the elaborate model domain over sufficiently long periods (> 45 days). Local simulation results are therefore less accurate in areas where 3D currents are important, e.g., at the riverbank vertical accelerations, neglected in a depth averaged model, are in fact important. A second uncertainty in model model-setup is with the use of topographic data that does not correspond to time periods of flow events. The lidar used for floodplain topography was collected in 2010 (*Xu et al*., 2020), and river bathymetry was collected in 2019. The main channel has been relatively stable (*Williams et al., 2017).* However, field surveys indicate that spatially varying sedimentation occurs across the floodplain (*Kinzer, 2017*; *Shelley et al., 2012*), and therefore it is possible that some highly dynamic parts of the floodplain have changed over the interim. A third uncertainty in the model is the use of static Manning roughness values while the vegetation within CNP and surrounding floodplain shows strong seasonal variation in groundcover and undergrowth.